

1    **Sulfur cycling in the gabbroic section of the Oman Ophiolite**

2    Ana P Jesus<sup>1</sup>, Harald Strauss<sup>2</sup>, Mário A. Gonçalves<sup>1,3</sup>, Michelle Harris<sup>4</sup>, Diogo Silva<sup>3</sup>, Martin J.  
3    Whitehouse<sup>5</sup>, Damon A.H. Teagle<sup>6</sup>

4    1- (Corresponding author) Instituto Dom Luiz. Faculdade de Ciências Universidade Lisboa. Campo Grande C6 piso 1, 1749-016 Lisboa, Portugal.

5    [ana.jesus@fc.ul.pt](mailto:ana.jesus@fc.ul.pt)

6    2- Institute for Geology and Paleontology, University Münster. Correnstr.. 24, 48149 Münster, Germany. [hstrauss@uni-muenster.de](mailto:hstrauss@uni-muenster.de)

7    3- Departamento de Geologia. Faculdade de Ciências Universidade Lisboa. Campo Grande C6 piso 1, 1749-016 Lisboa, Portugal. [mgoncalves@fc.ul.pt](mailto:mgoncalves@fc.ul.pt) ,  
8    [dmfrs.97@gmail.com](mailto:dmfrs.97@gmail.com)

9    4- School of Geography, Earth and Environmental Sciences, Plymouth University. B526 Portland Square, Drake Circus, Plymouth, PL4 8AA, UK.  
10    [michelle.harris@plymouth.ac.uk](mailto:michelle.harris@plymouth.ac.uk)

11    5- Department of Geosciences, Swedish Museum of Natural History, Box 50 007. SE-104 05 Stockholm Sweden. [martin.whitehouse@nrm.se](mailto:martin.whitehouse@nrm.se)

12    6- School of Ocean and Earth Science, National Oceanography Centre Southampton, University of Southampton, European Way, Southampton SO14 3ZH.  
13    UK. [damon.teagle@southampton.ac.uk](mailto:damon.teagle@southampton.ac.uk)

14

15    **Keywords**

16    Multiple sulfur isotopes, Oman Ophiolite, Oceanic Crust, Hydrothermal alteration, Sulfide.

17

18    **Abstract**

19    We present sulfur mineralogy and isotope geochemistry from the gabbro transect of the Oman Drilling  
20    Project to unravel the sulfur cycle during hydrothermal alteration of the plutonic oceanic crust. The  
21    sheeted dike–gabbro transition (Hole GT3A) shows low sulfide-sulfur concentrations (GT3A<sub>median</sub>=178  
22    ppm,  $\sigma=4873$  ppm) but with great sulfur isotope variability ( $\delta^{34}\text{S} = -12.8$  to  $14.4\text{\textperthousand}$  V-CDT, weighted  
23    average  $+5.8\text{\textperthousand}$ ) and unusually heavy compositions relative to in-situ or ophiolitic crust. These features  
24    are consistent with abiogenic thermochemical sulfate reduction during intense hydrothermal alteration  
25    under greenschist facies conditions which formed a low-variance and relatively high-fS<sub>2</sub> assemblage of  
26    pyrite  $\pm$  chalcopyrite  $\pm$  bornite. The heaviest isotope compositions ( $+10$  to  $+14\text{\textperthousand}$ ) occur within 10 m of  
27    the uppermost gabbro screen suggesting focused fluid-rock exchange with isotope enrichment relative  
28    to seawater due to closed-system reservoir effects. The change in isotope compositions from  $+5$  to  $0$   
29     $\text{\textperthousand}$  in the overlying sheeted dike reflect fluids gradually buffered by magmatic sulfur to signatures similar  
30    to the Oman Volcanogenic Massive Sulfide deposits. Hole GT3A represents a deep hydrothermal  
31    reaction zone with extensive S and base metal losses and incorporation of up to  $\sim 80\%$  seawater-  
32    derived sulfate. The amount of Cu and Zn released in a  $1\text{ km}^3$  crustal section similar to Hole GT3A is  
33     $\sim 3$  times greater than the average contents of Omani VMS deposits.

34 The mid to lower crustal section (Holes GT2A and GT1A) mostly preserves MORB sulfur isotope  
35 compositions but highly variable sulfide-sulfur contents (GT2A<sub>median</sub>=454,  $\sigma$ =693 ppm, GT1A<sub>median</sub>=114,  
36  $\sigma$ =277 ppm). Away from fault zones, silicate microvein networks enabled variable sulfide and metal  
37 remobilization. Magmatic sulfides persist as remobilized remnants along with sulfidation reactions and  
38 mild isotopic enrichments ( $<+2.7\text{\textperthousand}$ ) in secondary sulfides (millerite + siegenite-polydimitess + pyrite).  
39 The mid-lower crustal section experienced redistribution of magmatic sulfur mixed with minor inputs of  
40 seawater-derived sulfur ( $<10\%$ ), under very low fluid/rock ratios and moderate sulfur fugacities, that  
41 chiefly preserved base metal abundances in secondary sulfides. The many faulted intervals present in  
42 Holes GT1A and GT2A record near complete sulfur and metal leaching of magmatic sulfides without  
43 the deposition of secondary sulfides but preserve sulfate with a Cretaceous seawater sulfate-sulfur  
44 isotope signature (+16.1 to +17.3‰). These structures are the expression of crustal scale channeled  
45 hydrothermal recharge fluid flow and record a previously unaccounted sulfur budget introduced in the  
46 deep crust.

47

48 **1 INTRODUCTION**

49 Hydrothermal circulation modifies the composition of the oceanic crust by fixing chemical elements such  
50 as magnesium, boron, strontium and sulfur during chemical exchange between seawater and basaltic  
51 rock; these reactions take place under progressively higher temperatures with depth leading to mineral  
52 transformations up to amphibolite facies temperatures (Alt, 1995). Ultimately, the balance between  
53 hydrothermal alteration, submarine volcanic emissions and riverine inputs regulates the composition of  
54 the ocean through time and can modify the mantle through the subduction of altered oceanic crust  
55 (Plank and Manning, 2019). Sulfur is a crucial element for tracing global biogeochemical and planetary  
56 cycles: the mass exchanges and isotopic fractionations of sulfur enable identifying the chemical  
57 pathways and quantify elemental fluxes between surface and endogenous reservoirs within a wide  
58 range of temperatures and redox conditions (Canfield, 2004). Sulfur cycling in the oceanic crust has  
59 been studied on drill core samples obtained through scientific ocean drilling and in ancient oceanic crust  
60 exposed on land in ophiolites. Drilling in the thick crust of fast spreading ridges has intersected the  
61 volcanic rocks and the sheeted dikes (Alt et al., 1989; Alt et al., 1995). However, after more than five  
62 decades of ocean drilling, Ocean Drilling Program Hole 1256D remains the only borehole to reach the  
63 sheeted dike-gabbro transition, intersecting the “high level” or “isotropic” gabbros of the axial melt lens  
64 (Teagle et al., 2010; Wilson et al., 2006). Submersible dives into lower crust exposed by rifting has  
65 enabled mapping and sampling of deep cumulate gabbros formed on the fast spreading East Pacific  
66 Rise (EPR) at Hess Deep (Gillis, 1995; Gillis et al., 2001) and Pito Deep (Barker et al., 2010; Heft et  
67 al., 2008) but intact sections remain un-sampled leading to poor knowledge of magmatic accretion  
68 processes and the associated hydrothermal exchanges (Kelemen et al., 1997; Lecuyer and Reynard,  
69 1996; McCollom and Shock, 1998).

70 Due to these constraints, there is little knowledge of sulfur behaviour in deep plutonic rocks formed at  
71 fast spreading ocean ridges. Evidence shows that the permeable volcanic section of the oceanic crust  
72 experiences low temperature (<100 °C), oxidative alteration that leads to sulfur loss and mild isotopic  
73 enrichments ( $\delta^{34}\text{S} \sim +1.6 \text{ ‰}$ ; ODP Hole 504B, Alt et al., 1989) relative to a canonical MORB mantle  
74 value of  $+0.1 \pm 0.3 \text{ ‰}$  (Sakai et al., 1984).  $\text{H}_2$  produced during iron oxidation can support  
75 chemoautotrophs (Bach and Edwards, 2003) producing large fractionations down to a  $\delta^{34}\text{S}$  value of -  
76 26.1 ‰ in the volcanic section (Troodos; Alt, 1994) resulting from microbial sulfate reduction (MSR)  
77 under open system conditions. Mixing of upwelling hydrothermal fluids with cold seawater can form  
78 sulfide mineralization at the lava-dike transition (Alt et al., 2010), with  $\delta^{34}\text{S}$  values up to  $+3\text{ ‰}$  (Alt et al.,  
79 1989). During active axial hydrothermal circulation, increasing temperatures from greenschist (>250  
80 °C) to lower amphibolitic facies conditions (>350 °C) in the sheeted dikes and the underlying dike-  
81 gabbro transition precludes biologically mediated processes and incorporation of seawater derived  
82 sulfur occurs via thermochemical sulfate reduction (TSR) pathways (Shanks, 2001).

83 Sulfur isotopic enrichments documented in the intrusive upper crustal section are significantly higher in  
84 ophiolites (<+10‰; Alt, 1994) compared to those observed in modern crust (<+3.1‰, Alt et al., 1989;  
85 Alt et al., 1995; Barker et al., 2010). Furthermore, the dike–gabbro transition is thought to represent the  
86 reaction zone where metals for the genesis of Volcanogenic Massive Sulfide (VMS) deposits are

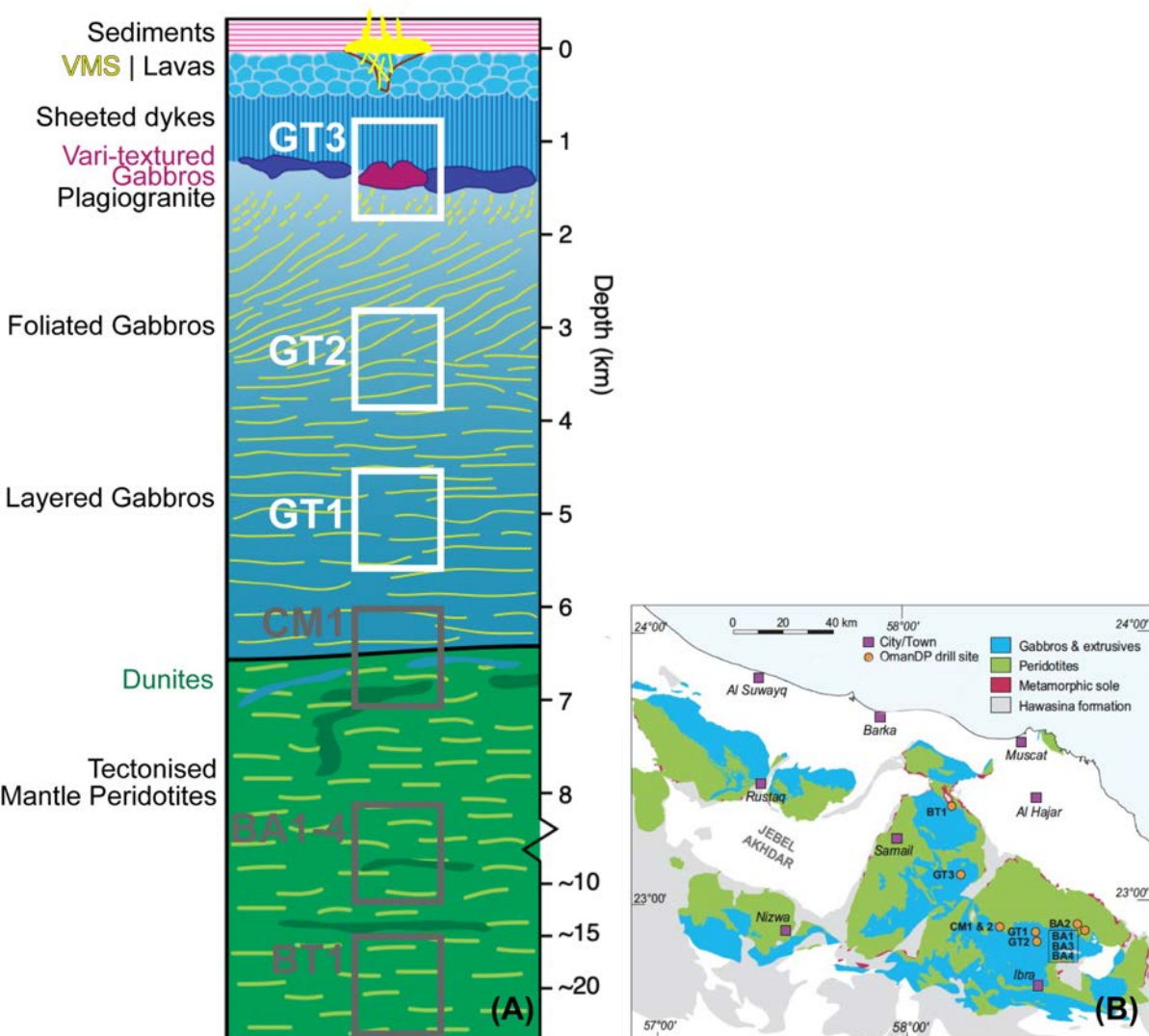
87 sourced (Alt, 1995; Hannington, 2014). Epidosites, mineral associations of granoblastic epidote-quartz-  
88 titanite, have long been considered to represent the depleted endmembers of sulfur and metal leaching  
89 at the deep reaction zone. Despite clear evidence for metal mobilization in in-situ oceanic crust (Alt et  
90 al., 2010; Alt et al., 1996; Gillis, 1995; Gillis et al., 2001; Heft et al., 2008; Patten et al., 2016), epidosites  
91 have only been documented in ophiolites (Harper et al., 1988; Jowitt et al., 2012; Nehlig et al., 1994;  
92 Richardson et al., 1987; Harris et al., 2015). Recent work in the Oman ophiolite has challenged the view  
93 that epidosites are restricted to the deep reaction zone (Gilgen et al., 2016) and proposed that they are  
94 formed by late, oxidized, Fe-poor fluids, unlikely to form VMS deposits (Richter and Diamond, 2022).

95 Differences between in-situ oceanic and ophiolitic lower crustal sections are seemingly less  
96 pronounced. However, sampling deep crustal sections of in-situ oceanic crust is restricted to tectonically  
97 exposed sections, most common on slow-spreading ridges. Uplifted sections of lower crust that are  
98 directly exposed to seawater can display oxidative, lower temperature alteration enabling MSR  
99 processes (Alford et al., 2011). Otherwise, sulfur isotopic enrichments decrease throughout the  
100 gabbroic lower crust towards values below +2.5‰ although sections affected by channeled fluid flow  
101 may record heavier isotopic compositions (ca. +6‰ Alt, 1994; Puchelt et al., 1996; Delacour et al.,  
102 2008a; Delacour et al., 2008b)

103 The Samail Ophiolite in the Sultanate of Oman (Figure 1B) provides a unique sample of the oceanic  
104 crust and upper mantle exposed on land that has been extensively studied since the late 1970's. The  
105 International Continental Scientific Drilling Program (ICDP) Oman Drilling Project (OmanDP; Kelemen  
106 et al., 2020) enabled unprecedented, continuous sampling of critical sections of the ophiolite crust and  
107 mantle through drilling of a number of short ( $\leq 400$  m) diamond coring drill holes from representative  
108 sections of the mid- to lower plutonic crust of the Samail ophiolite (Figure 1A). Sulfide minerals are easily  
109 modified by oxidation and weathering processes under surface conditions, therefore OmanDP samples  
110 provide an exceptional opportunity to investigate sulfur and metal cycling in pristine rocks from the  
111 oceanic crust. A profile in the Samail Ophiolite based on surface samples by Oeser et al. (2012) showed  
112 elevated  $\delta^{34}\text{S}$  values (up to +5 ‰) and low sulfide S-contents in the dike-gabbro transition that were  
113 attributed to TSR followed by oxidation and leaching; the lower crust and mantle section preserved  
114 near-MORB  $\delta^{34}\text{S}$  values and non-zero, mildly negative  $\Delta^{33}\text{S}$  values (down to -0.042‰). Building on  
115 Oeser et al. (2012) findings, we present detailed sulfide mineralogy and results from whole-rock sulfur  
116 isotope geochemistry complemented with data from in-situ techniques covering a representative profile  
117 of the intrusive oceanic crust including: 1) the upper crustal sheeted dike complex and the transition to  
118 the high level gabbros (Hole GT3A); 2) the mid-crustal section at the transition from foliated to layered  
119 gabbros (Hole GT2A) and; 3) a sequence of lower crustal layered gabbros (Hole GT1A) about 1000 m  
120 stratigraphically above the crust-mantle transition zone. To understand the pathways and isotopic  
121 fractionation mechanisms of sulfur from magmatic conditions throughout the various stages of oceanic  
122 hydrothermal alteration, our sampling covers a spectrum from fresh rocks to those recording moderate  
123 to complete hydrothermal recrystallisation, including highly deformed rocks from deep oceanic fault-  
124 zones crosscutting the layered gabbros (Zihlmann et al., 2018). Finally, to assess the metal mobility

125 and elucidate on the potential source rocks for VMS deposits, we make use of comprehensive whole-  
126 rock profiles obtained during core logging by the OmanDP science team (Kelemen et al., 2020).

127



141 **2.1 The Samail Ophiolite and current views on the oceanic crust accretion and alteration**

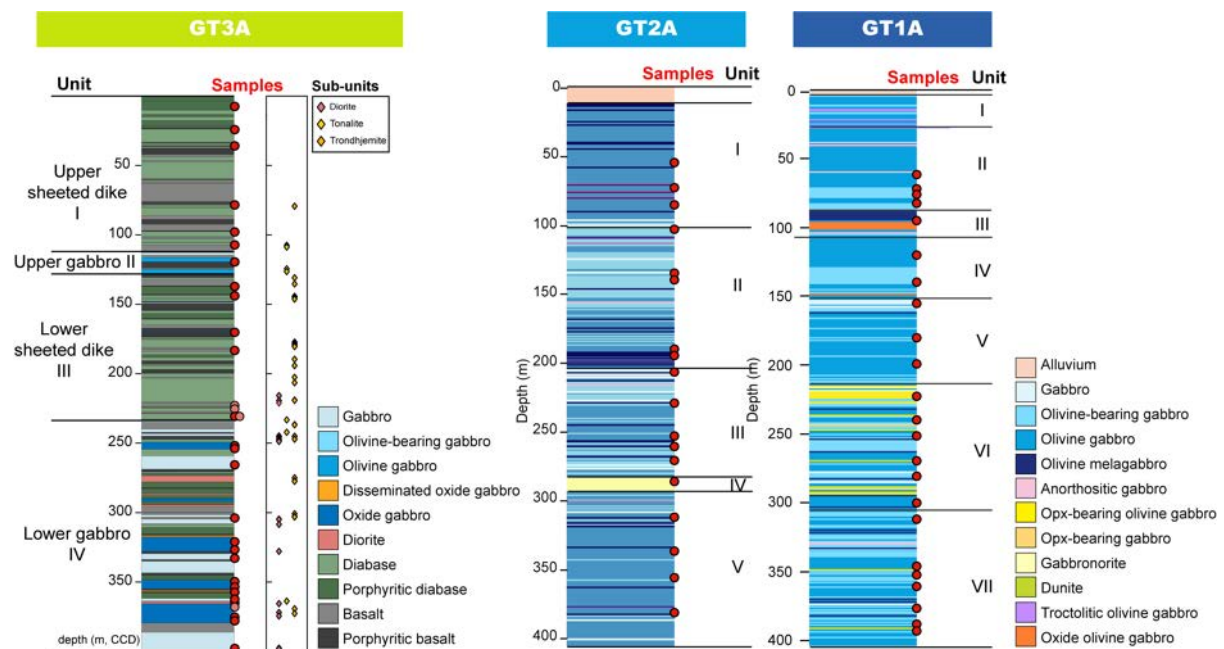
142 The Samail Ophiolite represents an exceptionally large fragment of the Tethyan ocean lithosphere with  
143 ca 500 km long, 200 km width and 2-20 km thickness that was preserved from post-obduction tectono-  
144 metamorphic events (Nicolas et al., 2000). Its classic Penrose stratigraphy (Anonymous, 1972) became  
145 the template for the structure of the oceanic crust in fast-spreading ridges such as the EPR (Pallister  
146 and Hopson, 1981). The ophiolite records a polygenetic history (Alabaster et al., 1982) starting with a  
147 main axial stage of crustal accretion, during which the Penrose-like crustal architecture was developed  
148 and the voluminous V1-Geotimes axial lavas erupted. A second magmatic stage comprises  
149 incompatible element depleted, low-Ti off-axis volcanism (V2 lavas) and late intrusives (gabbronorites,  
150 wehrlites; Benoit et al., 1996; Koepke et al., 2009), consistent with hydrous melting of a progressively  
151 depleted mantle source. This evolution has led to considerable debate about whether the Samail  
152 ophiolite was formed at a typical Mid-Ocean Ridge (MOR) or in a subduction initiation setting (Belgrano  
153 et al., 2019; Godard et al., 2006; Lippard, 1986). Zircon U/Pb dating place axial magmatism at 96 Ma  
154 whereas post-ridge magmatic activity extended until 95 Ma (Rioux et al., 2021).

155 Current views on the oceanic crust are based on seminal geological and geophysical observations on  
156 the seafloor and ophiolites (Alt, 1995). They propose that fast-spreading ridges comprise an upper crust  
157 with ca. 3 km where lavas grade into the sheeted dike complex via a ~100 to 300 m-thick transition  
158 zone where subvertical dikes are increasingly common. The dike complex roots into a thin axial melt  
159 lens (AML; MacLeod and Yaouancq, 2000; Gillis, 2008) the level of which can vary dynamically through  
160 time due to eruption/replenishment cycles (Coogan et al., 2003). The AML is overlain by a thermal  
161 boundary layer that separates the vigorous hydrothermal convective system responsible for the  
162 generation of seafloor hydrothermalism and SMS/VMS deposits (France et al., 2009; Wilson et al.,  
163 2006) from the underlying deeper hydrothermal system affecting the lower crust.

164 Much of the lower crust beneath the ridge is in a mushy state, down to the Moho Transition Zone (MTZ).  
165 The exact mechanism of crustal accretion continues to be debated (e.g., Coogan et al., 2006; Zhang et  
166 al., 2021) and is strongly dependent on the mechanisms for cooling of the crust and the geometry of  
167 hydrothermal circulation. Potential processes for heat removal of the lower crust include a millimeter-  
168 scale inter- and transgranular vein networks infilled with amphibole (Bosch et al., 2004; Manning et al.,  
169 2000). Because these may not be sufficient to extract heat from depth, large scale corridors of focused  
170 fluid flow extending from the base of the sheeted dike down to the MTZ under greenschist facies (~300  
171 °C) up to very high temperature conditions (~880°C) have also been proposed, (Coogan et al., 2006;  
172 Zihlmann et al., 2018). Noticeable examples of such corridors in Oman are the Al Asih (Abily et al.,  
173 2011) and Zihlmann-Müller- fault zone-ZMFZ (Zihlmann et al., 2018) where cooling was largely  
174 facilitated by introduction of seawater-derived hydrothermal fluids to great large depths in the crust  
175 resulting in the cooling from magmatic conditions to greenschist facies temperatures.

176 **2.2 Main features of drillholes OmanDP Holes GT1A, GT2A, GT3A**

177 The three OmanDP drillholes investigated were diamond-cored to ~400 m and petrographically and  
 178 instrumentally described to better than scientific ocean drilling standards (Kelemen et al., 2020) (Figure  
 179 2). The lower crustal (GT1) and mid-crustal sites (GT2) are located in Wadi Gideah (Tayin Massif) and  
 180 estimated to lie ~1400 m and ~3300 m above the (crust-)Mantle Transition Zone (MTZ), respectively  
 181 (Figure 1, Figure 2). The gabbro-dike transition site (GT3) is located in Wadi Aswad in the Samail Massif,  
 182 approximately 40 km west of Wadi Gideah and is estimated to be collared ~4100 m above the MTZ. All  
 183 drill sites are located in domains without the influence of the second (V2) magmatic stage magmatism  
 184 and their magmatic features document the V1 crustal accretion stage of the Samail paleoridge  
 185 (Goodenough et al., 2014). All drilling depths refer to the *Chikyu Curated Depth* (CCD) scale (Kelemen  
 186 et al. (2020).



201 Hole GT3A sampled the dike-gabbro transition, and is subdivided into four major magmatic units (Figure  
202 2) including an Upper and Lower Sheeted Dike sequence with more than 95% steeply dipping dikes  
203 with mean thickness estimated to be 0.58 m comprising (porphyritic) diabase with chilled, basaltic to  
204 glassy margins . These dikes are separated by two gabbro sequences which nonetheless include  
205 significant amounts of dikes (~46.5%) but have distinctive petrography. The thin Upper Gabbro (111.02  
206 to 127.89 m downhole) is dominantly olivine (bearing) gabbro whereas oxide (disseminated) gabbro  
207 prevails in the Lower Gabbro (from 233.84 m). Swarms of dikelets and magmatic breccias of tonalite  
208 and diorite occur at the transition from the Lower Dikes to the Upper Gabbro sequence, wherein oxide  
209 gabbros grade upward to leucodiorite. Dike-gabbro crosscutting relationships suggest that the Upper  
210 Gabbro represents a younger paleolevel of the AML relative to the highly differentiated oxide gabbros  
211 of the Lower Gabbro Sequence (Kelemen et al., 2020; Engelhardt et al., 2022; France et al., 2021).  
212 Unlike ODP Hole 1256D (Wilson et al., 2006; Alt et al., 2010) no continuous region of granoblastic  
213 hornfels resulting from contact metamorphism of the dikes was present in Hole GT3A although  
214 granoblastic patches have been reported in the surrounding outcrops (France et al., 2021).  
215 Microgranular domains with granoblastic textures representing stopped blocks of hydrothermally  
216 altered and metamorphosed dikes are present at ~243 m (Engelhardt et al., 2022) and 323-326 m  
217 depths in Hole GT3A (Kelemen et al., 2020) (Figure 2).

218

## 219 **2.2.2 Alteration and deformation**

220 Total alteration, defined as the weighted average of background alteration plus patches, vein halos and  
221 deformation-related alteration, is higher in Holes GT1A (60%) and GT3A (54%) than in Hole GT2A  
222 (44%). All sections record early alteration under amphibolite facies conditions (brown amphibole),  
223 progressing through greenschist (green amphibole+chlorite+albite+epidote) and late sub-greenschist  
224 facies (zeolites+prehnite+calcite) (Kelemen et al., 2020).

225 Brown amphibole blebs replace clinopyroxene in Holes GT1A and 2A and are less common in Hole  
226 GT3A (Engelhardt et al., 2022), where fibrous green amphibole is the most common mineral  
227 pseudomorphically replacing clinopyroxene. Olivine is replaced by chlorite + oxides (rarely serpentine)  
228 although in Hole GT2A, talc or brown phyllosilicates are also common. Rare olivine phenocrysts in the  
229 Hole GT3A diabase or in the matrix of olivine gabbros are completely replaced by mixtures of smectite-  
230 chlorite + actinolite + opaques. Epidote (s.l.) is significantly more common in Hole GT3A, where it  
231 extensively replaces igneous plagioclase in several intervals; plagioclase is also extensively replaced  
232 by albite or zeolites (thompsonite; also present in Holes GT1A and GT2A). In the lower/mid-crustal  
233 sections (GT1A-GT2A), plagioclase is more commonly replaced by chlorite, whereas albitization  
234 prevails in intensely altered intervals with loss of primary texture. Most Hole GT2A rocks feature an  
235 intergranular chlorite vein network that replaces plagioclase along the margins of microcracks.  
236 Downhole variations are conspicuous for few alteration minerals: i) calcite and oxy-hydroxides are more  
237 common in the uppermost part of each hole and; ii) Hole GT3A features a clear downhole increase in  
238 epidote±prehnite (Kelemen et al., 2020).

239 Vein mineral fill and associated halos follows the relative order of formation outlined above. Vein  
240 densities increase towards fault zones and deformation-related alteration is most commonly associated  
241 with lower temperature, sub-greenschist mineral paragenesis (~270 – 100 °C). Additionally, Holes  
242 GT1A and GT2A have wide (2-10 m) intervals of fault rock with associated anhydrite veins (Kelemen  
243 et al., 2020; Teagle et al., 2019).

244 Pre-drilling site survey geological mapping identified a 251/55°SE structure (Zihlmann et al., 2018) ca.  
245 300 m north-east of Site GT1 named Zihlmann-Müller- Fault Zone (ZMFZ; Kelemen et al., 2020). This  
246 normal fault zone with convincing syn-oceanic origin comprises ~1 m fault-gauge and a > 4 m alteration  
247 halo ranging from greenschist (chlorite-epidote) to zeolite facies (carbonate-zeolite) conditions with  
248 formation of pyrite ± chalcopyrite. Copper slags from ancient ore processing are common in the vicinity.  
249 The ZMFZ was projected to be intersected by Hole GT1A between 145-310 m depth and is likely one  
250 of the main fault structures identified at ca. 200 m. However, unexpectedly Hole GT1A intersected 7  
251 major fault zones and 14 minor structures with associated intense deformation, alteration and veining,  
252 so the exact correlation to the ZMFZ is not possible. Hole GT2A includes 20 main fault-zones and a  
253 total >250 m of moderate to complete brittle deformation, more evenly distributed than in Hole GT1A  
254 (see

255 **Figure 5B**, ahead). In Hole GT3A deformation is most commonly concentrated along dike margins and  
256 postdates vein formation or is contemporaneous with the latest zeolite vein generation. The intervals  
257 with most significant brittle deformation and veining are between 160-200 m and 360-400 m (**Figure 2**).

### 258 3 METHODS

#### 259 3.1 Sampling strategy and sample preparation

260 Sampling took place aboard R/V *Chikyu* during ChikyuOman2017 Phase 1 core logging activities  
261 (Kelemen et al., 2020). Most samples were quarter cores with lengths between 5 cm (for HQ=63.5 mm  
262 diameter) and 10 cm (for NQ=47.6 mm diameter). 73 samples were selected for mineralogical study  
263 and S isotopic characterization distributed amongst Holes GT1A, GT2A and GT3A, with care taken to  
264 avoid the uppermost weathered intervals and focusing on intervals with visible sulfide (Table 1). Sample  
265 referencing follows the original on-site labelling during core handling and curation (Kelemen et al.,  
266 2020).

267 Following macroscopic description, thin section billets were made from representative portions of the  
268 sample and the remainder core powdered at the Geology Department Faculdade Ciências Lisboa/IDL,  
269 for whole-rock sulfur geochemical analysis. Samples were split with diamond saws and all surfaces  
270 abraded in emery wheels to remove any metal contaminants. Whole-rock powders for sulfur elemental  
271 and isotopic analysis were obtained by coarse crushing in a hardened steel roll crusher and final  
272 pulverization in an agate mill.

#### 273 3.2 Petrography and mineralogy

274 Due to microscopic scale variations in alteration and sulfide distribution, the samples processed for  
275 sulfur isotopic geochemistry were studied in detail. Petrographic analysis of polished thin sections took  
276 place under transmitted and reflected light, enabling visual estimates of: 1) total alteration % by

277 weighted average of each magmatic mineral species; 2) modes for remobilized, magmatic and  
278 hydrothermal sulfide, as reported in section 4.1. Total alteration % does not include veins and can thus  
279 be considered as a minimum estimate for each thin section. Total sulfide modes were determined by  
280 image analysis using Leica Software by averaging 3 random areas. All data are available in  
281 Supplementary Material 1 (SM 1, Table 1).

### 282 **3.3 Electron Probe Micro-analysis**

283 Petrographic observations reported in this work were validated via Electron Microprobe analysis of  
284 silicate (unpublished results) and sulfide mineral assemblages Supplementary Material SM1 (Table 2).  
285 Mineral major element compositions were determined on polished sections, covered in a 20 nm-thick  
286 carbon coating at the Geology Department Faculdade Ciências Lisboa/IDL using a JEOL-JXA 8200  
287 electron probe microanalyzer (EPMA) equipped with four wavelength-dispersive spectrometers (WDS)  
288 , six analyzer crystals (LIF, LIFH, PET, PETH, TAP and LDED2), secondary and back-scattered  
289 electron detectors, and an energy-dispersive spectrometer (EDS). Measurements were made with a  
290 20s acquisition time for the peaks, and 5s for the background. The accelerating voltage was 15keV,  
291 with a beam current of 25nA and a beam diameter of 5µm. Natural mineral and metallic standards from  
292 Astimex Scientific Ltd were used.

293

### 294 **3.4 Sulfur isotopes- whole rock**

295 Sulfur extraction, measurements and isotope analyses were performed at the Institut für Geologie und  
296 Paläontologie, University of Münster. Total sulfur concentrations ( $TS_{Meas}$ ) were measured using an Eltra  
297 CS-580 sulfur/carbon analyzer with a detection limit of 0.01 wt% and an estimated analytical uncertainty  
298 of 3 % relative. 10-20 mg of whole-rock powder was combusted at 1350 °C in a porcelain crucible under  
299 an O<sub>2</sub>-atmosphere. These data were used to determine the amount of sample for the sequential sulfur  
300 extractions and to assess if the extractions were complete. All sulfur concentrations in the text refer to  
301 those obtained by gravimetry, as described below.

302 Sulfur extraction for subsequent isotope analyses was performed by a sequential wet chemical  
303 procedure. Acid Volatile Sulfides (AVS, including monosulfide phases such as pyrrhotite or sphalerite)  
304 and Cr-reducible Sulfur (CRS, including disulfides such as pyrite, chalcopyrite or bornite), were  
305 extracted in closed glass digestion vessels under a N<sub>2</sub>-atmosphere using 6M HCl and 1M CrCl<sub>2</sub>-HCl,  
306 respectively (Canfield et al., 1986; Rice et al., 1993). Released H<sub>2</sub>S was firstly precipitated as ZnS in a  
307 3% acetic zinc acetate solution and then as silver sulfide (Ag<sub>2</sub>S) using a 0.1 M AgNO<sub>3</sub> solution. The  
308 sample residue following the AVS-CRS extraction ( $TS_{sulfide}$ =AVS+CRS) was filtered and acid-soluble  
309 sulfate ( $TS_{SO4}$ ) was precipitated as BaSO<sub>4</sub> using an 8.5% BaCl<sub>2</sub> solution. The mass of each sulfur  
310 species was determined via gravimetry, their sum representing the total sulfur extracted:  
311  $TS_{Ext}=TS_{sulfide}(AVS+CRS)+TS_{SO4}$ . Comparison of total sulfur extracted wet-chemically ( $TS_{Ext}$ ) with that  
312 measured using the sulfur/carbon analyzer provides excellent agreement ( $r = 0.99$ ) with deviations  
313 mostly for samples with low S concentration (S <500 ppm) that approach the lower detection limit of the  
314 Eltra furnace (SM2, Fig. 1).

315  $\delta^{34}\text{S}$  was determined for all three sulfur species using a ThermoScientific Delta V Advantage mass  
316 spectrometer coupled with a Flash EA IsoLink elemental analyzer. Between 0.290 and 0.440 mg of  
317 sample were combusted with vanadium pentoxide in tin capsules along with the standards IAEA-S1, -  
318 S2, -S3 and NBS127 for calibration. Results are reported in the common  $\delta$  notation relative to Vienna  
319 Canyon Diablo Troilite (V-CDT):

320

321 *Eq. 1* 
$$\delta^{34}\text{S}_{\text{sample}} = [(\text{sample}/^{34}\text{S}/^{32}\text{S})_{\text{sample}} / (^{34}\text{S}/^{32}\text{S})_{\text{V-CDT}} - 1] \times 1000.$$

322

323 Reproducibility for  $\delta^{34}\text{S}$  values was better than  $\pm 0.3\text{\textperthousand}$  ( $1\sigma$ ). Whenever no visible amount of  $\text{H}_2\text{S}$  from  
324 AVS species was released (i.e. no  $\text{ZnS}$  precipitate in the vials) CRS was collected subsequently in the  
325 same vial and combined with AVS traces for sulfur isotope analysis.

326 Representative samples were selected for multiple sulfur isotopes ( $^{32}\text{S}$ ,  $^{33}\text{S}$ ,  $^{34}\text{S}$ ) measurements using  
327 a ThermoScientific Mat 253 mass spectrometer coupled to a fluorination line. Between 2 and 3 mg  $\text{Ag}_2\text{S}$   
328 was converted to  $\text{SF}_6$  via fluorination at  $300^\circ\text{C}$  overnight in nickel reactors.  $\text{SF}_6$  was cryogenically and  
329 chromatographically purified and then introduced into the mass spectrometer via a dual inlet system  
330 and masses 127, 128, and 129 (representing  $^{32}\text{S}$ ,  $^{33}\text{S}$ , and  $^{34}\text{S}$ , respectively) measured simultaneously  
331 (Peters et al., 2011). The IAEA-S1 standard was used as reference material. Following Farquhar et al.  
332 (2000), Peters et al. (2010) and Peters et al. (2011)  $\Delta^{33}\text{S}$  is defined as (*Eq. 2*).

333

334 *Eq. 2* 
$$\Delta^{33}\text{S} = \delta^{33}\text{S} - 1000 \times [(1 + \delta^{34}\text{S}/1000)^{0.515} - 1].$$

335

336 Reproducibility for  $\Delta^{33}\text{S}$  measurements is better than  $\pm 0.008\text{\textperthousand}$  ( $1\sigma$ ).

337

### 338 **3.5 In-situ sulfur isotopes**

339 In-situ measurements in pyrite, pyrrhotite and chalcopyrite were performed on sub-sampled portions of  
340 previously studied thin sections representative of the three drillholes at the NordSIMS laboratory,  
341 Swedish Museum of Natural History, Stockholm. Mounts with the cut fragments were polished, gold  
342 coated, and then analyzed for  $\delta^{34}\text{S}$  using a CAMECA IMS-1280 large-geometry secondary ion mass  
343 spectrometer (LG-SIMS). The method broadly followed that described by Whitehouse et al. (2005) and  
344 Whitehouse (2013). A 20 keV impact energy,  $\sim 6 \mu\text{m}$ -sized, critically focused beam of  $^{133}\text{Cs}^+$  ions,  
345 rastered over  $10 \times 10 \mu\text{m}$  to homogenise the crater base, was used to locally sputter and ionize S from  
346 individual pyrite grains. A low energy electron flooding gun was used to prevent charge buildup on  
347 adjacent, non-conducting matrix phases and/or inclusions. The  $^{32}\text{S}$  and  $^{34}\text{S}$  isotopes were separated  
348 using an NMR-regulated magnetic field and detected in two Faraday detectors operating at a mass  
349 resolution of 2430 ( $\text{M}/\Delta\text{M}$ ). Matrix matched reference materials were regularly interspersed with the  
350 analyses of unknowns and used to determine instrumental mass bias in order to derive the correct

351 values of  $\delta^{34}\text{S}_{\text{V-CDT}}$ . These reference materials were for pyrite Ruttan (Crowe and Vaughan, 1996;  
352 recalibrated by Cabral et al., 2013) and S0302A (Liseroudi et al., 2021 Liseroudi et al., 2021); for  
353 chalcopyrite Nifty-B (LaFlamme et al., 2016); and for pyrrhotite YP-136 (Li et al., 2019) or MV1  
354 (Whitehouse et al., 2013). Reproducibility (1 std. deviation) based on the frequent standard  
355 measurements in each analytical session (= sample mount) was propagated together with the within  
356 run uncertainties to yield the overall uncertainty on  $\delta^{34}\text{S}$  for a given analysis, as reported in **Table 3**.

357 **4 RESULTS**

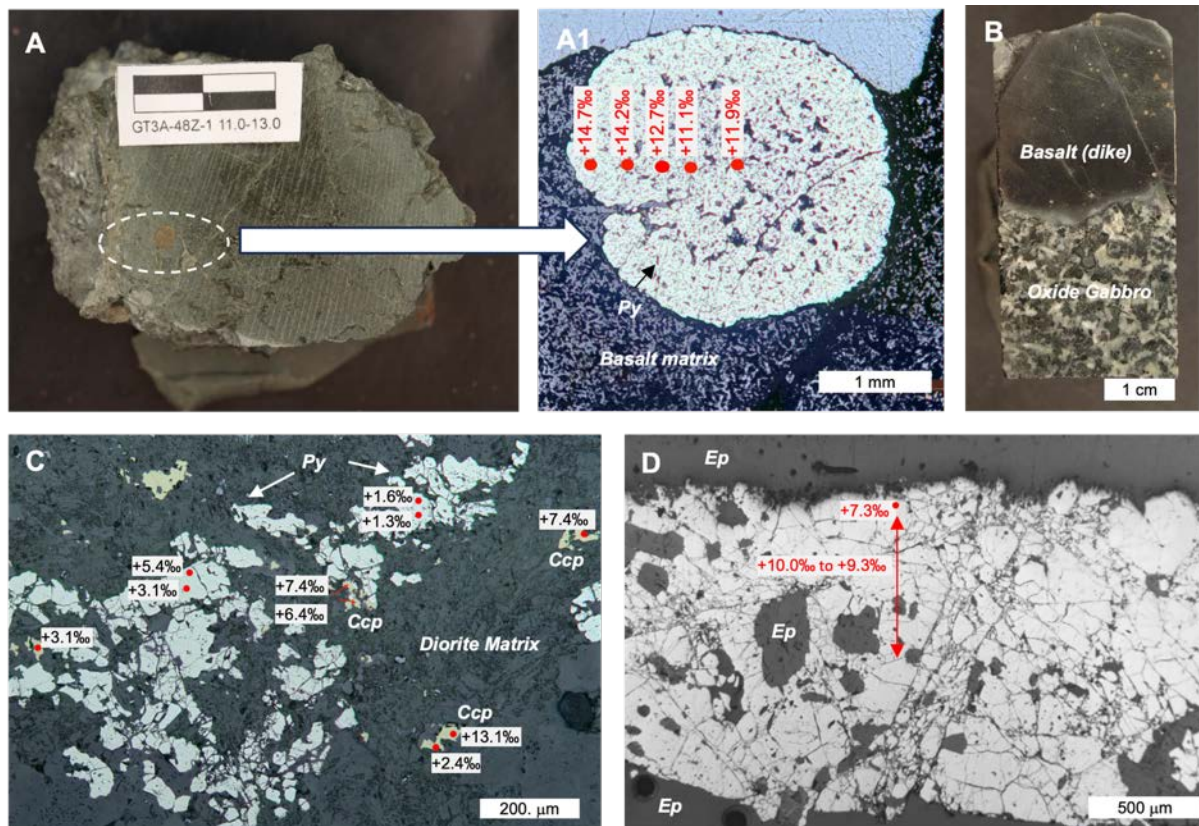
358 **4.1 Sulfide mineralogy**

359 Sulfides were classified based on their micro-textures and associated paragenesis. *Magmatic sulfides*  
360 form blebs or larger, smooth-surfaced, interstitial aggregates of pyrrhotite with chalcopyrite and  
361 pentlandite which occurs as exsolutions or granular aggregates (**Figure 4C**). *Remobilized sulfides* are  
362 magmatic sulfides that preserve their original mineralogy but were partly replaced by secondary  
363 silicates (amphibole, chlorite) during hydrothermal alteration, without formation of secondary sulfide  
364 phases. They can be recognized by their ragged edges and the outline of the original aggregate, with  
365 some outlined by micron sulfide remnants intergrown with the hydrous silicates (**Figure 4D, E**).  
366 Newformed sulfides were labelled as *hydrothermal* (**Figure 4G-H**) and can be found replacing silicates,  
367 magmatic sulfides or in veinlets. Hydrothermal sulfides that can be identified as partially or totally  
368 replacing preexisting magmatic sulfide assemblages were further sub-divided as *hydrothermal-*  
369 *metasomatic* (**Figure 4F**).

370

371 **Figure 5** shows the relative vol% of magmatic, remobilized and hydrothermal (including metasomatic)  
372 sulfides in a composite downhole plot. Sulfides from the dike-gabbro transition zone (Hole GT3A) are  
373 scarce only exceeding 1 %vol on few intervals: 97-120, 222.8, 253-258 m and in the lowermost ~42 m  
374 (357.6 to 375 m;

375 **Figure 5A**). The most strongly sulfide mineralized interval is a pyrite-epidote patch at 362.2 m in the  
376 Lower Gabbro Sequence (**Figure 3D**). All sulfides identified are hydrothermal except for within a diabase  
377 at 6.6 m (sample GT3A-9Z-1 7-12 cm) where minute fragments of pyrrhotite are preserved within  
378 amphibole replacing clinopyroxene. Sulfide blebs are common at the contacts between (glassy) basalt  
379 crosscutting gabbro or diorite. Within the Upper Dike sequence some blebs are large, up to 1-3 mm  
380 (**Figure 3A-A1**) whereas in the Lower Dike and Gabbro sequences they form arrays bordering lithological  
381 contacts (**Figure 3B**). The blebs correspond to porous/spongy pyrite aggregates overgrowing the altered  
382 matrix and their shape and mode of occurrence strongly suggests they are the result of pseudomorphic  
383 replacement of preexisting magmatic sulfides. Pyrite dominates the sulfide assemblage down to ~300  
384 m, most commonly as small porous/spongy grains overgrowing the intensely altered silicate  
385 assemblage, and more rarely as shattered crystals within cataclastic bands. Pyrite in Hole GT3A is  
386 close to an ideal composition (**Figure 6A-B**), with minor elevated Co concentration relative to other  
387 analyzed metals (**Figure 6C**). Chalcopyrite is rare and occurs as small granular or dusty aggregates and  
388 becomes more abundant below ~300 CCD (**Figure 3C**), commonly associated with epidote. Some  
389 chalcopyrite is altered to bornite.



390

391 **Figure 3.** Hole GT3A sulfide mineralogy with spots showing locations of SIMS analyses. **(A-A1)** Basalt with large magmatic bleb  
 392 replaced by pyrite (GT3A-48Z-1 11-13 cm, Upper Dike; 97 m). **(B)** Basalt in dike crosscutting oxide gabbro (GT3-101Z-3 66-71  
 393 cm, Lower Gabbro- 254 m) with multiple magmatic blebs replaced by pyrite (Py). **(C)** Pyrite – chalcopyrite (Ccp) in diorite (GT3-  
 394 142Z-3 4-10 cm; Lower Gabbro- 364 m). **(D)** Pyrite-epidote patch in gabbro, (GT3-141Z-4 61-69 cm; Lower Gabbro- 362 m).

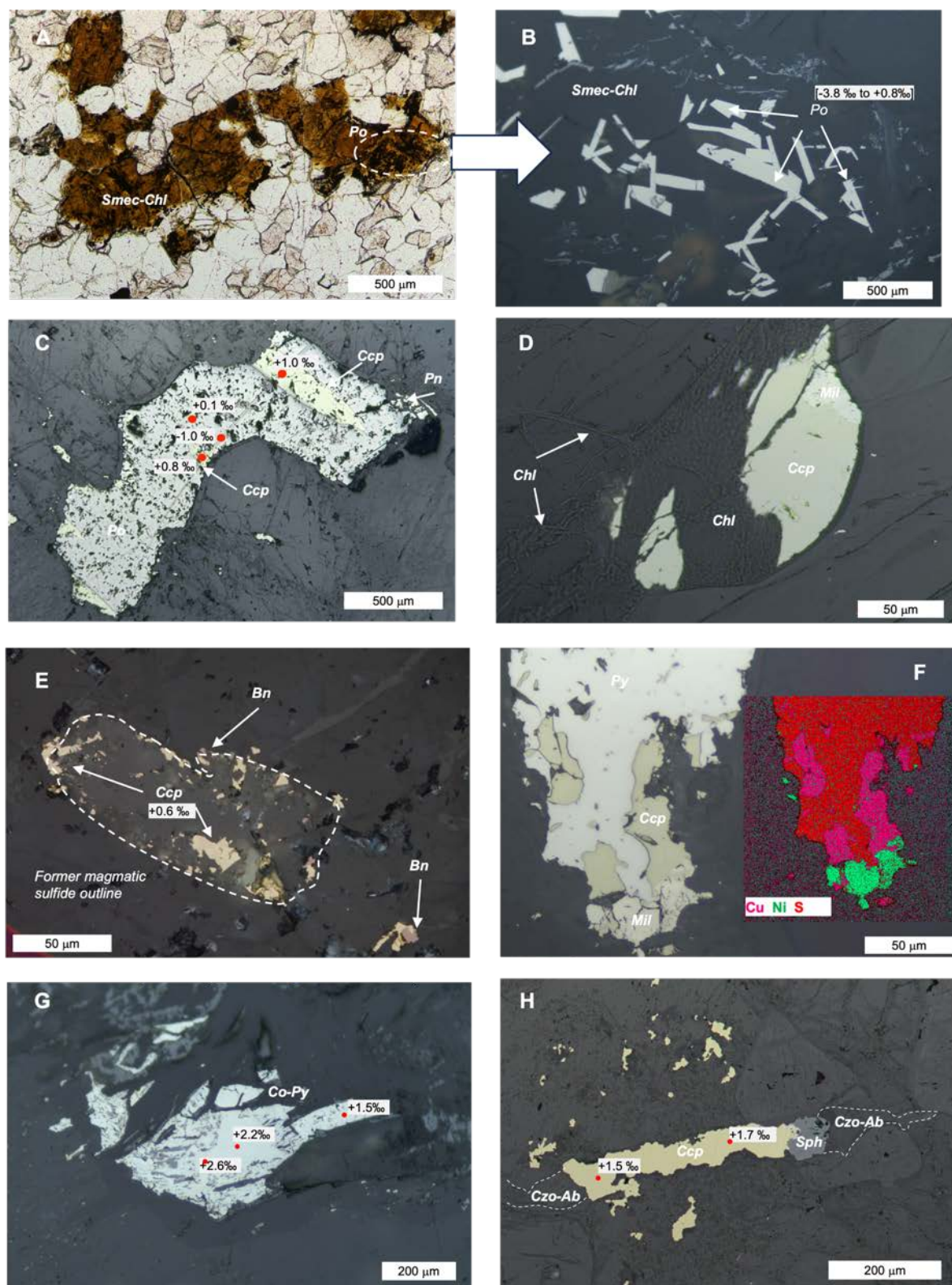
395

396

397

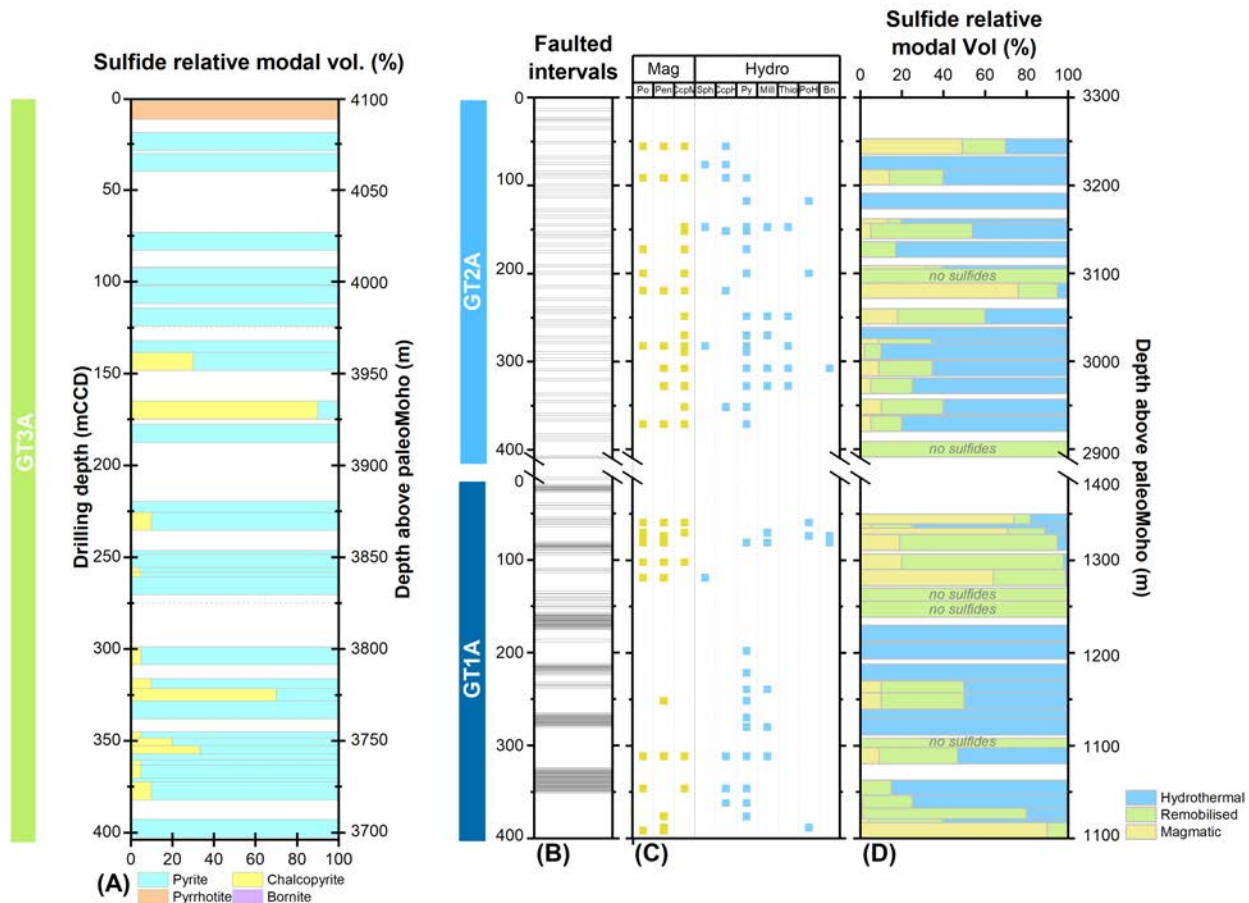
398

399



402 **Figure 4.** Sulfide mineralogy in Holes GT1A and GT2A with spots showing location of SIMS analyses (A-B) Smectite-chlorite  
 403 (Smech-Chl), replacing olivine enclosing pyrrhotite (Po) platelets (GT2-45Z1 32-35 cm; 117.6 m). (C) Magmatic sulfide pyrrhotite  
 404 - chalcopyrite (Ccp) – pentlandite (remobilized- Pn) (GT1-31Z-2 20-25 cm; 73.9 m). (D) Metasomatic sulfide chalcopyrite –  
 405 millerite (Mil) replaced by chlorite (Chl) (GT2-100Z-4 14-17 cm; 270.4 m); (E) Remobilized sulfide with chalcopyrite remnants,

406 partly oxidized to bornite (*Bn*) (GT1-30Z-1 55-60 cm; 70.4 m); **(F)** Metasomatic sulfide pyrite-millerite-chalcopyrite showing EDS  
 407 compositional map (GT2-55Z2 63-65 cm; 147.4 m); **(G)** Hydrothermal chalcopyrite-sphalerite (*Sph*) vein with albite (*Ab*) and  
 408 clinozoisite (*Czo*) (GT2A-31Z-1 68-70 cm; 76 m).



409 **Figure 5.** Sulfide mineralogy variations with depth. **(A)** Hole GT3A relative modal volume % of sulfide. With the exception of the  
 410 uppermost sample, all sulfides are hydrothermal. **(B-D)** Hole GT1A and GT2A showing: **(B)** Faulted intervals, **(C)** Individual sulfide  
 411 minerals, shown as present or absent since modal amounts are very low and, **(D)** relative modal volume sulfides (%) shown for  
 412 magmatic vs. remobilized or hydrothermal (including metasomatic, see text). Abbreviations: *Mag*-magmatic, *Hydro*- hydrothermal  
 413 *Po*- pyrrhotite, *Pn*-pentlandite, *Ccp*- chalcopyrite, *Sph*- sphalerite, *Py*- pyrite, *Mil*- millerite, *Thi*- thiospinels (polydymite-  
 414 siegenitess), *Bn*- bornite. All depth scales in m-CCD (*Chikyu Curated Depth* as in Kelemen et al., 2020).

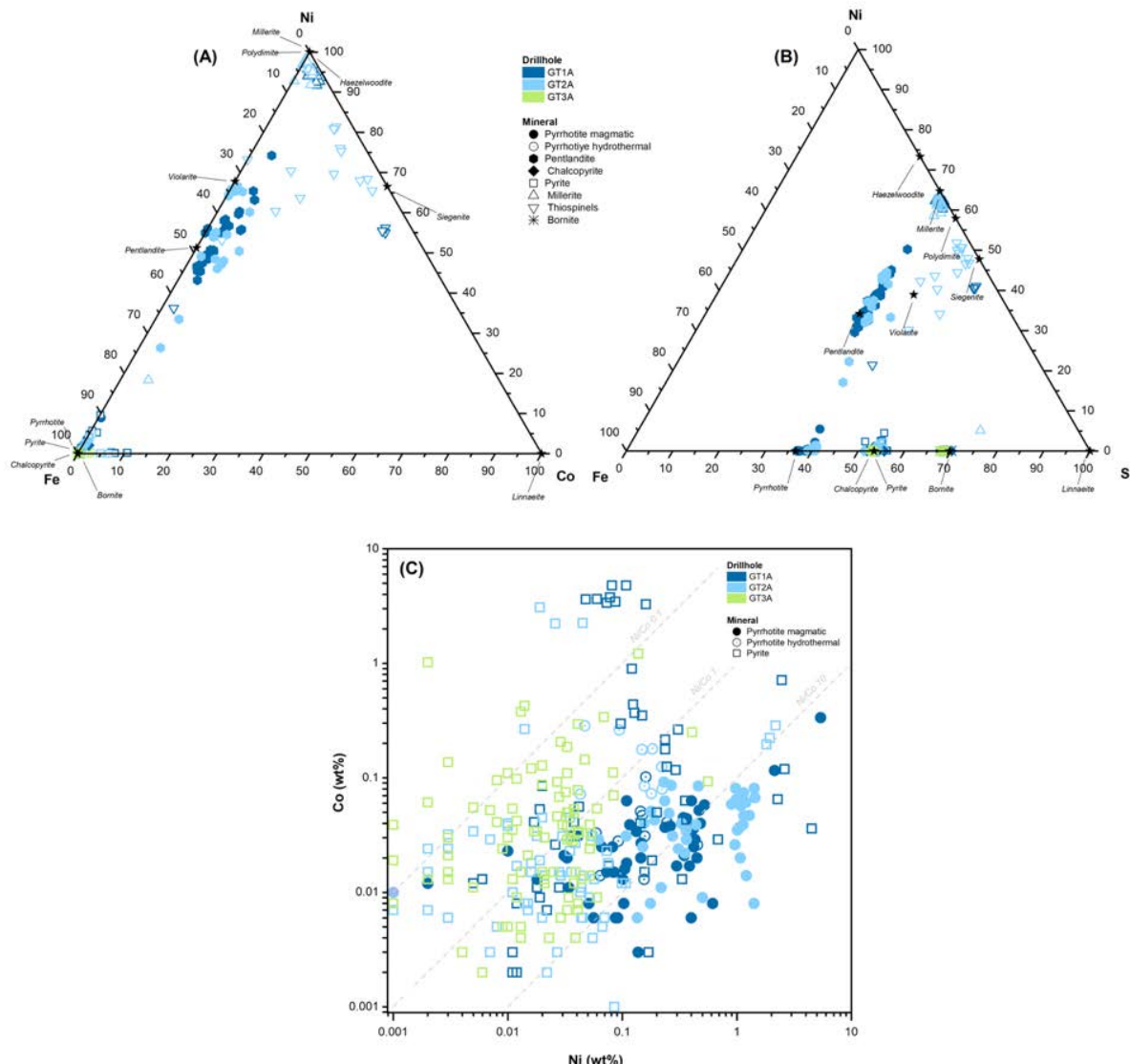
415  
 416 Holes GT1A and GT2A have low sulfide abundances (<< 1 %vol) compared to Hole GT3A cores but  
 417 wider phase and textural variance (Figure 5B-D). Magmatic sulfides (as described above) are  
 418 predominantly preserved in the least altered and deformed intervals (

419 **Figure 5B-D).** The foliated gabbros in Hole GT2A have less well preserved pentlandite and more  
 420 abundant chalcopyrite compared to Hole GT1A, although it is unclear whether this results from  
 421 remobilization or is a primary feature. In both Holes, sulfides are completely remobilized in intervals  
 422 with intense cataclastic deformation and hydrothermal overprint including zones with abundant  
 423 deformation-related veins and fault gouges. Fault zones are abundant in both Holes GT1A and GT2A  
 424 but more common in the former where several meter-scale intervals of damaged rock are present (

425 **Figure 5B**). Consequently, sulfides are chiefly absent throughout large intervals of Hole GT1A, including  
426 those corresponding to the projected intersection of the ZMFZ (~150-100 m). Moderately altered rocks  
427 display variable degrees of magmatic sulfide remobilization and deposition of hydrothermal  
428 assemblages. In Hole GT1A the most common metasomatic replacement is the formation of pyrite-  
429 millerite±chalcopyrite, whereas pyrite+(siegenite-polydimitite)<sub>ss</sub>±chalcopyrite aggregates are more  
430 common in Hole GT2A (**Figure 4D, F**;

431 **Figure 5A-B**). Pyrite can also form idiomorphic or blocky aggregates overgrowing the silicate assemblage  
432 that are more abundant as pyrrhotite disappears from the assemblage (**Figure 4G**). Minute aggregates  
433 of sphalerite are most common in Hole GT2A, mostly associated with hydrothermal chalcopyrite  
434 although some partially fill clinzoisite-albite-chalcopyrite veins (**Figure 4H**). Sulfides also show some  
435 compositional differences between both Holes. Pyrite tends to be consistently more enriched in both Ni  
436 and Co in Hole GT1A relative to Hole GT2A (**Figure 6C**) whereas magmatic pyrrhotite tends to show  
437 minor (<1 wt%) enrichment in Ni leading to Ni/Co ratios >1 (**Figure 6C**). Pyrrhotite platelets in smectite-  
438 chlorite pseudomorphs after olivine (**Figure 4A-B**) show similar metal contents relative to its magmatic  
439 counterparts, although some pyrrhotite grains in Hole GT2A display a low Ni/Co trend similar to pyrite  
440 (**Figure 6C**).

441



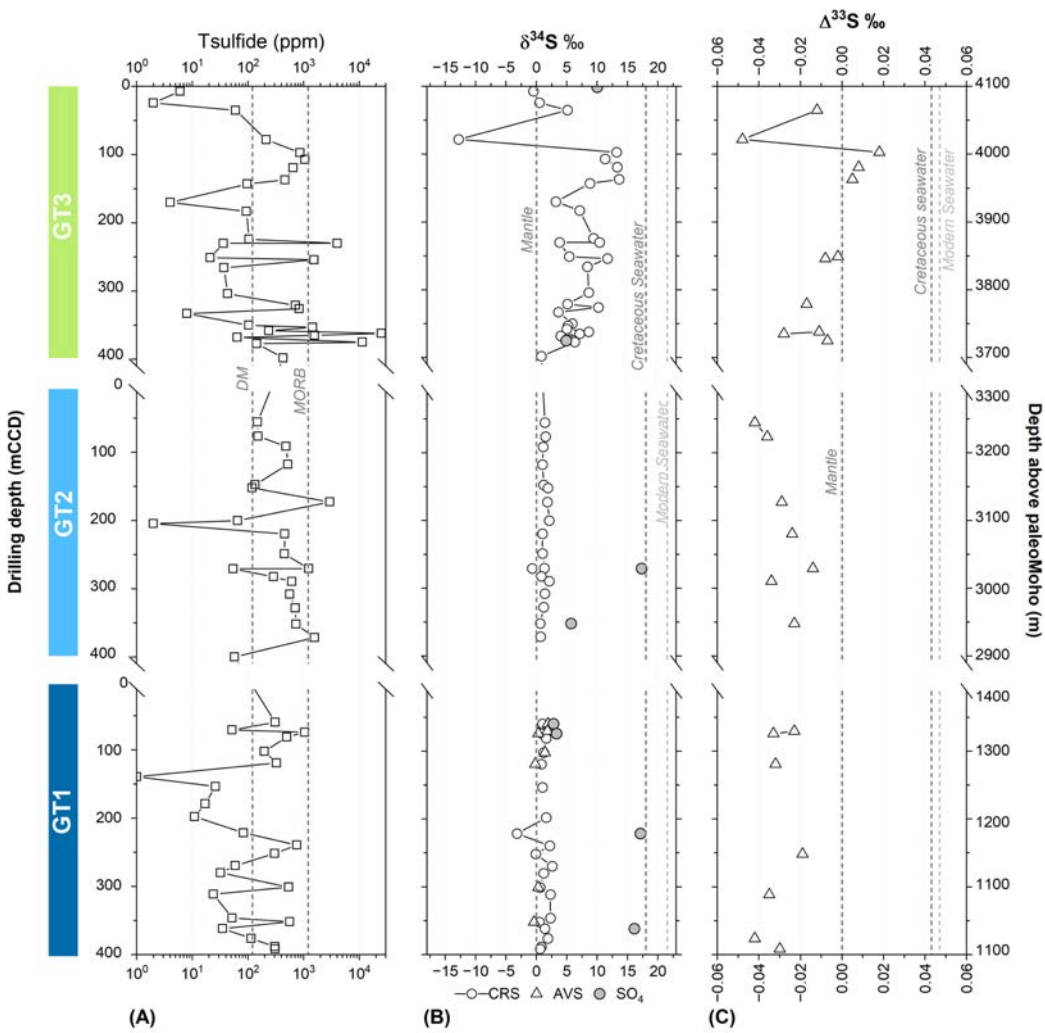
442

443 **Figure 6.** Sulfide compositional variations. (A, B) Fe-Ni-Co and Fe-Ni-S showing endmember compositions (stars) and using  
444 wt%. The diagrams show the deviation from ideal compositions in pentlandite towards higher Ni/Fe towards millerite in both GT1A  
445 and GT2A and the formation of violarite-siegenite-polydymite solid solutions in Hole GT2A. Also, it shows GT3A pyrite-  
446 chalcopyrite-bornite hydrothermal assemblages are close to ideal compositions. (C) Ni-Co variations for Fe-sulfide phases. EPMA  
447 data are available in SM 2 Table 2.

448

#### 449 **4.2 Bulk rock sulfur contents and isotope compositions**

450 Results for extracted sulfide sulfur and sulfate contents are persented in **Table 1** and plotted in a  
451 composite downhole profile in **Figure 7**. **Figure 8** shows the statistical distribution for the total sulfide sulfur  
452 concentrations and isotope compositions.

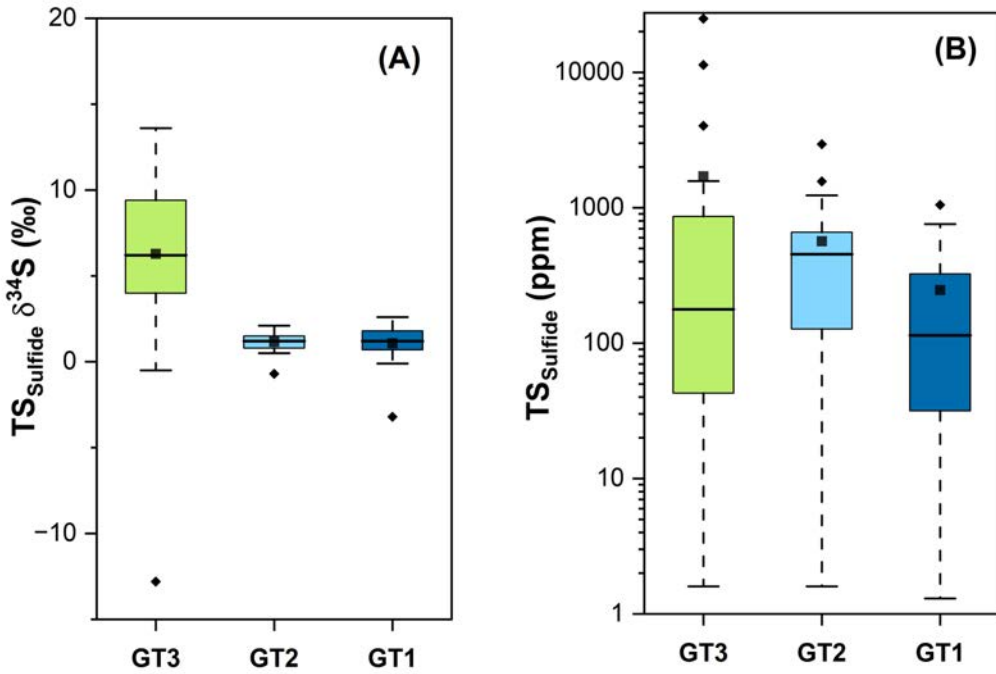


453

454 **Figure 7.** Downhole variation of whole-rock measurements for a reconstituted stratigraphic section of the three drillholes sulfide  
 455 sulfur: (A) Total sulfide sulfur ( $TS_{\text{Sulfide}}$ ); (B)  $\delta^{34}\text{S}$  for sulfide and sulfate fractions; (C)  $\Delta^{33}\text{S}$  in CRS extracts. Also shown for  
 456 reference: (A) sulfur contents for EPR lavas (Alt et al., 2010) and depleted mantle (DM- Salters and Stracke, 2004); (B)  $\delta^{34}\text{S}$  for  
 457 MORB (Sakai et al., 1984), Cretaceous (Kampschulte and Strauss, 2004) and modern seawater (Johnston et al., 2014); (C)  $\Delta^{33}\text{S}$   
 458 for mantle (Labidi et al., 2012; Ono et al., 2007), modern and Cretaceous seawater (Masterson et al., 2016).

459

460 Sulfur contents ( $TS_{\text{Sulfide}}$ ) in Hole GT3A show a broad variation with several domains showing very high  
 461 sulfide concentrations up to 24902 ppm for a pyrite-epidote patch, but relatively low median  
 462 concentrations due to very low S concentrations in many studied core intervals (Hole GT3A:  
 463  $X=\text{median}=178$  ppm,  $\sigma=\text{standard deviation}=4873$  ppm). Sulfur contents ( $TS_{\text{Sulfide}}$ ) in the mid- to lower  
 464 crustal section are higher in Hole GT2A ( $X = 454$  ppm,  $\sigma = 693$  ppm, max = 2951 ppm) relative to the  
 465 layered gabbros in Hole GT1A ( $X = 114$  ppm,  $\sigma = 277$  ppm, max = 1050 ppm).



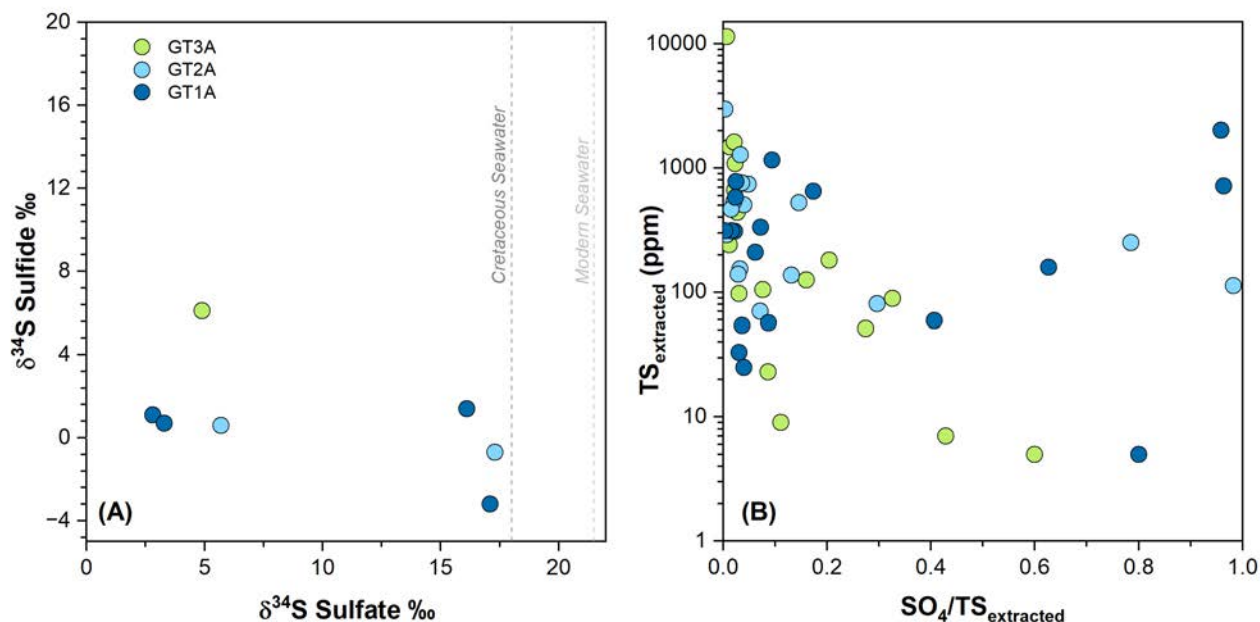
466  
467

468 **Figure 8.** Statistical distribution of  $\delta^{34}\text{S}_{\text{TS}}$  (A) and sulfide-sulfur concentration (i.e.  $\text{TS}_{\text{Sulfide}} = \text{AVS} + \text{CRS}$ ) (B) for the three Holes.  
469 Upper and lower dashed bars: 95<sup>th</sup> and 5<sup>th</sup> percentiles, boxes: 75<sup>th</sup> and 25<sup>th</sup> percentiles; thick horizontal bar: median; white  
470 squares: mean; diamonds: outliers.

471

472 Samples from Hole GT3A only yielded CRS with a wide range in  $\delta^{34}\text{S}$  from -12.8‰ to +13.6 ‰. Isotope  
473 variations are not lithology-dependent but show distinct variations with depth: samples down to ~80 m  
474 vary from -12.8‰ to +5.1‰ and generally have very low  $\text{TS}_{\text{Sulfide}}$  contents. From 80 m  $\delta^{34}\text{S}$  reaches its  
475 highest value ( $\delta^{34}\text{S} = +13.6\text{‰}$ ), and then broadly decreases downhole albeit not uniformly and is  
476 associated with widely variable  $\text{TS}_{\text{Sulfide}}$  concentrations (Figure 7). Pyrrhotite is scarce in Hole GT2A and  
477 only traces of AVS were recovered, insufficient for isotope measurements. In Hole GT1A, the AVS  
478 fraction ( $\delta^{34}\text{S}_{\text{AVS}} = -0.4\text{‰}$  to  $+1.9\text{‰}$ ) lies within ~1‰ relative to the isotope composition of the  
479 coexisting CRS fraction ( $\delta^{34}\text{S}_{\text{CRS}} = -3.2\text{‰}$  to  $+2.6\text{‰}$ ). The median  $\delta^{34}\text{S}$  for CRS fraction in both mid-  
480 to lower crustal holes is identical ( $X = +1.2\text{‰}$ ) with Hole GT1A samples spanning a slightly wider range  
481 of compositions ( $\delta^{34}\text{S} = -3.2\text{‰}$  to  $+2.6\text{‰}$ ) relative to Hole GT2A ( $\delta^{34}\text{S} = -0.7\text{‰}$  to  $+2.1\text{‰}$ ).

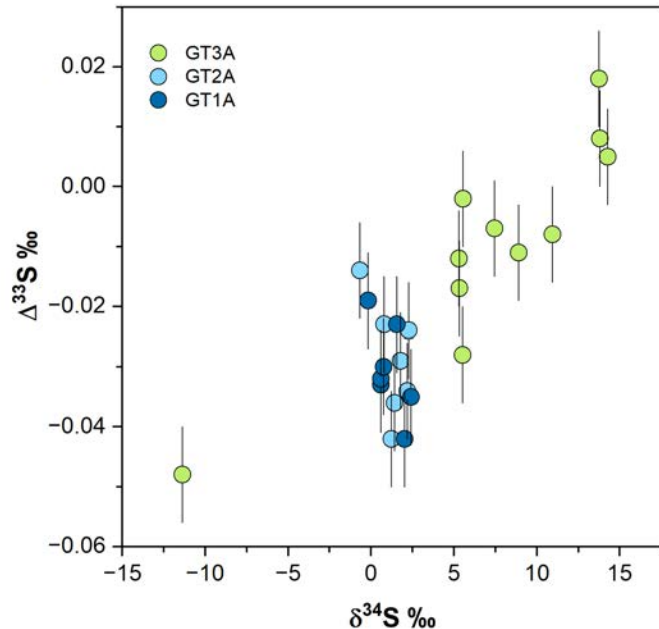
482 The relationships between sulfate and sulfide are shown in Figure 9. Sulfate minerals are scarce  
483 throughout the Wadi Gideah drill holes with similar median concentration values for the entire studied  
484 crustal section ( $X \sim 12\text{-}15\text{ ppm}$ ) and sulfate is generally only a small fraction of the extracted total sulfur,  
485 with  $\text{TS}_{\text{SO}_4}/\text{TS}_{\text{ext}}$  mostly  $<0.2$  (Figure 9B). Maximum sulfate concentrations increase from Hole GT3A (76  
486 ppm), to Hole GT2A (197 ppm) to 1933 ppm in fault zone samples from Hole GT1A that also include  
487 traces of pyrite. The  $\delta^{34}\text{S}$  isotope composition for sulfates is generally close to the range of coexisting  
488 sulfides, except for three GT1A and GT2A samples with higher sulfate fractions ( $\text{TS}_{\text{SO}_4}/\text{TS}_{\text{ext}}$  0.40 to  
489 0.96). Here, sulfate with a  $\delta^{34}\text{S}$  value up to +17.3‰, is considerably higher than the coexisting sulfides.



492 **Figure 9.** (A) Relationships between sulfide and sulfate isotope compositions. (B) Total extracted sulfur (TS<sub>extracted</sub>) versus sulfate  
 493 fraction (TS<sub>SO<sub>4</sub></sub>). Also shown for reference:  $\delta^{34}\text{S}$  for Cretaceous (Kampschulte and Strauss, 2004) and modern seawater (Johnston  
 494 et al., 2014).

#### 496 4.2.1 Multiple sulfur isotope compositions

497 Multiple sulfur isotope measurements performed on CRS extracts for selected samples are listed in  
 498 **Table 2** and shown in **Figure 7C**; **Figure 10** shows respective  $\Delta^{33}\text{S}$  and  $\delta^{34}\text{S}$  values. Mid-lower crustal  
 499 rocks show uniformly negative  $\Delta^{33}\text{S}$  compositions (Hole GT1A = -0.042‰ to -0.019‰; GT2A = -0.042‰  
 500 to -0.014‰), that display a near vertical trend with  $\delta^{34}\text{S}$ . Hole GT3A has one sample with a very negative  
 501  $\Delta^{33}\text{S}$  value of -0.048‰ and a  $\delta^{34}\text{S}$  value of -12.8‰, but other Hole GT3A samples have  $\Delta^{33}\text{S}$  between  
 502 -0.028‰ to +0.018‰ and display a steep positive trend with  $\delta^{34}\text{S}$  (**Figure 10**).



504

505

**Figure 10.** Relationship between  $\Delta^{33}\text{S}$  and  $\delta^{34}\text{S}$  obtained from CRS fractions.

506

#### 507 4.3 In-situ isotope compositions

508 In-situ SIMS data are listed in **Table 3**, with point locations for representative mineral assemblages  
 509 shown in **Figure 4**. In-situ measurements in the dike-gabbro transition zone samples (Hole GT3A) aimed  
 510 to assess the existence of compositional zonings in large hydrothermal sulfide grains and fractionations  
 511 between different sulfide phases. The large blebs in basalt samples in the Upper Dike Sequence display  
 512 lighter sulfur isotope values in their cores relative to their grain borders, ranging from  $+11.9\text{\textperthousand}$  to  
 513  $+14.4\text{\textperthousand}$  in the largest grains (**Figure 3A1**). In contrast, the epidote-pyrite patch with spongy texture within  
 514 the Lower Gabbro Sequence (**Figure 3D**) shows mostly uniform  $\delta^{34}\text{S}$  values ( $+9.3\text{\textperthousand}$  to  $+10.0\text{\textperthousand}$ ) with a  
 515 single value of  $+7.3\text{\textperthousand}$  in one grain boundary. In the Lower Gabbro Sequence, chalcopyrite is more  
 516 abundant, and has a heavier isotope composition relative to associated pyrite: one basalt (232 m-CCD)  
 517 includes pyrite with  $\delta^{34}\text{S}$  between  $-1.0\text{\textperthousand}$  and  $+1.2\text{\textperthousand}$  whereas chalcopyrite displays  $\delta^{34}\text{S}$  values from  
 518  $+1.8\text{\textperthousand}$  to  $2.5\text{\textperthousand}$ . This chalcopyrite is partly altered to bornite that was not analyzed due to the lack of  
 519 appropriate standards. Sulfides in one diorite sample show heterogenous compositions, with  
 520 significantly higher chalcopyrite  $\delta^{34}\text{S}$  values ( $+2.4\text{\textperthousand}$  to  $+13.1\text{\textperthousand}$ ) compared to pyrite ( $+1.3\text{\textperthousand}$  to  $5.4\text{\textperthousand}$ ;  
 521 **Figure 3C**). There are no significant differences between cataclastic pyrite and non-cataclastic spongy  
 522 pyrite in the same samples.

523 In the mid-lower crust (Holes GT1A and 2A), SIMS analyses focused on distinguishing the composition  
 524 of mineral species occurring in different paragenetic contexts (see Section 4.2). Median  $\delta^{34}\text{S}$  values for  
 525 hydrothermal pyrite ( $X=+1.6\text{\textperthousand}$ ;  $-1.2\text{\textperthousand}$  to  $+2.7\text{\textperthousand}$ ) are slightly more positive than for metasomatic pyrite  
 526 ( $X=-0.8\text{\textperthousand}$ ;  $-3.2\text{\textperthousand}$  to  $0.4\text{\textperthousand}$ ). Magmatic pyrrhotite grains have a slightly negative isotope composition  
 527 ( $X=-0.5\text{\textperthousand}$ ;  $-4.3\text{\textperthousand}$  to  $+0.1\text{\textperthousand}$ ), a tendency more pronounced in grains that experienced remobilization  
 528 ( $X=-2.8\text{\textperthousand}$ ;  $-3.8\text{\textperthousand}$  to  $-1.8\text{\textperthousand}$ ) and hydrothermal pyrrhotite in smectite-chlorite aggregates ( $X=-3.8\text{\textperthousand}$ ; -

529 5‰ to +0.8‰). Magmatic, remobilized and hydrothermal chalcopyrite overlap in composition with  
530 median values of +0.9‰, +0.5‰ and +0.7‰ respectively, with a wider spread of values for the  
531 hydrothermal chalcopyrite (-1.8‰ to +2.5‰). Grains representing metasomatic replacement have a  
532 slightly heavier isotopic compositions ( $\Delta=+1.4\text{‰}$ ) although only 3 spots were analyzed showing a  
533 relatively narrow compositional range.

534 As can be seen from **Table 3**, results from in-situ analyses fall within the range of whole-rock  
535 measurements in the same sample or in adjoining domains. There are two noticeable exceptions.  
536 Sample GT3A-140Z-2 22-30 cm is a basalt from the Hole GT3A Lower Gabbro Sequence for which in-  
537 situ measurements yielded relatively lighter compositions (-1 to +2.5‰) compared to the whole rock  
538 (+5‰). This sample has bornite after chalcopyrite which may have contributed to the heavier  
539 composition measured in whole rock. The second disparity occurs in lower crust sample GT1A-152Z-3  
540 0.8 cm where SIMS measurements in pyrrhotite blebs yield negative isotope values (-4.3‰ to -2.2‰)  
541 lower than the measured whole-rock value (0.6‰). This sample is essentially fresh and devoid of  
542 hydrothermal sulfides therefore the only explanation we can provide is that pyrrhotites are anomalous  
543 and/or pentlandite contributed to this sample positive whole-rock isotope signature.

544 **5 DISCUSSION**

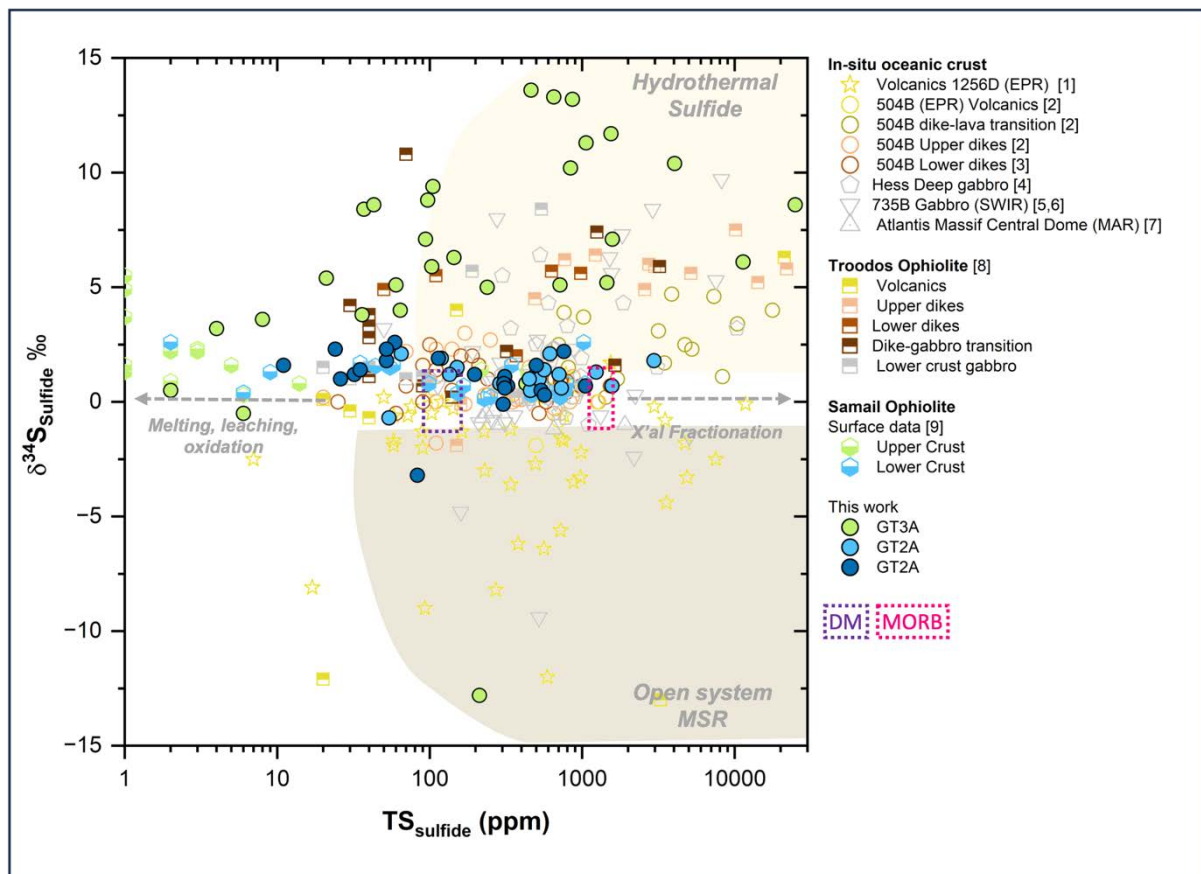
545 **5.1 Sulfur geochemistry in the oceanic crust**

546 We firstly evaluate the  $\delta^{34}\text{S}$  values with respect to sulfur contents in our samples and compare them to  
547 well-studied sections of ophiolitic and in-situ oceanic crust (**Figure 11**). A first insight into the processes  
548 that affected the studied crustal section shows the compositional fields for sulfides formed through  
549 different pathways during seawater/rock interaction following Alt et al. (2007). The crustal section is  
550 highly heterogenous and includes gabbroic cumulates from the mid-lower crust (Holes GT1A and  
551 GT2A) and dikes and varitextured gabbros (Hole GT3A) from the dike-gabbro transition which  
552 lithological nature must be considered to determine reference values for primary (magmatic) S  
553 concentrations, as discussed below.

554

555

556



557

558

559 **Figure 11.** Sulfur geochemistry showing sulfide sulfur ( $TS_{\text{Sulfide}}$ ) versus  $\delta^{34}\text{S}_{\text{Sulfide}}$ . Arrows indicate processes that can lead to  
560 sulfur loss via melting, leaching or oxidation and sulfur increase via crystal fractionation without changes in the isotopic  
561 composition and the fields indicate expectable isotope compositions for sulfides formed via open system Microbial Sulfate  
562 Reduction (MSR) or Hydrothermal Sulfide Addition via Thermochemical Sulfate Reduction (TSR), based on Alt et al., 2007.  
563 Ocean crust data from: [1]- Alt and Shanks, 2011; [2]- Alt et al., 1989, [3]- Alt et al., 1995, [4]- Puchelt et al., 1996, [5] Alt and  
564 Anderson, 1991, [6] Alford et al., 2011, [7] Delacour et al., 2008a, [8] Alt, 1994, [9] Oeser et al., (2012). Also shown for reference:  
565 MORB  $\delta^{34}\text{S}$  Sakai et al. (1984), sulfur contents for EPR glasses Alt et al.(2010), depleted mantle (DM) Salters and Stracke  
566 (2004).

567

### 568 5.1.1 Main processes at the dike gabbro transition: Hole GT3A

569 Sulfide contents in Hole GT3A samples are extremely low considering the non-cumulate, and relatively  
570 evolved nature of these rocks ( $\#Mg = Mg/Mg+Fe$ , molar:  $X=0.52; 0.32-0.75$ ). Sulfur solubility in basaltic  
571 melts increases with Fe content, and variably complex formulation has been proposed to predict sulfur  
572 contents in the melt or sulfur capacity at sulfide saturation-SCSS (Li and Ripley, 2009; Liu et al., 2007;  
573 Mathez, 1976). In the absence of S measurements for fresh lavas or glasses from Oman, we rely on  
574  $\#Mg$ -S relationships (**Eq. 3**) for ODP Hole 1256D fresh glasses (Alt and Shanks, 2011) with similar  
575 compositional range ( $\#Mg X=0.62; 0.32-0.63$ ), to estimate primary sulfur contents for Hole GT3A  
576 samples.

577 **Eq. 3**

$$S = -0.198Mg\# + 0.234$$

578 Magmatic sulfur contents for Hole GT3A rocks are estimated to lie between 851 and 1439 ppm,  
579 which is significantly higher than their  $Ts_{Sulfide}$  or  $Ts_{Ext}$  sulfur contents (Figure 9, Figure 11; Supplementary  
580 Material SM3- Table 1), implying that pervasive sulfur losses occurred throughout the section. Sulfide  
581 addition (>2000 ppm) is concentrated in the Upper Gabbro sequence (~230-250 m) and at the bottom  
582 (~360-375 m) of the Lower Gabbro Sequence.

583 The reduction of seawater sulfate to sulfide via biogenic (Microbial Sulfate Reduction- MSR), or  
584 abiogenic high temperature thermochemical sulfate reduction (TSR) pathways will lead to sulfide  
585 addition with extensive isotope fractionations. Because of the biological preference for  $^{32}S$ , open system  
586 MSR will have large fractionation factors that will lead to very negative isotopic signatures (Canfield,  
587 2004). Only one sample in the Upper Dike Sequence of Hole GT3A has a negative isotope signature -  
588 12.8 ‰ which would be consistent with a biogenic origin via MSR. Likewise, one lava sample from  
589 Wadi Gideah was reported by Oeser et al. (2012) with a strongly negative  $\delta^{34}S$  value of -31.2 ‰. For  
590 both samples, sulfur contents are low (~210 ppm) suggesting that these rocks experienced leaching of  
591 magmatic sulfur prior to the addition of a small amount of biogenic sulfur. All other upper crust samples  
592 in this study show increasingly heavy sulfur isotope signatures at increasing sulfur contents consistent  
593 with abiogenic TSR reactions during intense hydrothermal alteration. TSR is most effective above 250  
594 °C, requiring  $H^+$  provided by the simultaneous oxidation of ferromagnesian magmatic minerals in the  
595 rock and will lead to moderately heavy  $\delta^{34}S$  values (Shanks et al., 1981; Figure 11). Sulfur isotope  
596 values determined here for the dike-gabbro transition (Hole GT3A) section differ substantially from  
597 those reported by Oeser et al. (2012). They obtained  $\delta^{34}S_{CRS}$  for sulfide between +0.3 to +5.4 ‰ that  
598 coexist with heavy sulfates (+2.8 to +14.8 ‰), which fall within the range of our sulfide isotopic  
599 compositions (-0.5 to +13.6 ‰; Figure 11). Given the coincidence between sulfate isotopic values  
600 collected in outcrop (Oeser et al., 2012) and sulfide obtained in core samples (this work), we suggest  
601 that the surface pyrite sulfur (CRS) may have experienced subaerial oxidation, as is commonly  
602 observed in VMS deposits of Oman, where pyrite oxidizes almost immediately after exposure (Cravinho  
603 et al., 2023). Oxidation via both abiotic or microbial pathways has been recognized to produce  
604 fractionations up to -18 ‰ (Alt et al., 2007; Canfield, 2001; Delacour et al., 2008a; Delacour et al.,  
605 2008b). However, it is common that abiotic oxidation results in negligible fractionation thus explaining  
606 the overlapping sulfide (this work) and sulfate (Oeser et al. 2012) isotope signatures. Hole GT3A rocks  
607 have a remarkably heavy isotopic composition compared to in-situ oceanic crust, consistent with the  
608 sheeted dike complex in Cretaceous Troodos ophiolite (Alt, 1994), albeit that the Samail sheeted dikes  
609 are even heavier. This is particularly significant considering that Cretaceous seawater was isotopically  
610 lighter (Kampschulte and Strauss, 2004; see below) than modern day seawater. Consequently,  
611 scenarios of restricted closed system seawater circulation that can produce significantly heavier isotope  
612 signatures will also be considered in the geochemical modelling section (5.2) below.

613

614 **5.1.2 Main processes in the mid to lower crust: Holes GT2A and GT1A**

615 Most of the Samail ophiolite mid to lower crustal gabbros from Holes GT1A and GT2A are cumulate  
616 rocks and therefore expectedly have lower S concentrations than evolved MORBs from the EPR (1250  
617  $\pm 200$  ppm, Alt & Shanks, 2011). A significant number of samples have sulfide concentrations lower  
618 than depleted mantle values ( $120 \pm 30$  ppm, Salters & Stracke, 2003) (Figure 11). Results from this study  
619 reveal that rocks with the lowest S concentrations are from fault damage zones where there was near  
620 complete leaching of magmatic sulfides without the deposition of secondary sulfides. Leaching, melting  
621 and equilibrium oxidation of magmatic sulfides will decrease total sulfide contents without imparting  
622 changes in isotopic values (Alt et al., 2007). All other mid-lower crustal gabbros with ( $T_{S_{\text{Sulfide}}}$  values  
623 between 120 and 1200 ppm) have sulfide sulfur concentrations within the range of in-situ gabbroic  
624 oceanic crust and Troodos lower gabbros. The least altered rocks (defined here as rocks less affected  
625 by post-magmatic processes with <50% hydrothermal sulfide) have  $T_{S_{\text{Sulfide}}}$  values that vary by one  
626 order of magnitude (114 and 1050 ppm) suggesting a wide range of primary sulfur concentrations in  
627 the cumulates due to segregation and mobility of sulfide melts within the cumulate mush.

628 Regardless of the intensity of hydrothermal and tectonic-induced alteration, both Holes from the Samail  
629 mid- to lower crustal section (Hole GT2A and GT1A) broadly preserve magmatic isotope signatures  
630 (Sakai et al., 1984). This is consistent with results obtained by SIMS showing that the entire spectrum  
631 of analyzed sulfides, from secondary (hydrothermal or metasomatic) to partly remobilized sulfides,  
632 chiefly retained their magmatic signatures. The sole exception are pyrrhotite laths within late-formed  
633 smectite aggregates replacing olivine, which have mildly negative sulfur isotope signatures, with  $\delta^{34}\text{S}$   
634 values as low as  $-5.0\text{\textperthousand}$ . Otherwise, the Samail lower crust is similar to most gabbroic sections of  
635 oceanic crust (Figure 11) where a few  $^{34}\text{S}$ -enriched samples in the uplifted crust of SWIR (ODP Hole  
636 735B; Alford et al., 2011) have been attributed to closed system microbial sulfate reduction (MSR) that  
637 can lead to heavy signatures due to reservoir effects.

638

639 **5.2 Geochemical modeling of sulfur geochemistry processes**

640 Only one sample from Hole GT3A can be reasonably attributed to biogenic mediated processes.  
641 Consequently, in this section we focus on high-temperature abiogenic processes dominating sulfur  
642 cycling during hydrothermal alteration of the Samail ophiolite crust. Due to their greater sensitivity in  
643 assessing mass-dependent sulfur isotope fractionation, modelling will concentrate on the multiple sulfur  
644 isotope dataset, using mixing model formulations for thermochemical sulfate reduction (TSR) that take  
645 into account temperature (Section 5.2.2) and variable sulfur concentrations (Section 5.2.3) in the  
646 system.

647 **5.2.1 Input isotope values for TSR mixing models**

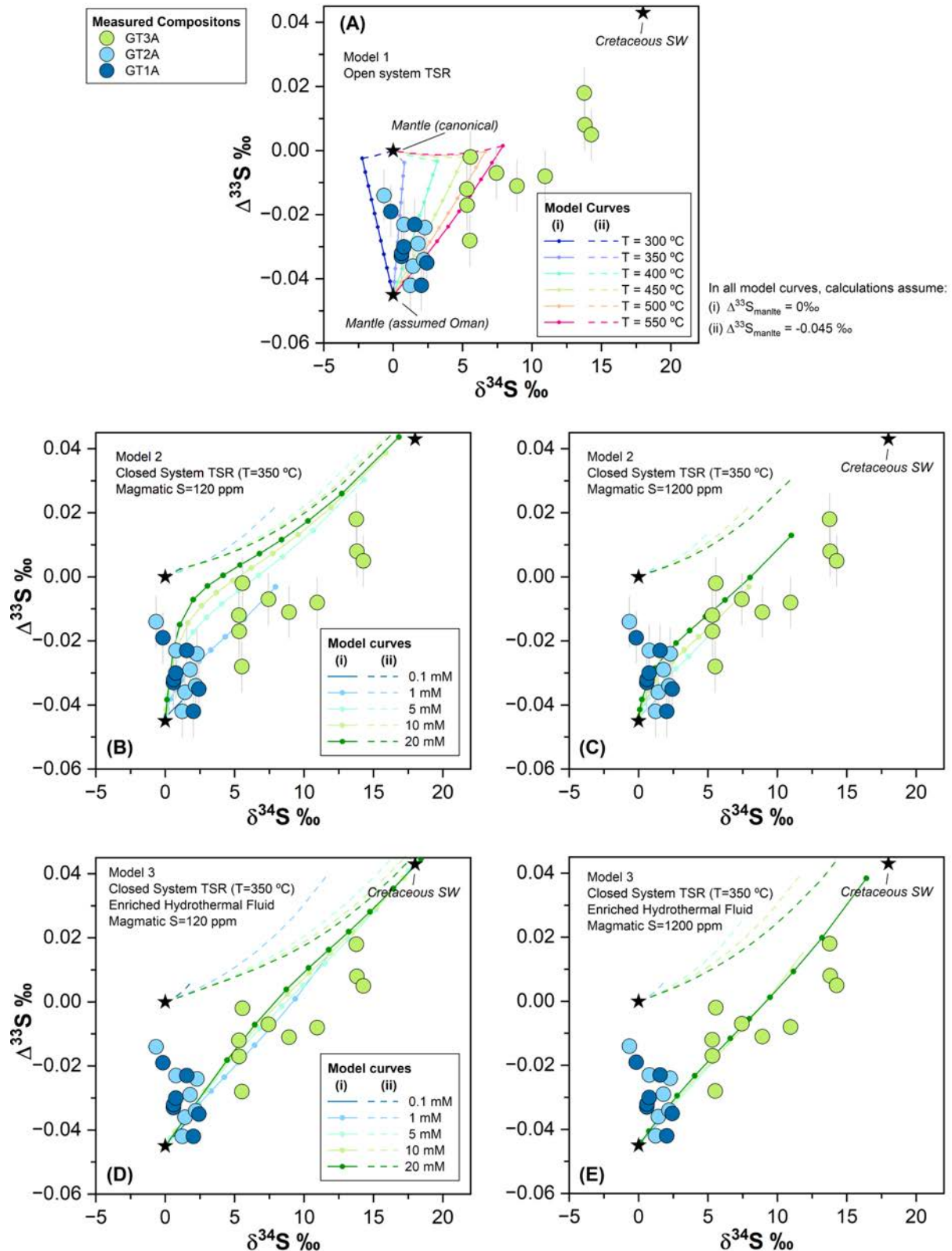
648 The main pools of sulfur involved in both low temperature and hydrothermal processes affecting the  
649 oceanic crust are magmatic sulfide and seawater sulfate. Recent measurements of quadruple sulfur  
650 isotopes on MORB samples suggest an average composition for the Depleted Mantle reservoir of  $\delta^{34}\text{S}$   
651  $-1.28 \pm 0.33\text{\textperthousand}$  (Labidi et al., 2014) instead of the canonical value of  $0.3 \pm 0.5\text{\textperthousand}$  of Sakai et al. (1984).

652 Our whole rock measurements in mid-lower crustal samples with more than 70% magmatic sulfides  
653 show values between  $-0.1\text{\textperthousand}$  and  $+1.9\text{\textperthousand}$  with median close to  $+1\text{\textperthousand}$ . Although in-situ SIMS  
654 measurements show some anomalous pyrrhotite isotopic compositions (sample GT1A-152Z-3 0-8 cm),  
655 the positive sulfur isotope signatures in magmatic chalcopyrite and whole-rock data for fresh samples  
656 strongly suggest that the integrated monosulfide from which pyrrhotite-chalcopyrite-pentlandite were  
657 exsolved had a slightly positive signature. This would lie within the  $+0.3 \pm 0.5\text{\textperthousand}$  range suggested by  
658 Sakai et al. (1984) and therefore we use the value of  $0\text{\textperthousand}$  as a reference in our calculations.

659 Mantle isotope compositions for  $\Delta^{33}\text{S}$  are  $0\text{\textperthousand}$  (Labidi et al., 2012; Ono et al., 2007). However, data  
660 from incipiently hydrothermally altered mid-lower crustal sections from this work and Oeser et al. (2012)  
661 are consistently negative. Indeed, irrespective of the model considered below, any set of curves  
662 calculated assuming mantle compositions of  $\Delta^{33}\text{S}=0\text{\textperthousand}$  (Labidi et al., 2012; Ono et al., 2007) falls out  
663 of the compositional space of the samples studied (stippled curves in Figure 12). Considering that Samail  
664 mid-lower crustal rocks preserving magmatic sulfides have isotope compositions as low as  $\Delta^{33}\text{S}=-$   
665  $0.042\text{\textperthousand}$ , we have used a value of  $-0.045\text{\textperthousand}$  for the mantle composition in the models below (solid lines  
666 in Figure 12), although the model curves for the canonical mantle value are also depicted (stippled lines)  
667 for comparison. The potential causes for the deviation of  $\Delta^{33}\text{S}$  values relative to canonical values require  
668 further investigation. We propose a provisional explanation that relates to the Indian MORB  
669 geochemical features of the Samail mantle source (Godard et al., 2006, Jesus et al., 2023). Indian  
670 MORB presumably taps slab-derived components from old subduction zones where sediments with  
671 mass independent fractionation (MIF) signatures could provide the mild but systematically negative  
672  $\Delta^{33}\text{S}$  signatures to the Samail crust. Recycling of old sedimentary slab-derived components has been  
673 documented for example in the Mangaia plume considered to be an end-member for high- $\mu$  mantle  
674 where Archean sediments were recycled (Cabral et al., 2013).

675 Mesozoic seawater sulfate isotope composition was lower than modern day ( $\delta^{34}\text{S}=21.5 \pm 0.5\text{\textperthousand}$ ;  
676 Johnston et al., 2014), between  $+16$  to  $+22\text{\textperthousand}$  (Kampschulte and Strauss, 2004). During the Cretaceous,  
677 compositions were closer to  $+18\text{\textperthousand}$  (Kampschulte and Strauss, 2004; Paytan et al., 2004) and we use  
678 this value in our modeling together with  $\Delta^{33}\text{S}$  of  $0.043 \pm 0.016\text{\textperthousand}$  following Masterson et al. (2016).

679 In all mixing models presented below (Figure 12), the plotted  $\delta^{34}\text{S}$ - $\Delta^{33}\text{S}$  curves represent the pooled  
680 (accumulated) product composition of  $\text{H}_2\text{S}$  for a given fraction of the mixture ( $f$ ). Fractionation factors  
681 between sulfide and  $\text{H}_2\text{S}$  increase with decreasing temperature, being highest for pyrite at  $300\text{ }^{\circ}\text{C}$  ( $\Delta_{\text{Py}-$   
682  $\text{H}_2\text{S}} = 1.22\text{\textperthousand}$ ) Ohmoto et al., 1979. These values are one order of magnitude smaller than the isotope  
683 fractionations for seawater sulfate reduction to  $\text{H}_2\text{S}$  (10.1 to  $20.2\text{\textperthousand}$ ; see 5.2.2.) at the temperatures  
684 considered in modeling (550-300  $^{\circ}\text{C}$ ). Therefore, we take the composition of  $\text{H}_2\text{S}$  in the models to be  
685 chiefly identical to the resulting hydrothermal sulfides since this will have a negligible bearing on the  
686 model sulfide compositions.



687

688 **Figure 12.** Modelling of sulfide compositions using different mixing models for TSR. In all plots, curves represent the pooled (or  
689 accumulated) composition of  $\text{H}_2\text{S}$ : the upper set of stippled curves (ii) were calculated using the canonical mantle composition  $\Delta$   
690  $^{33}\text{S} = 0.00\text{‰}$  that cannot explain the OmanDP samples. Therefore the solid curves (i) were calculated using  $\Delta^{33}\text{S} = -0.045\text{‰}$ , as  
691 discussed in the text. Nodes in model curves represent increments of mixing from  $f = 0.001$  to  $f=1$ . Additional input parameters  
692 common to all models: magmatic sulfur  $\delta^{34}\text{S}=0\text{‰}$  (Sakai et al., 1984), Cretaceous seawater  $\delta^{34}\text{S}=18\text{‰}$  (Kampschulte and

Strauss, 2004; Paytan et al. 2004)  $\Delta^{33}\text{S} = 0.043 \text{ ‰}$  (Masterson et al., 2016). **(A)** Model 1: Open system mixing for TSR at variable temperature [300-550] °C; **(B-C)** Model 2: Closed system, Rayleigh distillation for TSR assuming magmatic sulfur concentrations of 120 (B) and 1200 ppm (C), calculated for different sulfate concentrations in the hydrothermal fluid, corresponding to the coloured curves; **(D-E)** Model 3: Closed system, Rayleigh distillation for TSR assuming magmatic sulfur concentrations of 120 (D) and 1200 ppm (E), calculated at different sulfate concentrations in the hydrothermal fluid corresponding to the coloured curves. In model 3 it is assumed that the hydrothermal fluid has undergone 40% isotopic enrichment relative to Cretaceous seawater during closed system evolution within the hydrothermal system ( $\delta^{34}\text{S}=26.8 \text{ ‰}$ ,  $\Delta^{33}\text{S}=0.091 \text{ ‰}$ ; see Supplementary Material SM2 Fig.2). Note that for models 1 and 2, assuming a magmatic S concentration of 1200 ppm results in a sulfide product with very little isotopic fractionation, therefore the resulting curves are very short and plot close to the mantle composition being hard to depict.

### 5.2.2 Open system mixing model for TSR as a function of temperature

Within the high-temperature zone at the base of the upper crustal hydrothermal system, the  $\text{H}_2\text{S}$  in the fluid will result from a mixture of (Ono et al., 2007; Shanks, 2001): a) magmatic  $\text{H}_2\text{S}$  leached from the magmatic sulfides in the basaltic (s.l.) rocks (Woodruff and Shanks III, 1988) and; b) thermochemically reduced sulfate in the presence of ferrous-bearing minerals (Shanks et al., 1981). Mixing model 1 in **Figure 12A** shows the effects of open-system thermochemical sulfate reduction (TSR) under a range of temperatures between 300 and 550 °C appropriate for high-temperature seafloor hydrothermal systems (Shanks, 2001). Fractionation factors for  $\text{SO}_4\text{-H}_2\text{S}$  are temperature dependent and were calculated for  $^{34}\alpha$  from Ohmoto and Lasaga (1982), where T is temperature in Kelvin (Eq. 4):

$$\ln^{34}\alpha = \frac{6.463 \times 10^6}{T^2 + 0.56}$$

For mass-dependent  $\text{SO}_4\text{-H}_2\text{S}$   $^{33}\text{S}$  fractionation processes, the temperature dependence of the fractionation factor  $^{33}\alpha$  can be related by the empirical expression for  $^{33}\theta$  (Ono et al., 2007; **Eq. 5**) which at high temperatures approaches the value 0.515 in **Eq. 2**.

$$^{33}\theta = \frac{\ln(^{33}\alpha)}{\ln(^{34}\alpha)} = -\frac{9.460}{T^2} - \frac{0.3117}{T} + 0.5159$$

For each temperature, the sulfide produced from seawater TSR is mixed with the mantle isotope composition following a simple binary mixing model (Eq. 6) where x refers to  $^{33}\text{S}$ ,  $^{34}\text{S}$ .

$$\delta_{\text{Mixture}}^x = f \times \delta_{\text{Seawater}}^x + (1 - f) \times \delta_{\text{Magmatic}}^x$$

Even if only a negligible contribution of leached magmatic sulfide is assumed, in a seawater-derived sulfur dominated system, open-system TSR is only able to produce a relatively narrow compositional range. Fractionation factors increase with decreasing temperature (T=500 to 300 °C,

729  $^{34}\alpha \sim +20$  to  $+10 \text{ ‰}$ ), meaning that TSR will produce S with mildly positive values at 550 °C but slightly  
730 negative  $\delta^{34}\text{S}$  compositions at low temperatures (Figure 12A). The Hole GT3A dike-gabbro transition  
731 zone samples mostly fall outside these model curves, with the high isotopic values implying that either  
732 a modified fluid, with S-isotopic compositions higher than Cretaceous seawater, was involved and/or  
733 there are reservoir effects that the open-system mixing models do not consider.

734 Lower crustal gabbro samples plot within a poorly defined region of the model, albeit following a trend  
735 that approaches the slope of lower temperature model curves. The formation of smectite-chlorite  
736 pyrrhotite aggregates should have occurred at temperatures below 200 °C (Alt et al., 2010). TSR is  
737 sluggish below 250 °C (Shanks et al., 1981) and the large fractionation factors at these temperatures  
738 ( $^{34}\alpha=24.2\text{‰}$ ) could produce sulfide with  $\delta^{34}\text{S}$  values as low as  $-6\text{‰}$ . It is therefore possible that the  
739 formation of secondary pyrrhotite sulfide assemblages began close to the limiting temperatures for TSR  
740 with further alteration to smectite-chlorite stratified formation occurring at lower temperatures (<100 °C,  
741 Alt et al., 2010).

742

#### 743 **5.2.3 Closed-system mixing model for TSR as a function of S concentrations**

744 The amount of sulfur available in the different reservoirs, namely the proportions of S from magmatic  
745 rocks and sulfate in the seawater-modified hydrothermal fluids, provide additional constraints on sulfur  
746 isotope variations. Mixing models 2 and 3 in Figure 12B-D take into account reservoir effects arising from  
747 closed system evolution of the hydrothermal system for different seawater and magmatic sulfur  
748 concentrations, following Rayleigh fractionation formulations adapted by Schwarzenbach et al. (2018).  
749 Based on MgO-S relationships for the dikes and frozen melts of the axial melt lens (Eq. 3), primary  
750 sulfur concentrations in the upper crustal section are estimated between  $\sim 850$  and  $\sim 1450$  ppm. The  
751 application of Eq. 3 to the mid-lower crustal rocks is precluded because these are cumulates and do  
752 not represent melts. Based on median and maximum  $T_{\text{Sulfide}}$  extracts (Table 1 and Figure 8), a wide  
753 permissible range of S concentrations is indicated:  $X= 454$  ppm,  $\text{max}=2951$  ppm for mid-crustal GT2A  
754 cumulates and  $X=114$  ppm,  $\text{max}= 1050$  ppm for GT1A lower crustal cumulates. To accommodate for  
755 this wide range, models consider initial magmatic sulfur concentrations of 120 and 1200 ppm.  
756 Temperature was fixed at 350°C which is representative of the base of an upper crustal hydrothermal  
757 system reaction zone near the dike-gabbro transition (Alt, 1995; Hannington, 2014) and would also  
758 overlap with dominant conditions in the mid-lower crustal section. Similar to S isotope compositions,  
759 seawater sulfate concentrations in the Mesozoic were lower than modern-day seawater, with the best  
760 estimates being 2-12 mM (Timofeeff et al., 2006). However, anhydrite displays retrograde solubility and  
761 upon reaching  $\sim 150$  °C anhydrite should precipitate from seawater-derived fluids that will significantly  
762 deplete the sulfate concentrations of recharge fluids, meaning a much smaller amount of sulfate will  
763 reach the deeper parts of the hydrothermal system (Seyfried Jr and Bischoff, 1981; Sleep, 1991; Teagle  
764 et al., 1998). Accordingly, our models consider a range of sulfate concentrations in the fluid from the  
765 experimental minimum of 0.1 mM (Seyfried Jr and Bischoff, 1981) to 20 mM, which is above the 12 mM  
766 limit proposed for the Cretaceous (Timofeeff et al., 2006).

767 Mixing model 2 (**Figure 12B-C**) shows the sulfide composition that forms from fluids with a starting  
768 isotopic composition equal to Cretaceous seawater at variable sulfate concentrations, represented by  
769 the various colored lines. For high concentrations of magmatic sulfur (1200 ppm), the resulting  
770 hydrothermal sulfide is buffered by the mantle isotopic composition, only reaching  $\delta^{34}\text{S} > 5\text{\textperthousand}$  at high  
771 sulfate concentrations in the fluid (>10 mM). Nevertheless, the heaviest isotopic composition that can  
772 be produced under these model conditions (+11‰) is insufficient to explain many of the heavier  
773 samples from the Hole GT3A dike-gabbro transition zone. For magmatic sulfur concentrations of 120  
774 ppm, the model sulfide compositions are closer to those measured in Hole GT3A if sulfate  
775 concentrations in the fluid are  $\geq 5$  mM, although the corresponding  $\Delta^{33}\text{S}$  values are higher than our  
776 samples.

777 Mixing model 3 (**Figure 12D-E**) introduces the effects of a hydrothermal fluid with isotopic composition  
778 heavier than that of Cretaceous seawater, based on the residual fluid from model 2 (for details see  
779 Supplementary Material SM2, Fig. 2). The best fit was obtained for a fluid that has undergone 40%  
780 isotopic enrichment relative to Cretaceous seawater during closed system evolution within the  
781 hydrothermal system ( $\delta^{34}\text{S} = 26.8\text{\textperthousand}$ ,  $\Delta^{33}\text{S} = 0.091\text{\textperthousand}$ ). This model shows a good fit to measured results,  
782 accounting for the heavier isotope compositions recorded in Hole GT3A, even for an initial magmatic S  
783 concentration of 1200 ppm (closer to the estimates for our samples). Furthermore, there is a good  
784 adjustment for scenarios with low initial sulfate concentrations in the hydrothermal fluid which are likely  
785 more realistic with those reaching the roots of the hydrothermal system (Seyfried Jr and Bischoff, 1981;  
786 Sleep, 1991; Teagle et al., 1998).

787 Models 2 and 3 do not provide additional constraints for sulfide formation in mid-lower crustal rocks. At  
788 lower temperatures all curves would follow a trend towards lower  $\delta^{34}\text{S}$  values at increasing  $\Delta^{33}\text{S}$   
789 values as seen in Model 1 (Supplementary Material SM2, Fig. 2). Given the significantly lower degree  
790 of alteration in most mid-low crustal rocks, it is reasonable that most high temperature alteration  
791 proceeded under low fluid/rock ratios and closed system conditions which cannot be resolved by the  
792 models. Mid-lower crustal samples that experienced stronger degrees of alteration under sub-  
793 greenschist conditions, such as faulted intervals or the pyrrhotite-smectite aggregates in non-faulted  
794 rocks, the lower temperature trend in Model 1 remains the best approach.

795

### 796 **5.3 Sulfur and base metal mobility during hydrothermal alteration**

797 **Figure 13A-D** shows selected base metal and MgO concentrations in the crustal section from shipboard  
798 data (Kelemen et al., 2020) plus reference values for Indian MORB (White and Klein, 2014) and the  
799 axial Geotimes volcanic unit, contemporaneous to the crustal accretion stage (Belgrano et al., 2019).  
800 As evidenced by MgO and Ni concentrations, Geotimes lavas are more differentiated than Indian MORB  
801 (e.g. Godard et al., 2006) with samples from Hole GT3A straddling between both. The mid-lower crustal  
802 gabbros (GT1A and GT2A) show a gradual increase in MgO and Ni downhole due to the combined  
803 effects from increasing primitive character of the melts and olivine accumulation. Mg-Ni troughs  
804 correspond to anorthosite and peaks, to ultramafic layers. Zn concentrations increase stepwise from

805 the layered (Hole GT1A) to the foliated gabbros (Hole GT2A), following an expectable differentiation  
806 trend, but Hole GT3A dike and gabbros concentrations are below the range for the Geotimes lavas.  
807 The high Cu concentrations in the mid-lower crustal section are consistent with early sulfide saturation  
808 and the common occurrence of chalcopyrite in magmatic and hydrothermal sulfide assemblages.  
809 Contrarily to what is observed for Ni or Zn, strongly altered rocks in the lower crust have vanishingly  
810 low Cu concentrations. The dike-gabbro transition section shows a remarkable Cu distribution, with  
811 concentrations close to MORB at the bottom smoothly decreasing to a minimum at ca. 200 m (< 10  
812 ppm), then slowly increasing towards the top of Hole GT3A. A more subtle similar trend can be observed  
813 for Zn. The behavior of Cu and to a lesser extent Zn, in the upper crust suggest moderate to extensive  
814 metal mobilization during hydrothermal alteration. The depletion of Cu in altered rocks of the mid-lower  
815 crustal section is consistent with similar, but localized processes, that did not affect Zn or Ni to the same  
816 extent. Ni and Zn occur in magmatic sulfides, but also in silicates and oxides. Where alteration did not  
817 lead to the formation of secondary sulfides, as in mid-lower crust most altered domains, once the  
818 primary phase is destroyed, Ni and Zn can be re-incorporated in secondary silicate (serpentine,  
819 amphibole) or magnetite, whereas Cu will be transported out of the system.

820

### 821 **5.3.1 A semi-quantitative assessment of Cu, Zn and S mobility in GT3A Hole**

822 An accurate quantification of metal mobilization requires knowledge of chalcophile and immobile  
823 elements in fresh glasses which are currently unavailable for Oman (Jowitt et al., 2012; Patten et al.,  
824 2016). We provide a semi-quantitative assessment of Cu, Zn and S mobilization in the upper crust  
825 frozen melts where metal mobilization was widespread and magmatic accumulation is less likely to  
826 modify primary magmatic concentrations. Estimated magmatic Cu and Zn concentrations were  
827 calculated for each sample from the shipboard dataset based on the regression of metal concentrations  
828 relative to Y measured in Geotimes samples by Belgrano et al. (2019). Because Geotimes lavas are  
829 spilitised and may have experienced base metal mobilization, magmatic values were also computed for  
830 EPR basalts compiled by Gale et al. (2013) for comparison. Results for baseline magmatic  
831 concentrations are quite similar for Zn but lower Cu concentrations are estimated based on Geotimes  
832 lavas (details can be found in Supplementary Materials SM3, Fig.2).

833 Sulfur measurements are unavailable for Oman shipboard samples therefore we rely on MgO-S  
834 relationships from Alt and Shanks (2011) (**Eq. 3**) only for samples studied in this work. Although MgO  
835 is mobile during seawater-rock reactions, net fluxes estimated for the oceanic crust dike section are  
836 mainly zero (Staudigel, 2014). Crucially, Hole GT3A alteration is dominated by albitization and  
837 amphibolitization rather than chlorite formation. Hydrothermal amphiboles most commonly record the  
838 Mg# of the primary pyroxenes (Gillis, 1995), unlike chlorite which can effectively accommodate  
839 seawater Mg, but is largely subordinate to amphibole in Hole GT3A.

840 The final mass balance for Cu, Zn and S is given by **Eq. 7** where  $E^i_{\text{sample}}$  and  $E^i_{\text{magmatic}}$  are the  
841 concentrations of the element measured in the altered sample and estimated for the magmatic protolith,  
842 whereas  $\Delta E^i$  is the mass variation for that element (Jowitt et al., 2012).

843

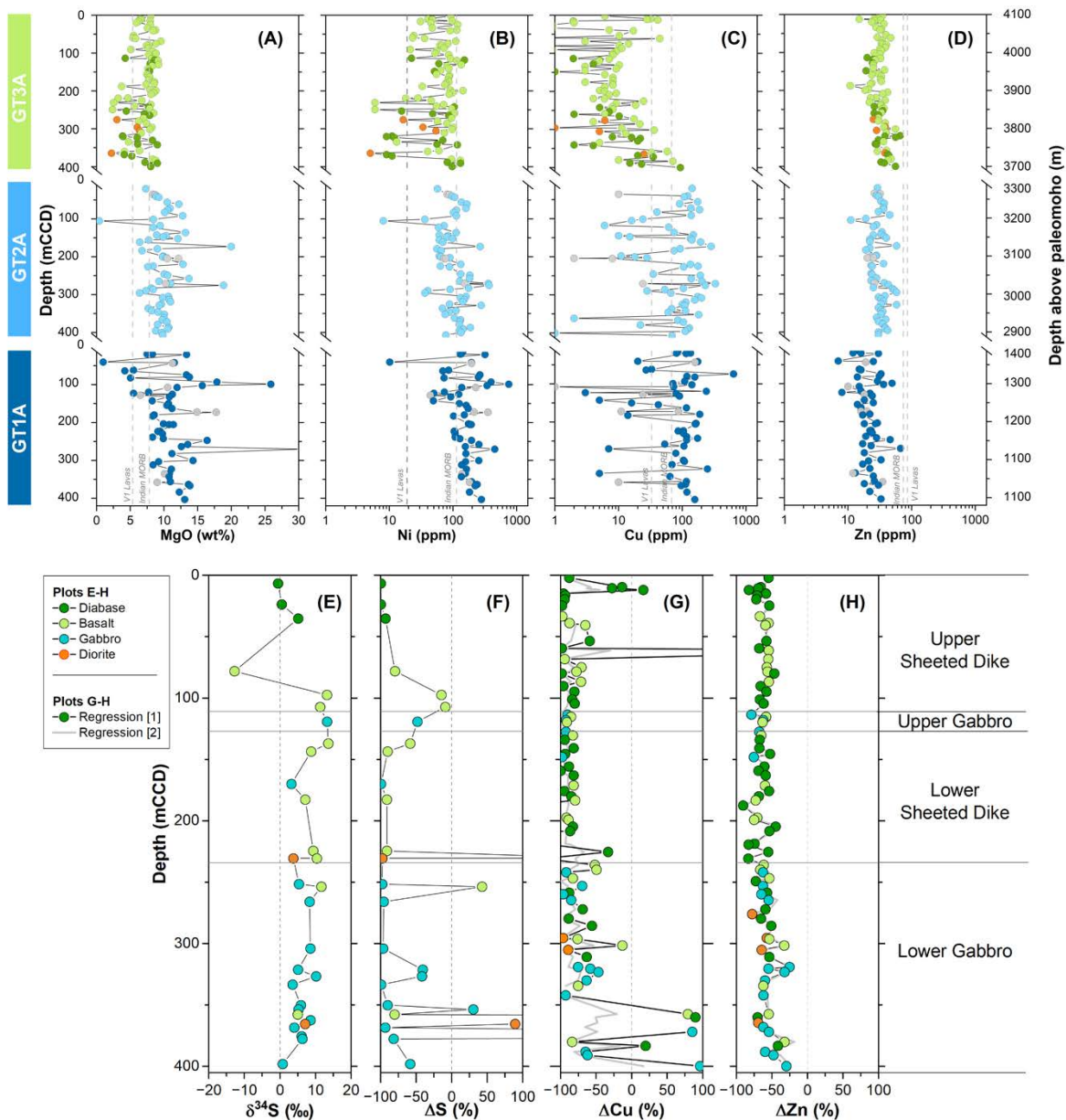
844 Eq. 7 
$$\Delta E^i = \frac{E^i_{\text{sample}} - E^i_{\text{magmatic}}}{E^i_{\text{magmatic}}} * 100$$

845

846 Mass balance for sulfur was made for all samples studied in this work and results are shown in **Figure**  
847 **13E-F** alongside with the isotope values for comparison. **Figure 13G-H** shows the results for Cu and  
848 Zn mass balance using all shipboard samples: the black and grey data series refer to estimates based  
849 on a magmatic baseline that considers Geotimes and EPR basalts magmatic concentrations,  
850 respectively. Details of the regressions are provided in **SM3** and summary statistics are listed in **Table**  
851 **4A**. Results based on Geotimes versus those obtained with EPR lavas are identical for Zn but differ for  
852 Cu. Due to the higher magmatic baseline concentrations for EPR lavas, these estimates indicate more  
853 extreme Cu losses, namely in sections where the Geotimes-based estimates would suggest moderate  
854 Cu-gains (**Figure 13G**). Because currently there are no means to assess how much the Cu magmatic  
855 concentrations in Geotimes lavas might have been lost during spilitization, we will consider these semi-  
856 quantitative results in the forthcoming discussion, as they provide a more conservative estimate of Cu  
857 losses compared to those provided by the EPR baseline.

858 Indeed, regardless of the regression considered, results suggest that most of the studied upper crustal  
859 section experienced extensive (>80%) to near complete leaching of the magmatic sulfur content. Sulfur  
860 gains due to hydrothermal sulfide deposition are restricted to the Hole GT3A Lower Gabbro Sequence.  
861 Rocks that experienced >80% sulfur loss have enriched  $\delta^{34}\text{S}$  values of up to +10‰, whereas those with  
862 heaviest isotopic composition have sulfur losses up to ~60%.

863  $\Delta E^{\text{Zn}}$  estimates are relatively constant, without intervals of major Zn enrichment, as expected  
864 considering the absence of sphalerite and low Zn contents in other sulfide phases. Results confirm that  
865 the uppermost ~12 m of Hole GT3A show the most significant Zn losses ( $X\Delta E^{\text{Zn}} = -68$ ,  $\sigma = 11$ ), compared  
866 to Cu ( $X\Delta E^{\text{Cu}} = -22$ ,  $\sigma = 43$ ). Below this interval, down to ~342 m, Cu losses are extensive to near  
867 complete ( $X\Delta E^{\text{Cu}} = -88$ ,  $\sigma = 17$ ) and show no correlation with sulfur mass variations or isotope signatures,  
868 as exemplified by intervals with higher sulfidation comprising isotopically heavy pyrite. These features  
869 suggest that between 12-342 m Cu was substantially leached out of the system. The lowermost portion  
870 of the hole (below 347 m) is characterized by smaller Cu losses or modest gains due to the greater  
871 presence of chalcopyrite.



872

873 **Figure 13. (A-D)** Cu, Zn, Ni and MgO concentrations for OmanDP Gabbro-Transect drillholes using OmanDP shipboard analyses  
 874 (Kelemen et al., 2020). Reference values: Geotimes V1 lavas (Belgrano et al., 2019; Indian MORB (White and Klein, 2014). (E-  
 875 H) Sulfur and base metal mass balance for the upper crustal section GT3A showing the  $\delta^{34}\text{S}$  Isotope values (E) for comparison;  
 876 consult section 2.2.1 for details on GT3A lithostratigraphy. (F) Mass balance for sulfur based on data obtained in this work. (G-  
 877 H) Mass balance for base metals using OmanDP shipboard data from Kelemen et al., 2020 wherein two regressions lines are  
 878 shown: [1] black line with symbols is based on Geotimes lavas (Belgrano et al., 2019) and [2] grey line (symbols are omitted for  
 879 clarity) is based on regressions using EPR basalts compiled by Gale et al. (2013), for further details consult SM3.

880

## 881 5.4 Implications for fluid circulation in the oceanic crust

### 882 5.4.1 The origin of sulfates in the lower crust

883 Three samples yielded high sulfate fraction extracts ( $\text{TS}_{\text{SO}_4}/\text{TS}_{\text{ext}}$  0.41 to 0.96) with a sulfur isotopic  
 884 composition close to that of Cretaceous seawater,  $+16.1\text{\textperthousand}$  to  $+17.3\text{\textperthousand}$  (Figure 9B). These samples are

885 associated with intervals of intense deformation representative of extensively metasomatized gabbro.  
886 As noted above, these deformed rocks show the effects of extensive magmatic sulfide leaching without  
887 hydrothermal sulfide precipitation, apart from traces of pyrite. Some of these intervals likely correspond  
888 to fault infills of the Zihlmann-Müller-fault zone (ZMFZ, Kelemen et al., 2020; Zihlmann et al., 2018)  
889 intersected in Hole GT1A. As is common in other ocean-crust studies (e.g. Alt and Anderson, 1991) no  
890 sulfates were observed petrographically or imaged using compositional EDS scans in our wall rock  
891 samples (this study). However, thick anhydrite veins (>10 cm) are present associated with brittle  
892 structures in Holes GT1A and GT2A (Kelemen et al., 2020, Teagle et al., 2019), and therefore it is  
893 reasonable that (sub-) microscopic veinlets are present throughout the fault damage zones.

894 The presence of sulfates in deep seated oceanic faults documents the inflow of seawater that  
895 precipitated anhydrite upon reaching temperatures of ~150 °C (Kleine et al., 2022; Seyfried Jr and  
896 Bischoff, 1981; Sleep, 1991; Teagle et al., 2019; Teagle et al., 1998). Anhydrite veins were documented  
897 in the Atlantis Massif (Delacour et al., 2008a) to a depth of 700 m in Hole U1309D whereas Hole GT1A  
898 represents a paleodepth >5 km below the seafloor implying deep-seated hydrothermal recharge. Due  
899 to anhydrite's retrograde solubility, it is commonly assumed that it dissolves back into the oceans during  
900 off-axis circulation within the upper crust (e.g., Alt, 1995; Kleine et al., 2022). The precipitation and  
901 preservation of anhydrite in Holes GT1A and GT2A requires that the lower crust remained at T>150 °C  
902 until the system was effectively closed to seawater interaction. This could occur when high temperature,  
903 upwelling hydrothermal circulation (e.g., as documented in the ZMFZ by Zihlmann et al., 2018) wanned  
904 and downwelling fluids enabled anhydrite precipitation or, spatially close recharge-discharge during the  
905 axial stage. Crucially, the occurrence of Cretaceous seawater sulfate in several fault-zones logged in  
906 Holes GT1A and GT2A, attests to the complexity, and likely longevity, of the plumbing system of deep-  
907 seated fault zones.

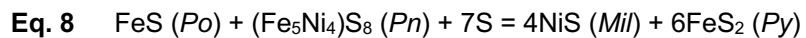
908 Other sulfates identified in the mid-lower crustal section represent a residual amount of the extracted  
909 sulfur fraction in that sample ( $TS_{SO4}/TS_{ext}$  0.01 to 0.09) and display isotopic compositions slightly higher  
910 ( $\delta^{34}S_{SO4}$  +2.8 ‰ to +5.7 ‰) than the coexisting sulfides ( $\delta^{34}S_{Sulfide}$  +0.8 ‰ to +1.2 ‰) resulting in  $\Delta_{SO4-Sulfide}$   
911 between +1.8 ‰ and +5.1 ‰. Abiotic oxidation of sulfide to sulfate under acidic conditions (pH<3)  
912 produces negligible  $\Delta_{SO4-Sulfide}$  (Taylor et al., 1984) whereas under neutral to alkaline conditions (pH 8-  
913 11),  $\Delta_{SO4-Sulfide}$  are  $-5.2 \pm 1.4$  (Fry et al., 1988). Only one sulfate sample from Hole GT3A has negative  
914  $\Delta_{SO4-Sulfide}$  of -1.2 ‰. The strong base metal leaching within Hole GT3A requires acidic, black smoker-  
915 like fluids (Seyfried Jr and Bischoff, 1981), therefore this small negative  $\Delta_{SO4-Sulfide}$  could reflect sulfide  
916 oxidation during the off-axis stage, under the influence of neutral to slightly alkaline seawater. The lower  
917 crustal sulfates showing larger positive  $\Delta_{SO4-Sulfide}$  imply that sulfide oxidation occurred under acidic  
918 conditions, likely under the influence of residual hydrothermal fluids at temperatures between ~ 250-  
919 150 °C where TSR was no longer possible.,.

920

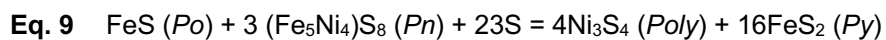
921 **5.4.2 Constraints to hydrothermal circulation in the mid-lower oceanic crust**

922 The secondary sulfide assemblage within mid-lower crust rocks comprises millerite + siegenite-  
 923 polydymite<sub>ss</sub>+ pyrite that formed by replacement of magmatic pyrrhotite-pentlandite in reactions such as  
 924 **Eq. 8** or **Eq. 9**. Chalcopyrite remained stable from the magmatic to hydrothermal stage, although  
 925 dissolution-reprecipitation cannot be excluded based on its occurrence in veins (Figure 4H). Millerite and  
 926 polydymite upper temperature stabilities are bounded at 379 and 356 °C, respectively (Fleet, 2006),  
 927 and their formation requires sulfur input to the system, enabling also the formation of pyrite.

928



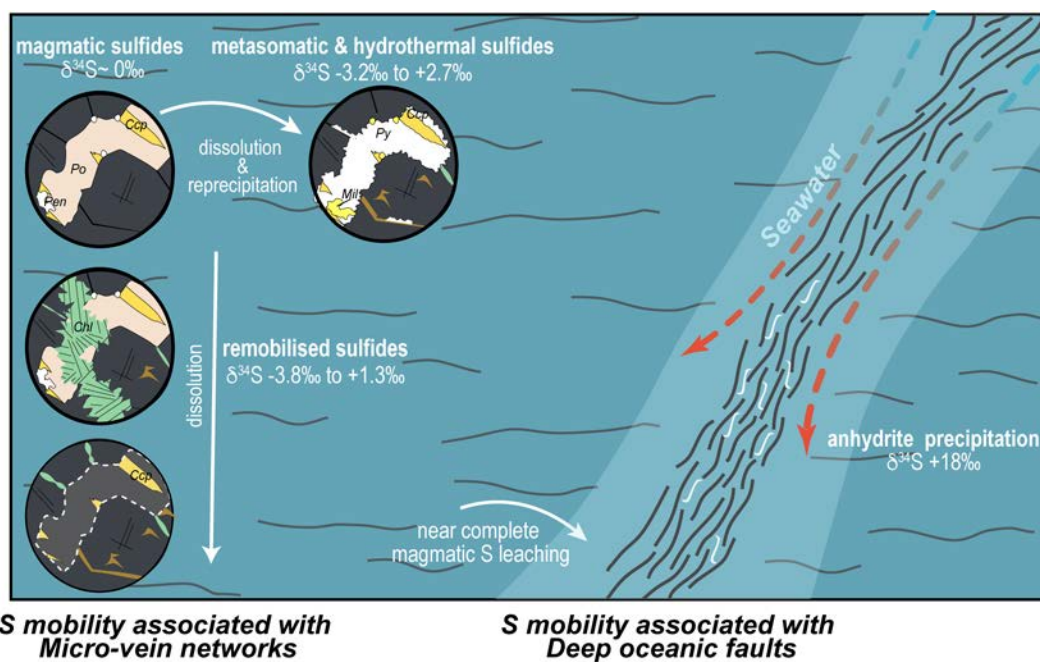
930



932

933 The formation of millerite implies slightly lower sulfur fugacity relative to polydymite-siegentite<sub>ss</sub> and  
 934 indicating higher sulfidation conditions in the foliated (Hole GT2A) relative to the layered (Hole GT1A)  
 935 gabbros, where millerite is comparatively more abundant (

936 **Figure 5**). These mineralogical constraints are consistent with results from isotope modelling that suggest  
 937 the studied mid-lower crustal rocks experienced small additions of seawater-derived sulfur via TSR  
 938 down to ~300 °C (Figure 12A). For a closed system evolution, the isotopic signature of the most  
 939 isotopically modified rock ( $\Delta^{33}\text{S} = -0.014\text{\textperthousand}$ ) requires ~10% input of seawater derived sulfur (Figure 12B-  
 940 C). In-situ isotope measurements show that metasomatic and hydrothermal sulfides express this  
 941 progressive isotopic enrichment relative to magmatic and remobilized sulfide assemblages.



943

944 **Figure 14.** Schematic evolution of sulfur cycling during magmatic and hydrothermal processes in the lower crustal gabbros (Holes  
945 GT1A and GT2A). Mineral abbreviations as in Fig. 4, brown and green veins or patches denote amphibole and chlorite infilling  
946 vein networks, respectively.

947

948 The observations for Hole GT1A and GT2A can be reconciled with the models for lower crustal cooling,  
949 albeit with fundamentally different outcomes on sulfur and metal cycling (**Figure 14**). Away from intervals  
950 affected by fault zones, sulfide and silicate alteration is not pervasive with many sections preserving  
951 intact magmatic sulfide assemblages that also persist as remobilized remnants along with the  
952 hydrothermal sulfides. In these rocks, textural relationships indicate that the microvein network (Bosch  
953 et al., 2004; Manning et al., 2000) played a crucial role in sulfide and metal remobilization (**Figure 4D**).  
954 The minor isotopic resetting suggests these rocks experienced redistribution of magmatic sulfur mixed  
955 with very small inputs of seawater-derived sulfur. As implied by mineral paragenesis, this evolution took  
956 place under very low fluid/rock ratios, moderate sulfur fugacities and essentially preserved base metal  
957 abundances as metasomatic and hydrothermal sulfides. Strongly altered domains such as the ZMFZ  
958 (Zihlmann et al., 2018) and the many faulted intervals present in Holes GT1A and GT2A, preserve lower  
959 temperature, sub-greenschist mineral assemblages and the effects of near-complete sulfur and metal  
960 mobilization. Such structures are the expression of crustal scale channelled hydrothermal fluid flow  
961 (Coogan et al., 2006) and the occurrence of sulfate with a Cretaceous seawater sulfate sulfur isotope  
962 signature (**Figure 9**; Kelemen et al., 2020, Teagle et al., 2019) attests to their open-system behavior,  
963 representing a previously unaccounted sulfur budget introduced in the deep crust.

964

#### 965 **5.4.3 The dike-gabbro transition and the roots of VMS systems**

966 The upper crustal dike-gabbro transition zone sampled by Hole GT3A experienced near-complete  
967 metamorphic recrystallization giving rise to a low variance, higher fS<sub>2</sub> sulfide assemblage (pyrite-  
968 chalcopyrite-bornite). Geochemical modelling of isotopic compositions implies ~20 to 80% incorporation  
969 of seawater derived sulfur (**Figure 12B-E**). To achieve the heavier sulfur isotope compositions (+10 to  
970 +14 ‰) it is necessary to invoke a fluid that experienced isotope enrichment relative to seawater due  
971 to closed-system reservoir effects, likely reflecting limited supply of sulfur into the system. Mass balance  
972 indicates extensive S and Cu losses that were either re-precipitated at higher (not drilled) crustal levels  
973 or vented to the seafloor.

974 The Hole GT3A matrix-forming mineral assemblages formed at low fluid/rock ratios (Kelemen et al,  
975 2020) with the leaching of Cu in most of the Hole (between 12-342 m) requiring temperatures of 350 to  
976 400 °C (Seyfried Jr and Bischoff, 1981) to solubilize Cu into the hydrothermal fluids. The smaller  
977 losses/localized Cu enrichment in the lowermost portion of Hole GT3A (below 347 m) are due to the  
978 formation of hydrothermal chalcopyrite rather than the preservation of magmatic sulfides. These  
979 changes suggest that the hydrothermal fluid may have had decreased capacity to transport Cu. The  
980 Fe/Cu ratio of VMS hydrothermal fluids increases mildly with decreasing pH or increasing chlorine in

981 solution, but is mostly dependent on  $fO_2$  (Seyfried et al., 1997). The major changes in the Hole GT3A  
982 mineralogy at depth reflect the increase in epidote due to increasing  $aCa^{2+}/aH^+$  (Kelemen et al., 2020)  
983 and magnetite in the oxide gabbros which could buffer the fluids at higher Fe/Cu and lower  $fO_2$ , favoring  
984 chalcopyrite precipitation. SIMS measurements show that chalcopyrite has slightly heavier isotope  
985 composition relative to coexisting pyrite and is therefore in isotopic disequilibrium regarding  
986 fractionations to  $H_2S$  (Ohmoto et al., 1979) or, formed from different fluids/stages. Gradual shifting to  
987 lighter isotope compositions toward the bottom of the Lower Gabbros, along with the less pronounced  
988 sulfur losses in this unit, suggests a sulfate-depleted fluid at this depth. Excluding later effects from late  
989 MSR processes, the rocks in the uppermost section of Hole GT3A (above ~90 m) have  $\delta^{34}S$  values of  
990 +5‰ to 0‰. These domains were less affected by sulfur and Cu mobilization and did not experience  
991 hydrothermal sulfide deposition, despite displaying similar silicate alteration assemblages.

992 The lithology-weighted average of isotope compositions for Hole GT3A provides a  $\delta^{34}S$  value of +5.8‰.  
993 This overlaps with the upper range of currently documented VMS deposits in Oman: their  $\delta^{34}S$  values  
994 between -1.1 and +5.4 ‰ are typical of unsedimented ridges (Jesus et al., 2022). Hole GT3A records  
995 significant sulfur isotope variability, with unusually heavy compositions relative to in-situ and ophiolitic  
996 oceanic crust (Figure 11 and references therein). The dynamic magmatic-hydrothermal evolution  
997 proposed for the dike-gabbro transition (Engelhardt et al., 2022; France et al., 2021) and age  
998 relationships recorded in Hole GT3A may elucidate on the causes for such variations (Figure 15).

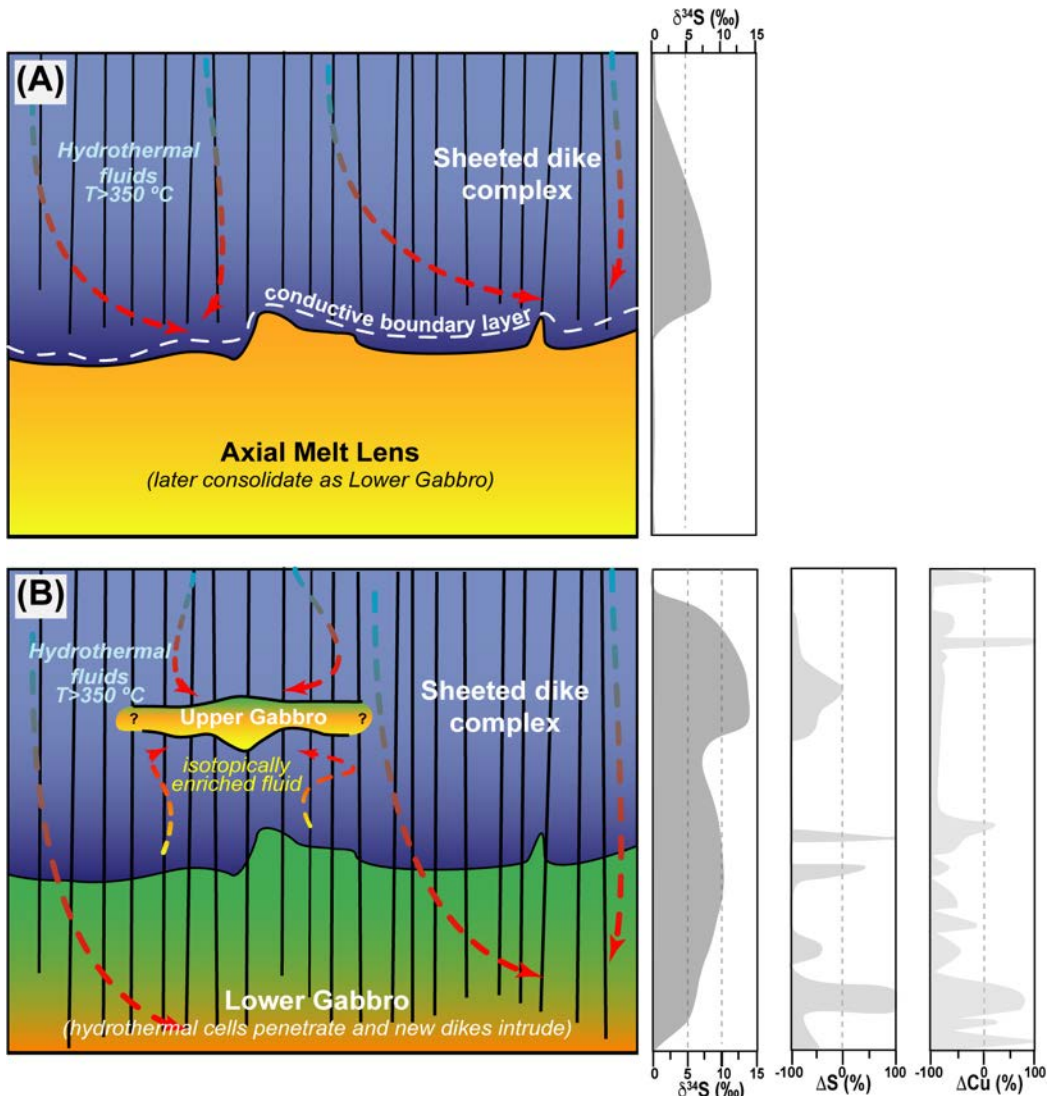
999 (i) The hydrothermal system was initially perched above the axial melt lens (AML) represented  
1000 by the Lower Gabbro, leaching the rocks of the Lower Dike Sequence that now record  $\delta^{34}S$   
1001 values ~+10‰. (Figure 15A).

1002 (ii) Once the Lower Gabbro consolidated, the hydrothermal cells could penetrate, progressing  
1003 downward into the AML (e.g. Gillis, 1995) and gradually forming isotopically lighter sulfides.  
1004 Less comprehensive leaching of S and Cu also lead to increasing abundance in  
1005 chalcopyrite. (Figure 15B).

1006 (iii) Relative ages based on cross-cutting relationships for Hole GT3A decrease upwards,  
1007 suggesting that the Upper Gabbro Sequence was emplaced (slightly?) later, which could  
1008 have triggered a renewed period of hydrothermal activity. Although the three dimensional  
1009 geometry of the Upper Gabbro precludes precise assumptions, the localized isotopic  
1010 enrichments within ±10 m of this Unit (Figure 13) and increasing  $\delta^{34}S$  toward pyrite grain  
1011 borders (Figure 3A), are consistent with efficient focalizing of an isotopically heavy, rapidly  
1012 evolving fluid (Figure 15B). The origin of the isotopically enriched fluid (supported by our  
1013 geochemical modelling) could lie on recycling of mature hydrothermal fluids from  
1014 previous/on-going hydrothermal activity beneath.

1015 (iv) The transition to isotope compositions closer to MORB in the remainder ~90 m of the Upper  
1016 Sheeted Dike suggests a fluid buffered by magmatic sulfur outside of the influence of the  
1017 underlying Upper Gabbro. Although these values are closer to the compositional range of  
1018 Oman VMS deposits or the sheeted dike section in Troodos (Alt, 1994) the relatively abrupt

1019 transition from fundamentally different isotopic domains and the unknown features of the  
 1020 thick crustal section above, advise caution in making further extrapolations to the actual  
 1021 relationship with the sulfur isotope compositions of VMS fluids.



1039 **Figure 15.** Schematic evolution of sulfur cycling during magmatic and hydrothermal processes in the dike-gabbro transition (Hole  
 1040 GT3A). **(A)** Initial stage where the Lower Gabbro (Axial Melt Lens- AML) is unconsolidated and separated from the overlying  
 1041 hydrothermal system by an thermal conductive boundary layer.  $\delta^{34}\text{S}$  would be bounded by the current composition of the Upper  
 1042 Dikes. **(B)** The hydrothermal system penetrates the now consolidated Lower Gabbro while it is extensively intruded by new dikes.  
 1043 The thin Upper Gabbro is meanwhile emplaced and quickly consolidates above being modified by a possible isotopically enriched  
 1044 fluid. The diagrams on the right schematically show the isotope, sulfur and base metal loss profiles currently observed.

1045  
 1046 Despite its unusual isotopic variations, the upper crustal section drilled in Hole GT3A has many of the  
 1047 ingredients of a deep reaction zone of a VMS hydrothermal system (Hannington, 2014). The degree of  
 1048 Cu mobilization here estimated (based on Geotimes lavas, see section 5.3.1) is akin to that reported in

1049 diabase and epidosites of the Troodos ophiolite (Jowitt et al., 2012) although slightly lower for Zn.  
1050 Integrated weighted averages for S and metals mobilized in the Hole GT3A Sequence (**Table 4**) show  
1051 that 1 km<sup>3</sup> of crust can release 2712 kt S, 74.6 kt Cu and 144 kt Zn. These values are within the range  
1052 of the amount of metal released in the epidosite areas of Troodos (Jowitt et al., 2012). An average-  
1053 sized VMS deposit in Oman hosted in axial Geotimes lavas has ~1 Mt ore @ 2% Cu=20 kt, 0.5% Zn=5kt  
1054 and is constituted by ~80% of pyrite equating to 424 kt of sulfur (Cravinho et al., 2023; Gilgen et al.,  
1055 2014), much less than the amount of metal estimated to be mobilised in Hole GT3A. A twofold area (2  
1056 km<sup>3</sup>) would be necessary to produce a large 8 Mt deposit like Mandoos (Cravinho et al., 2023). These  
1057 results concur with observations by Nehlig et al. (1994), that hydrothermal leaching of metals and S do  
1058 not necessarily require the formation of epidosites, which were not documented in Hole GT3A. The  
1059 isotope shifts, and the most conservative estimates of metal and S leaching in Hole GT3A samples are  
1060 far more extensive than reported in in-situ oceanic crust (Alt et al., 2010; Alt et al., 1996; Gillis, 1995;  
1061 Gillis et al., 2001; Heft et al., 2008; Patten et al., 2016), reinforcing the view that ophiolitic crust  
1062 experienced larger hydrothermal fluxes than in-situ Mid Ocean Ridges (Bickle and Teagle, 1992; Alt  
1063 and Teagle, 2000).

1064

## 1065 **6 CONCLUSIONS**

1066 The sheeted dike – gabbro transition sampled by Hole GT3A records wide variations in sulfur isotope  
1067 compositions, with unusually high  $\delta^{34}\text{S}$  values compared to in-situ or ophiolitic crust and an integrated  
1068 composition of +5.8‰. The low sulfide-sulfur concentrations and heavy sulfur isotope signatures are  
1069 consistent with abiogenic thermochemical sulfate reduction reactions during intense hydrothermal  
1070 alteration under greenschist facies conditions. This produced a low-variance and relatively high-fS<sub>2</sub>  
1071 assemblage of pyrite  $\pm$  chalcopyrite  $\pm$  bornite. The Lower Gabbro Sequence records minor sulfur  
1072 additions and progressively lighter isotope signatures with depth which reflect decreasing availability of  
1073 seawater derived sulfate in the hydrothermal fluid following the gabbro consolidation. The heaviest  
1074 sulfur isotope compositions ( $\delta^{34}\text{S}$  of +10 to +14 ‰) occur within  $\pm$ 10 m of the Upper Gabbro and can be  
1075 explained by a focalized fluid that experienced isotope enrichment relative to seawater due to closed-  
1076 system reservoir effects. The overlying Upper Sheeted Dike Sequence records pronounced  $\delta^{34}\text{S}$  values  
1077 closer to MORB values (<+5.1‰) due to magmatic sulfur leaching without associated hydrothermal  
1078 sulfide deposition. This suggests the influence of a fluid buffered by magmatic S isotopic compositions,  
1079 closer to the signatures of Oman VMS deposits. Rare negative  $\delta^{34}\text{S}$  values resulted from late addition  
1080 of small amounts of biogenic sulfur, likely during post-axial stages. Hole GT3A has all the features of a  
1081 deep hydrothermal reaction zone with incorporation of up to ~80% seawater derived sulfate and  
1082 extensive S and Cu losses that were either re-precipitated at higher crustal levels or vented to the  
1083 seafloor. The amount of metal released in a 1 km<sup>3</sup> crustal section like Hole GT3A represents ~3-fold  
1084 the typical metal endowment of VMS deposits hosted in the axial lavas of Oman.

1085 The mid to lower crustal section sampled by Holes GT2A and GT1A mostly preserves MORB sulfur  
1086 isotope signatures and highly variable sulfur contents. Away from fault zones, a silicate microvein  
1087 network enabled sulfide and metal remobilization of magmatic sulfide assemblages along with formation

1088 of millerite + siegenite-polydimitite<sub>ss</sub> + pyrite. These reactions imply small additions of sulfur, expressed  
1089 by progressive isotopic enrichment in metasomatic or hydrothermal sulfides relative to magmatic or  
1090 remobilized sulfides. The mid-lower crustal section experienced redistribution of magmatic sulfur mixed  
1091 with very small inputs of seawater-derived sulfur (< 10%), under very low fluid/rock ratios, moderate  
1092 sulfur fugacities that essentially preserved base metal abundances in secondary sulfides.

1093 Strongly altered domains (sub-greenschist facies) related with the many faulted intervals in Holes GT1A  
1094 and GT2A, record near complete leaching of magmatic sulfides without the deposition of secondary  
1095 sulfides. The near-complete sulfur and metal mobilization and occurrence of sulfate with a Cretaceous  
1096 seawater sulfate isotope composition attest to open system behaviour. These structures are the  
1097 expression of crustal scale channeled hydrothermal fluid flow and preserve a previously unaccounted  
1098 sulfur budget introduced in the deep crust.

1099

## 1100                   **Acknowledgments**

1101 This work utilized samples from the Oman Drilling (OmanDP) that has been possible through co-  
1102 mingled funds from the International Continental Scientific Drilling Project (ICDP; Kelemen, Matter,  
1103 Teagle Lead PIs), the Sloan Foundation– Deep Carbon Observatory (Grant 2014-3-01, Kelemen PI),  
1104 the National Science Foundation (NSF-EAR-1516300, Kelemen lead PI), NASA– Astrobiology Institute  
1105 (NNA15BB02A, Templeton PI), the German Research Foundation (DFG: KO 1723/21-1, Koepke PI),  
1106 the Japanese Society for the Promotion of Science (JSPS no:16H06347, Michibayashi PI; and  
1107 KAKENHI 16H02742, Takazawa PI), the European Research Council (Adv: no.669972; Jamveit PI),  
1108 the Swiss National Science Foundation (SNF:20FI21\_163073, Früh-Green PI), JAMSTEC, the TAMU-  
1109 JR Science Operator, and contributions from the Sultanate of Oman Ministry of Regional Municipalities  
1110 and Water Resources, the Oman Public Authority of Mining, Sultan Qaboos University, CNRS-Univ.  
1111 Montpellier, Columbia University of New York, and the University of Southampton. The NordSIMS  
1112 facility in Stockholm operates as Swedish Research Council infrastructure (grant 2017-00256); this is  
1113 NordSIMS publication ###.

1114 AJ received funding from WWU Fellowships for International Visiting Scholars, European Union’s  
1115 Horizon 2020 research and innovation program under the Marie Skłodowska-Curie grant agreement  
1116 No 894599 and thru Instituto Dom Luiz Project FCT/UIDB/50019/2020 – IDL funded by FCT. DT and  
1117 MH were in part funded by NERC grant NE/W007517/1. We are grateful to Dr Esther Schwarzenbach,  
1118 Dr Clifford Patten and Manuel Dias for assisting with modelling of sulfur geochemistry processes and  
1119 to Dr Tom Belgrano for lively discussions on the geochemistry of the Oman lavas. André Cravinho  
1120 assistance with figure drawing is warmly acknowledged.

1121

## 1122                   **Tables**

1123

1124 **Table 1.** Sulfur and sulfate contents and corresponding  $\delta^{34}\text{S}$  isotope composition extracted from bulk  
1125 rocks.

1126 **Table 2.** Multiple sulfur isotope composition extracted from selected bulk rocks.

1127 **Table 3.**  $\delta^{34}\text{S}$  values measured in-situ for selected samples.

1128 **Table 4. (A)** Summary statistics for mass balance of S (using measurements on samples from this  
1129 work), Cu and Zn (using all shipboard samples) in Hole GT3A (see text for details). **(B)** Estimated mass  
1130 of sulfur and metals released during hydrothermal alteration of GT3A rocks using section length  
1131 weighted average of results from table A. Samples recording S or metal gains were excluded, it is  
1132 assumed the corresponding mobilized mass was redistributed within the crust. Densities for each  
1133 sequence from shipboard data (Kelemen et al., 2020).

1134

1135 **Supplementary Material**

1136 **Supplementary Material 1. (SM1)** SM1Table 1. Mineral data for studied Sulphide phases.

1137

1138 **Supplementary Material 2. (SM2)** Supporting data related with sulfur geochemistry.

1139

1140

1141 **Supplementary Material 3. (SM3)** Supporting material regarding calculation of base metal magmatic  
1142 concentrations in Oman lavas.

1143

1144

1145

1146

1147

1148 References

1149

1150 Abily, B., Ceuleneer, G., Launeau, P., 2011. Synmagmatic normal faulting in the lower oceanic crust:  
1151 Evidence from the Oman ophiolite. *Geology* 39, 391-394.

1152 Alabaster, T., Pearce, J.A., Malpas, J., 1982. The Volcanic Stratigraphy and Petrogenesis of the Oman  
1153 Ophiolite Complex. *Contributions to Mineralogy and Petrology* 81, 168-183.

1154 Alford, S.E., Alt, J.C., Shanks III, W.C., 2011. Sulfur geochemistry and microbial sulfate reduction during  
1155 low-temperature alteration of uplifted lower oceanic crust: Insights from ODP Hole 735B.  
1156 Chemical Geology 286, 185-195.

1157 Alt, J.C., 1994. A sulfur isotopic profile through the Troodos ophiolite, Cyprus: primary composition and  
1158 the effects of seawater hydrothermal alteration. *Geochimica et Cosmochimica Acta* 58, 1825-  
1159 1840.

1160 Alt, J.C., 1995. Subseafloor processes in mid-ocean ridge hydrothermal systems. *GEOPHYSICAL  
1161 MONOGRAPH-AMERICAN GEOPHYSICAL UNION* 91, 85-85.

1162 Alt, J.C., Anderson, T.F., 1991. Mineralogy and isotopic composition of sulfur in layer 3 gabbros from  
1163 the Indian Ocean, Hole 735B, *Proc. Ocean Drill. Program Sci. Results*, pp. 113-125.

1164 Alt, J.C., Anderson, T.F., Bonnell, L., 1989. The geochemistry of sulfur in a 1.3 km section of  
1165 hydrothermally altered oceanic crust, DSDP Hole 504B. *Geochimica et Cosmochimica Acta*  
1166 53, 1011-1023.

1167 Alt, J.C., Laverne, C., Coggon, R.M., Teagle, D.A., Banerjee, N.R., Morgan, S., Smith-Duque, C.E.,  
1168 Harris, M., Galli, L., 2010. Subsurface structure of a submarine hydrothermal system in ocean  
1169 crust formed at the East Pacific Rise, ODP/IODP Site 1256. *Geochemistry, Geophysics,  
1170 Geosystems* 11.

1171 Alt, J.C., Laverne, C., Vanko, D.A., Tartarotti, P., Teagle, D.A., Bach, W., Zuleger, E., Erzinger, J.,  
1172 Honnorez, J., Pezard, P.A., 1996. 34. Hydrothermal alteration of a section of upper oceanic  
1173 crust in the Eastern Equatorial Pacific: a synthesis of results from site 504 (DSDP LEGS 69,  
1174 70, and 83, and ODP LEGS 111, 137,140, and 148), *Proceedings of the Ocean Drilling  
1175 Program, scientific results*, pp. 417-434.

1176 Alt, J.C., Shanks, W.C., 2011. Microbial sulfate reduction and the sulfur budget for a complete section  
1177 of altered oceanic basalts, IODP Hole 1256D (eastern Pacific). *Earth and Planetary Science  
1178 Letters* 310, 73-83.

1179 Alt, J.C., Shanks, W.C., Bach, W., Paulick, H., Garrido, C.J., Beaudoin, G., 2007. Hydrothermal  
1180 alteration and microbial sulfate reduction in peridotite and gabbro exposed by detachment  
1181 faulting at the Mid-Atlantic Ridge, 15° 20' N (ODP Leg 209): A sulfur and oxygen isotope study.  
1182 *Geochemistry, Geophysics, Geosystems* 8.

1183 Alt, J.C., Teagle, D.A.H., 2000. Hydrothermal alteration and fluid fluxes in ophiolites and oceanic crust,  
1184 in: Dilek, Y., Moores, E.M., Elthon, D., Nicolas, A. (Eds.), *Ophiolites and oceanic crust: new  
1185 insights from field studies and the Ocean Drilling Program*. Geological Society of America,  
1186 *Sepcial Paper* 349:273-282.

1187 Alt, J.C., Zuleger, E., Erzinger, J., 1995. Mineralogy and stable isotopic compositions of the  
1188 hydrothermally altered lower sheeted dike complex, Hole 504B, Leg 140, *Proceedings of the  
1189 Ocean Drilling Program, Scientific Results*. Citeseer, pp. 155-166.

1190 Anonymous, 1972. Penrose field conference on ophiolites. *Geotimes* 17, 24-25.

1191 Bach, W., Edwards, K.J., 2003. Iron and sulfide oxidation within the basaltic ocean crust: implications  
1192 for chemolithoautotrophic microbial biomass production. *Geochimica et Cosmochimica Acta*  
1193 67, 3871-3887.

1194 Barker, A.K., Coogan, L.A., Gillis, K.M., 2010. Insights into the behaviour of sulphur in mid-ocean ridge  
1195 axial hydrothermal systems from the composition of the sheeted dyke complex at Pito Deep.  
1196 *Chemical Geology* 275, 105-115.

1197 Belgrano, T.M., Diamond, L.W., Vogt, Y., Biedermann, A.R., Gilgen, S., Al-Tobi, K., 2019. A revised  
1198 map of volcanic units in the Oman ophiolite: insights into the architecture of an oceanic proto-  
1199 arc volcanic sequence. *Solid Earth* 10, 1181-1217.

1200 Benoit, M., Polv , M., Ceuleneer, G., 1996. Trace element and isotopic characterization of mafic  
1201 cumulates in a fossil mantle diapir (Oman ophiolite). *Chemical Geology* 134, 199-214.

1202 Bosch, D., Jamais, M., Boudier, F., Nicolas, A., Dautria, J.-M., Agrinier, P., 2004. Deep and high-  
1203 temperature hydrothermal circulation in the Oman ophiolite—petrological and isotopic  
1204 evidence. *Journal of Petrology* 45, 1181-1208.

1205 Cabral, R.A., Jackson, M.G., Rose-Koga, E.F., Koga, K.T., Whitehouse, M.J., Antonelli, M.A., Farquhar,  
1206 J., Day, J., Hauri, E.H., 2013. Anomalous sulphur isotopes in plume lavas reveal deep mantle  
1207 storage of Archaean crust. *Nature* 496, 490-493.

1208 Canfield, D., 2001. Biogeochemistry of sulfur isotopes. *Reviews in Mineralogy and Geochemistry* 43,  
1209 607-636.

1210 Canfield, D.E., 2004. The evolution of the Earth surface sulfur reservoir. *American Journal of Science*  
1211 304, 839-861.

1212 Canfield, D.E., Raiswell, R., Westrich, J.T., Reaves, C.M., Berner, R.A., 1986. The use of chromium  
1213 reduction in the analysis of reduced inorganic sulfur in sediments and shales. *Chemical  
1214 Geology* 54, 149-155.

1215 Coogan, L., Howard, K., Gillis, K., Bickle, M., Chapman, H., Boyce, A., Jenkin, G., Wilson, R., 2006.  
1216 Chemical and thermal constraints on focussed fluid flow in the lower oceanic crust. *American  
1217 Journal of Science* 306, 389-427.

1218 Coogan, L.A., Mitchell, N.C., O'Hara, M.J., 2003. Roof assimilation at fast spreading ridges: An  
1219 investigation combining geophysical, geochemical, and field evidence. *Journal of Geophysical  
1220 Research: Solid Earth* 108, ECV 2-1-ECV 2-14.

1221 Cravinho, A., Jesus, A.P., Moreira, B., Mateus, A., Pracejus, B., Figueiras, J., Benoit, M., Bauer, W.,  
1222 Rocha, F., 2023. Contrasting Features and Volcanostratigraphy of the Mafic-Hosted Mandoos  
1223 and Shinas Volcanogenic Massive Sulfide Deposits, Samail Ophiolite, Oman. *Economic  
1224 Geology*.

1225 Crowe, D., Vaughan, R., 1996. Characterization and use of isotopically homogeneous standards for in  
1226 situ laser microprobe analysis of  $^{34}\text{S}/^{32}\text{S}$  ratios. *American Mineralogist* 81, 187-193.

1227 Delacour, A., Früh-Green, G.L., Bernasconi, S.M., 2008a. Sulfur mineralogy and geochemistry of  
1228 serpentinites and gabbros of the Atlantis Massif (IODP Site U1309). *Geochimica et*  
1229 *Cosmochimica Acta* 72, 5111-5127.

1230 Delacour, A., Früh-Green, G.L., Bernasconi, S.M., Kelley, D.S., 2008b. Sulfur in peridotites and gabbros  
1231 at Lost City ( $30^\circ\text{N}$ , MAR): Implications for hydrothermal alteration and microbial activity during  
1232 serpentinization. *Geochimica et Cosmochimica Acta* 72, 5090-5110.

1233 Dilek, Y., Furnes, H., 2014. Ophiolites and their origins. *Elements* 10, 93-100.

1234 Engelhardt, A., Koepke, J., Zhang, C., Garbe-Schönberg, D., Jesus, A.P., 2022. ICDP Oman Drilling  
1235 Project: varitextured gabbros from the dike–gabbro transition within drill core GT3A. *European*  
1236 *Journal of Mineralogy* 34, 603-626.

1237 Farquhar, J., Jackson, T.L., Thiemens, M.H., 2000. A  $^{33}\text{S}$  enrichment in ureilite meteorites: evidence  
1238 for a nebular sulfur component. *Geochimica et Cosmochimica Acta* 64, 1819-1825.

1239 Fleet, M.E., 2006. Phase equilibria at high temperatures. *Reviews in Mineralogy and Geochemistry* 61,  
1240 365-419.

1241 France, L., Lombard, M., Nicollet, C., Berthod, C., Debret, B., Koepke, J., Ildefonse, B., Toussaint, A.,  
1242 2021. Quantifying the axial magma lens dynamics at the roof of oceanic magma reservoirs  
1243 (dike/gabbro transition): Oman Drilling Project GT3 site survey. *Journal of Geophysical*  
1244 *Research: Solid Earth*.

1245 Fry, B., Ruf, W., Gest, H., Hayes, J.M., 1988. Sulfur isotope effects associated with oxidation of sulfide  
1246 by  $\text{O}_2$  in aqueous solution. *Chemical Geology: Isotope Geoscience section* 73, 205-210.

1247 Gale, A., Dalton C. A., Langmuir, C. H., Su, Y., Schilling, J.G., 2013. The mean composition of ocean  
1248 ridge basalts. *Geochemistry, Geophysics, Geosystems*: 14: 489-518. Gilgen, S.A., Diamond,  
1249 L.W., Mercolli, I., 2016. Sub-seafloor epidote alteration: Timing, depth and stratigraphic  
1250 distribution in the Semail ophiolite, Oman. *Lithos* 260, 191-210.

1251 Gilgen, S.A., Diamond, L.W., Mercolli, I., Al-Tobi, K., Maidment, D.W., Close, R., Al-Towaya, A., 2014.  
1252 Volcanostratigraphic Controls on the Occurrence of Massive Sulfide Deposits in the Semail  
1253 Ophiolite, Oman. *Economic Geology* 109, 1585-1610.

1254 Gillis, K.M., 1995. Controls on hydrothermal alteration in a section of fast-spreading oceanic crust. *Earth*  
1255 and *Planetary Science Letters* 134, 473-489.

1256 Gillis, K.M., 2008. The roof of an axial magma chamber: A hornfelsic heat exchanger. *Geology* 36, 299-  
1257 302.

1258 Gillis, K.M., Muehlenbachs, K., Stewart, M., Gleeson, T., Karson, J., 2001. Fluid flow patterns in fast  
1259 spreading East Pacific Rise crust exposed at Hess Deep. *Journal of Geophysical Research: Solid Earth* 106, 26311-26329.

1261 Godard, M., Bosch, D., Einaudi, F., 2006. A MORB source for low-Ti magmatism in the Semail ophiolite. *Chemical Geology* 234, 58-78.

1263 Goodenough, K.M., Thomas, R.J., Styles, M.T., Schofield, D.I., MacLeod, C.J., 2014. Records of ocean  
1264 growth and destruction in the Oman–UAE ophiolite. *Elements* 10, 109-114.

1265 Hannington, M., 2014. Volcanogenic massive sulphide deposits In: Holland HD, Turekian KK (ed)  
1266 *Treatise on geochemistry* 2nd edition. Elsevier Ltd.

1267 Harper, G.D., Bowman, J.R., Kuhns, R., 1988. A field, chemical, and stable isotope study of subseafloor  
1268 metamorphism of the Josephine ophiolite, California-Oregon. *Journal of Geophysical Research: Solid Earth* 93, 4625-4656.

1270 Harris, M., Coggon, R.M., Smith-Duque, C.E., Cooper, M.J., Milton, J.A., Teagle, D.A.H., 2015.  
1271 Channelling of hydrothermal fluids during the accretion and evolution of the upper oceanic  
1272 crust: Sr isotope evidence from ODP Hole 1256D. *Earth and Planetary Science Letters* 416,  
1273 56-66.

1274 Heft, K.L., Gillis, K.M., Pollock, M.A., Karson, J.A., Klein, E.M., 2008. Role of upwelling hydrothermal  
1275 fluids in the development of alteration patterns at fast spreading ridges: Evidence from the  
1276 sheeted dike complex at Pito Deep. *Geochemistry, Geophysics, Geosystems* 9.

1277 Jesus, A.P., Strauss, H., Benoit, M., Goncalves, M., Santos, A., 2022. Strontium and multiple sulfur  
1278 isotopic constraints on Volcanogenic Massive Sulfide (VMS) deposits in the Oman ophiolite,  
1279 2022 Goldschmidt Conference. *GOLDSCHMIDT*.

1280 Johnston, D.T., Gill, B.C., Masterson, A., Beirne, E., Casciotti, K.L., Knapp, A.N., Berelson, W., 2014.  
1281 Placing an upper limit on cryptic marine sulphur cycling. *Nature* 513, 530-533.

1282 Jowitt, S.M., Jenkin, G.R., Coogan, L.A., Naden, J., 2012. Quantifying the release of base metals from  
1283 source rocks for volcanogenic massive sulfide deposits: Effects of protolith composition and  
1284 alteration mineralogy. *Journal of Geochemical Exploration* 118, 47-59.

1285 Kampschulte, A., Strauss, H., 2004. The sulfur isotopic evolution of Phanerozoic seawater based on  
1286 the analysis of structurally substituted sulfate in carbonates. *Chemical Geology* 204, 255-286.

1287 Kelemen, P., Matter, J., Teagle, D.A.H., Coggon, J.A., Team, O.D.P.S., 2020. Proceedings of the Oman  
1288 Drilling Project: College Station, TX (International Ocean Discovery Program). .

1289 Kelemen, P.B., Koga, K., Shimizu, N., 1997. Geochemistry of gabbro sills in the crust-mantle transition  
1290 zone of the Oman ophiolite: implications for the origin of the oceanic lower crust. *Earth and Planetary Science Letters* 146, 475-488.

1292 Kleine, B.I., Stefánsson, A., Zierenberg, R.A., Jeon, H., Whitehouse, M.J., Jónasson, K., Fridleifsson,  
1293 G.Ó., Weisenberger, T.B., 2022. Sulfate (re-) cycling in the oceanic crust: Effects of seawater-  
1294 rock interaction, sulfur reduction and temperature on the abundance and isotope composition  
1295 of anhydrite. *Geochimica et Cosmochimica Acta* 317, 65-90.

1296 Koepke, J., Schoenborn, S., Oelze, M., Wittmann, H., Feig, S., Hellebrand, E., Boudier, F., Schoenberg,  
1297 R., 2009. Petrogenesis of crustal wehrlites in the Oman ophiolite: Experiments and natural  
1298 rocks. *Geochemistry, Geophysics, Geosystems* 10, n/a-n/a.

1299 Labidi, J., Cartigny, P., Birck, J.L., Assayag, N., Bourrand, J.J., 2012. Determination of multiple sulfur  
1300 isotopes in glasses: A reappraisal of the MORB  $\delta$ 34S. *Chemical Geology* 334, 189-198.

1301 Labidi, J., Cartigny, P., Hamelin, C., Moreira, M., Dosso, L., 2014. Sulfur isotope budget (32S, 33S, 34S  
1302 and 36S) in Pacific–Antarctic ridge basalts: A record of mantle source heterogeneity and  
1303 hydrothermal sulfide assimilation. *Geochimica et Cosmochimica Acta* 133, 47-67.

1304 LaFlamme, C., Martin, L., Jeon, H., Reddy, S.M., Selvaraja, V., Caruso, S., Bui, T.H., Roberts, M.P.,  
1305 Voute, F., Hagemann, S., 2016. In situ multiple sulfur isotope analysis by SIMS of pyrite,  
1306 chalcopyrite, pyrrhotite, and pentlandite to refine magmatic ore genetic models. *Chemical  
1307 Geology* 444, 1-15.

1308 Lecuyer, C., Reynard, B., 1996. High-temperature alteration of oceanic gabbros by seawater (Hess  
1309 Deep, Ocean Drilling Program Leg 147): Evidence from oxygen isotopes and elemental fluxes.  
1310 *Journal of Geophysical Research: Solid Earth* 101, 15883-15897.

1311 Li, C., Ripley, E.M., 2009. Sulfur contents at sulfide-liquid or anhydrite saturation in silicate melts:  
1312 empirical equations and example applications. *Economic Geology* 104, 405-412.

1313 Li, R., Xia, X., Yang, S., Chen, H., Yang, Q., 2019. Off-mount calibration and one new potential  
1314 pyrrhotite reference material for sulfur isotope measurement by secondary ion mass  
1315 spectrometry. *Geostandards and Geoanalytical Research* 43, 177-187.

1316 Lippard, S.J., 1986. The ophiolite of northern Oman. *Geological Society London Memoir* 11, 178.

1317 Liseroudi, M.H., Ardakani, O.H., Pedersen, P.K., Stern, R.A., Wood, J.M., Sanei, H., 2021. Microbial  
1318 and thermochemical controlled sulfur cycle in the Early Triassic sediments of the Western  
1319 Canadian Sedimentary Basin. *Journal of the Geological Society* 178, jgs2020-2175.

1320 Liu, Y., Samaha, N.-T., Baker, D.R., 2007. Sulfur concentration at sulfide saturation (SCSS) in  
1321 magmatic silicate melts. *Geochimica et Cosmochimica Acta* 71, 1783-1799.

1322 MacLeod, C.J., Yaouancq, G., 2000. A fossil melt lens in the Oman ophiolite: Implications for magma  
1323 chamber processes at fast spreading ridges. *Earth and Planetary Science Letters* 176, 357-  
1324 373.

1325 Manning, C.E., MacLeod, C.J., Weston, P.E., 2000. Lower-crustal cracking front at fast-spreading  
1326 ridges: Evidence from the East Pacific Rise and the Oman ophiolite. Special Papers-  
1327 Geological Society of America, 261-272.

1328 Masterson, A., Wing, B.A., Paytan, A., Farquhar, J., Johnston, D.T., 2016. The minor sulfur isotope  
1329 composition of Cretaceous and Cenozoic seawater sulfate. Paleoceanography 31, 779-788.

1330 Mathez, E., 1976. 31. SULFIDE RELATIONS IN HOLE 418A FLOWS AND SULFUR CONTENTS OF  
1331 GLASSES. Initial Reports of the Deep Sea Drilling Project: A Project Planned by and Carried  
1332 Out with the Advice of the Joint Oceanographic Institutions for Deep Earth Sampling 51, 1069.

1333 McCollom, T.M., Shock, E.L., 1998. Fluid-rock interactions in the lower oceanic crust: Thermodynamic  
1334 models of hydrothermal alteration. Journal of Geophysical Research: Solid Earth 103, 547-  
1335 575.

1336 Nehlig, P., Juteau, T., Bendel, V., Cotten, J., 1994. The root zones of oceanic hydrothermal systems:  
1337 Constraints from the Samail ophiolite (Oman). Journal of Geophysical Research: Solid Earth  
1338 (1978–2012) 99, 4703-4713.

1339 Nicolas, A., Boudier, F., Ildefonse, B., Ball, E., 2000. Accretion of Oman and United Arab Emirates  
1340 ophiolite—Discussion of a new structural map. Marine Geophysical Researches 21, 147-180.

1341 Oeser, M., Strauss, H., Wolff, P.E., Koepke, J., Peters, M., Garbe-Schönberg, D., Dietrich, M., 2012. A  
1342 profile of multiple sulfur isotopes through the Oman ophiolite. Chemical Geology 312, 27-46.

1343 Ohmoto, H., Lasaga, A.C., 1982. Kinetics of reactions between aqueous sulfates and sulfides in  
1344 hydrothermal systems. Geochimica et Cosmochimica Acta 46, 1727-1745.

1345 Ohmoto, H., Rye, R., Barnes, H., 1979. Geochemistry of hydrothermal ore deposits.

1346 Ono, S., Shanks III, W.C., Rouxel, O.J., Rumble, D., 2007. S-33 constraints on the seawater sulfate  
1347 contribution in modern seafloor hydrothermal vent sulfides. Geochimica et Cosmochimica Acta  
1348 71, 1170-1182.

1349 Pallister, J.S., Hopson, C.A., 1981. Samail Ophiolite Plutonic Suite - Field Relations, Phase Variation,  
1350 Cryptic Variation and Layering, and a Model of a Spreading Ridge Magma Chamber. Journal  
1351 of Geophysical Research 86, 2593-2644.

1352 Patten, C.G., Pitcairn, I.K., Teagle, D.A., Harris, M., 2016. Mobility of Au and related elements during  
1353 the hydrothermal alteration of the oceanic crust: implications for the sources of metals in VMS  
1354 deposits. Mineralium Deposita 51, 179-200.

1355 Paytan, A., Kastner, M., Campbell, D., Thiemens, M.H., 2004. Seawater sulfur isotope fluctuations in  
1356 the Cretaceous. Science 304, 1663-1665.

1357 Peters, M., Strauss, H., Farquhar, J., Ockert, C., Eickmann, B., Jost, C.L., 2010. Sulfur cycling at the  
1358 Mid-Atlantic Ridge: A multiple sulfur isotope approach. Chemical Geology 269, 180-196.

1359 Peters, M., Strauss, H., Petersen, S., Kummer, N.-A., Thomazo, C., 2011. Hydrothermalism in the  
1360 Tyrrhenian Sea: Inorganic and microbial sulfur cycling as revealed by geochemical and  
1361 multiple sulfur isotope data. *Chemical Geology* 280, 217-231.

1362 Plank, T., Manning, C.E., 2019. Subducting carbon. *Nature* 574, 343-352.

1363 Puchelt, H., Prichard, H., Berner, Z., Maynard, J., 1996. Sulfide mineralogy, sulfur content, and sulfur  
1364 isotope composition of mafic and ultramafic rocks from Leg 147, PROCEEDINGS-OCEAN  
1365 DRILLING PROGRAM SCIENTIFIC RESULTS. NATIONAL SCIENCE FOUNDATION, pp. 91-  
1366 102.

1367 Rice, C.A., Tuttle, M.L., Reynolds, R.L., 1993. The analysis of forms of sulfur in ancient sediments and  
1368 sedimentary rocks: comments and cautions. *Chemical Geology* 107, 83-95.

1369 Richardson, C.J., Cann, J.R., Richards, H.G., Cowan, J.G., 1987. Metal-depleted root zones of the  
1370 Troodos ore-forming hydrothermal systems, Cyprus. *Earth and Planetary Science Letters* 84,  
1371 243-253.

1372 Richter, L., Diamond, L.W., 2022. Characterization of hydrothermal fluids that alter the upper oceanic  
1373 crust to spilite and epidote: Fluid inclusion evidence from the Semail (Oman) and Troodos  
1374 (Cyprus) ophiolites. *Geochimica et Cosmochimica Acta* 319, 220-253.

1375 Rioux, M., Garber, J.M., Searle, M., Kelemen, P., Miyashita, S., Adachi, Y., Bowring, S., 2021. High-  
1376 precision U-Pb zircon dating of late magmatism in the Samail ophiolite: A record of subduction  
1377 initiation. *Journal of Geophysical Research: Solid Earth* 126, e2020JB020758.

1378 Sakai, H., Des Marais, D., Ueda, A., Moore, J., 1984. Concentrations and isotope ratios of carbon,  
1379 nitrogen and sulfur in ocean-floor basalts. *Geochimica et Cosmochimica Acta* 48, 2433-2441.

1380 Salters, V.J., Stracke, A., 2004. Composition of the depleted mantle. *Geochemistry, Geophysics,  
1381 Geosystems* 5.

1382 Schwarzenbach, E.M., Gill, B.C., Johnston, D.T., 2018. Unraveling multiple phases of sulfur cycling  
1383 during the alteration of ancient ultramafic oceanic lithosphere. *Geochimica et Cosmochimica  
1384 Acta* 223, 279-299.

1385 Seyfried Jr, W., Bischoff, J.L., 1981. Experimental seawater-basalt interaction at 300 C, 500 bars,  
1386 chemical exchange, secondary mineral formation and implications for the transport of heavy  
1387 metals. *Geochimica et Cosmochimica Acta* 45, 135-147.

1388 Seyfried, W.E., Jr., Ding, K., Berndt, M.E., Chen, X., 1997. Experimental and Theoretical Controls on  
1389 the Composition of Mid-Ocean Ridge Hydrothermal Fluids, Volcanic Associated Massive  
1390 Sulfide Deposits: Processes and Examples in Modern and Ancient Settings. *Society of  
1391 Economic Geologists*, p. 0.

1392 Shanks, W.C., 2001. Stable isotopes in seafloor hydrothermal systems: vent fluids, hydrothermal  
1393 deposits, hydrothermal alteration, and microbial processes. *Reviews in Mineralogy and*  
1394 *Geochemistry* 43, 469-525.

1395 Shanks, W.C., Bischoff, J.L., Rosenbauer, R.J., 1981. Seawater sulfate reduction and sulfur isotope  
1396 fractionation in basaltic systems: Interaction of seawater with fayalite and magnetite at 200–  
1397 350°C. *Geochimica et Cosmochimica Acta* 45, 1977-1995.

1398 Sleep, N.H., 1991. Hydrothermal circulation, anhydrite precipitation, and thermal structure at ridge axes.  
1399 *Journal of Geophysical Research: Solid Earth* 96, 2375-2387.

1400 Staudigel, H., 2014. Chemical fluxes from hydrothermal alteration of the oceanic crust.

1401 Taylor, B.E., Wheeler, M.C., Nordstrom, D.K., 1984. Stable isotope geochemistry of acid mine drainage:  
1402 Experimental oxidation of pyrite. *Geochimica et Cosmochimica Acta* 48, 2669-2678.

1403 Teagle, D., Cooper, M., Harris, M., Crispini, L., Kelemen, P., 2019. Tethyan anhydrite preserved in the  
1404 lower crust of the Samail ophiolite: Evidence from Oman Drilling Project Holes GT1A and 2A,  
1405 *Geophysical Research Abstracts*.

1406 Teagle, D.A., Alt, J.C., Halliday, A.N., 1998. Tracing the chemical evolution of fluids during hydrothermal  
1407 recharge: Constraints from anhydrite recovered in ODP Hole 504B. *Earth and Planetary*  
1408 *Science Letters* 155, 167-182.

1409 Teagle, D.A., Ildefonse, B., Blum, P., 2010. Integrated Ocean Drilling Program Expedition 335 Scientific  
1410 Prospectus Superfast Spreading Rate Crust 4.

1411 Timofeeff, M.N., Lowenstein, T.K., Da Silva, M.A.M., Harris, N.B., 2006. Secular variation in the major-  
1412 ion chemistry of seawater: Evidence from fluid inclusions in Cretaceous halites. *Geochimica*  
1413 *et Cosmochimica Acta* 70, 1977-1994.

1414 White, W., Klein, E., 2014. 4.13-Composition of the oceanic crust. *Treatise on Geochemistry* (second  
1415 edition), 457-496.

1416 Whitehouse, M.J., 2013. Multiple sulfur isotope determination by SIMS: Evaluation of reference sulfides  
1417 for  $\Delta 33S$  with observations and a case study on the determination of  $\Delta 36S$ . *Geostandards and*  
1418 *Geoanalytical Research* 37, 19-33.

1419 Whitehouse, M.J., Kamber, B.S., Fedo, C.M., Lepland, A., 2005. Integrated Pb- and S-isotope  
1420 investigation of sulphide minerals from the early Archaean of southwest Greenland. *Chemical*  
1421 *Geology* 222, 112-131.

1422 Wilson, D.S., Teagle, D.A., Alt, J.C., Banerjee, N.R., Umino, S., Miyashita, S., Acton, G.D., Anma, R.,  
1423 Barr, S.R., Belghoul, A., 2006. Drilling to gabbro in intact ocean crust. *Science* 312, 1016-  
1424 1020.

1425 Woodruff, L.G., Shanks III, W.C., 1988. Sulfur isotope study of chimney minerals and vent fluids from  
1426 21 N, East Pacific Rise: hydrothermal sulfur sources and disequilibrium sulfate reduction.  
1427 Journal of Geophysical Research: Solid Earth 93, 4562-4572.

1428 Zhang, C., Koepke, J., Wolff, P.E., Horn, I., Garbe-Schönberg, D., Berndt, J., 2021. Multi-Stage  
1429 Hydrothermal Veins in Layered Gabbro of the Oman Ophiolite: Implications for Focused Fluid  
1430 Circulation in the Lower Oceanic Crust. Journal of Geophysical Research: Solid Earth 126,  
1431 e2021JB022349.

1432 Zihlmann, B., Müller, S., Coggon, R.M., Koepke, J., Garbe-Schönberg, D., Teagle, D.A., 2018.  
1433 Hydrothermal fault zones in the lower oceanic crust: An example from Wadi Gideah, Samail  
1434 ophiolite, Oman. Lithos 323, 103-124.

1435

| Ref                       | Lithology                           | AVS     |                       |       | CRS     |                       |       | Sulfates |                       |       | Sulfide-S (ppm) | TS Ext (ppm) | SO <sub>4</sub> /TS | δ <sup>34</sup> S Bulk Sulfide |
|---------------------------|-------------------------------------|---------|-----------------------|-------|---------|-----------------------|-------|----------|-----------------------|-------|-----------------|--------------|---------------------|--------------------------------|
|                           |                                     | S (ppm) | δ <sup>34</sup> S (‰) | ± (‰) | S (ppm) | δ <sup>34</sup> S (‰) | ± □   | S (ppm)  | δ <sup>34</sup> S (‰) | ± (‰) |                 |              |                     |                                |
| GT3A-9Z1 7.0-12.0         | Diabase                             |         |                       |       | 6       | -0.5                  |       |          |                       |       | 6               | 6            |                     | -0.5                           |
| GT3A-22Z2 4.0-9.0 DIA     | Diabase                             |         |                       |       | 2       | 0.5                   |       | 3        |                       |       | 2               | 4            | 0.64                | 0.5                            |
| GT3A-26Z3 10.0-15.0       | Diabase                             |         |                       |       | 60      | 5.1                   | 0.001 | 29       |                       |       | 60              | 89           | 0.32                | 5.1                            |
| GT3A-41Z3 22.0-27.0       | Basalt                              |         |                       |       | 212     | -12.8                 | 0.003 |          |                       |       | 212             | 212          |                     | -12.8                          |
| GT3A-48Z1 11.0-13.0       | Basalt                              |         |                       |       | 862     | 13.2                  | 0.018 |          |                       |       | 862             | 862          |                     | 13.2                           |
| GT3A-52Z1 35.0-40.0       | Basalt                              |         |                       |       | 1060    | 11.3                  | 0.001 | 25       |                       |       | 1060            | 1084         | 0.02                | 11.3                           |
| GT3A-56Z1 59.0-64.0       | Ol Gabbro                           |         |                       |       | 650     | 13.3                  | 0.002 | 15       |                       |       | 650             | 665          | 0.02                | 13.3                           |
| GT3A-63Z1 0.0-6.0         | Plag-cpx phryic Basalt              |         |                       |       | 462     | 13.6                  | 0.017 |          |                       |       | 462             | 462          |                     | 13.6                           |
| GT3A-65Z1 36.0-39.0       | Basalt                              |         |                       |       | 97      | 8.8                   | 0.021 | 8        |                       |       | 97              | 105          | 0.07                | 8.8                            |
| GT3A-73Z4 9.0-14.0 GB     | Oxide Gabbro                        |         |                       |       | 4       | 3.2                   | 0.035 | 3        |                       |       | 4               | 7            | 0.44                | 3.2                            |
| GT3A-78Z1 36.0-41.0       | Basalt                              |         |                       |       | 94      | 7.1                   | 0.009 | 3        |                       |       | 94              | 98           | 0.03                | 7.1                            |
| GT3A-91Z4 80.0-85.0       | Basalt (Dior Xen)                   |         |                       |       | 105     | 9.4                   | 0.056 | 20       |                       |       | 105             | 125          | 0.16                | 9.4                            |
| GT3A-94Z1 27.0-32.0 BAS   | (Basalt / Diorite) Basalt fraction  |         |                       |       | 4032    | 10.4                  | 0.041 |          |                       |       | 4032            | 4032         |                     | 10.4                           |
| GT3A-94Z1 27.0-32.0 DIOR  | (Basalt / Diorite) Diorite fraction |         |                       |       | 36      | 3.8                   | 0.009 |          |                       |       | 36              | 36           |                     | 3.8                            |
| GT3A-100Z4 67.0-72.0      | Oxide Gabbro                        |         |                       |       | 21      | 5.4                   | 0.052 | 2        |                       |       | 21              | 23           | 0.09                | 5.4                            |
| GT3A-101Z3 66.0-71.0      | Basalt                              |         |                       |       | 1545    | 11.7                  | 0.008 |          |                       |       | 1545            | 1545         |                     | 11.7                           |
| GT3A-109Z1 27.0-35.0      | Gabbro                              |         |                       |       | 37      | 8.4                   | 0.012 | 14       |                       |       | 37              | 51           | 0.27                | 8.4                            |
| GT3A-121Z4 7.0-15.0       | Oxide Dissiminated Gabbro           |         |                       |       | 43      | 8.6                   | 0.027 |          |                       |       | 43              | 43           |                     | 8.6                            |
| GT3A-128Z2 62.0-70.0      | Oxide Gabbro                        |         |                       |       | 714     | 5.1                   | 0.008 |          |                       |       | 714             | 714          |                     | 5.1                            |
| GT3A-130Z1 55.0-63.0 GB   | Oxide Gabbro                        |         |                       |       | 837     | 10.2                  | 0.020 |          |                       |       | 837             | 837          |                     | 10.2                           |
| GT3A-132Z2 54.0-62.0      | Gabbro                              |         |                       |       | 8       | 3.6                   | 0.023 | 1        |                       |       | 8               | 10           | 0.14                | 3.6                            |
| GT3A-137Z4 26.0-34.0      | Oxide Gabbro                        |         |                       |       | 103     | 5.9                   | 0.007 |          |                       |       | 103             | 103          |                     | 5.9                            |
| GT3A-139Z1 5.0-13.0       | Oxide Gabbro                        |         |                       |       | 1452    | 5.2                   | 0.010 | 19       |                       |       | 1452            | 1472         | 0.01                | 5.2                            |
| GT3A-140Z2 22.0-30.0      | Plag-cpx phryic Basalt              |         |                       |       | 238     | 5.0                   | 0.059 | 3        |                       |       | 238             | 241          | 0.01                | 5.0                            |
| GT3A-141Z4 43-51          | Pyrite Epidote patch                |         |                       |       | 24902   | 8.6                   | 0.013 |          |                       |       | 24902           | 24902        |                     | 8.6                            |
| GT3A-142Z4 61.0-69.0 DIOR | Diorite                             |         |                       |       | 1575    | 7.1                   | 0.023 | 35       |                       |       | 1575            | 1610         | 0.02                | 7.1                            |
| GT3A-143Z4 24.0-32.0      | Oxide Gabbro                        |         |                       |       | 64      | 4.0                   | 0.037 |          |                       |       | 64              | 64           |                     | 4.0                            |
| GT3A-146Z1 57.0-65.0      | Oxide Gabbro                        |         |                       |       | 11334   | 6.1                   | 0.138 | 76       | 4.9                   |       | 11334           | 11410        | 0.01                | 6.1                            |
| GT3A-146Z4 17.0-21.0      | Oxide Gabbro                        |         |                       |       | 144     | 6.3                   | 0.031 | 37       |                       |       | 144             | 180          | 0.20                | 6.3                            |
| GT3A-155Z3 21.0-29.0      | Oxide Gabbro                        |         |                       |       | 428     | 0.8                   | 0.033 | 12       |                       |       | 428             | 440          | 0.03                | 0.8                            |
| GT2A-24Z2 31.0-36.0       | Ol gabbro                           |         |                       |       | 149     | 1.4                   | 0.039 | 5        |                       |       | 149             | 153          | 0.03                | 1.4                            |
| GT2A-31Z1 70.0-75.1       | Ol gabbro                           |         |                       |       | 151     | 1.5                   | 0.077 | 0.4      |                       |       | 151             | 152          | 0.00                | 1.5                            |
| GT2A-36Z1 50.5-55.5       | Ol gabbro                           |         |                       |       | 483     | 1.1                   | 0.014 | 20       |                       |       | 483             | 503          | 0.04                | 1.1                            |
| GT2A-45Z1 35.0-40.0       | Ol gabbro                           |         |                       |       | 522     | 1.0                   | 0.081 | 11       |                       |       | 522             | 533          | 0.02                | 1.0                            |
| GT2A-55Z2 65.0-70.0       | Ol gabbro                           |         |                       |       | 135     | 1.2                   | 0.063 | 4        |                       |       | 135             | 139          | 0.03                | 1.2                            |
| GT2A-58Z1 15.0-20.0       | Ol bearing Gabbro                   |         |                       |       | 119     | 1.9                   | 0.025 | 18       |                       |       | 119             | 137          | 0.13                | 1.9                            |
| GT2A-67Z3 58.0-68.0       | Ol gabbro                           |         |                       |       | 2951    | 1.8                   | 0.018 | 11       |                       |       | 2951            | 2962         | 0.00                | 1.8                            |
| GT2A-76Z3 61.0-68.0       | Troctolite                          | 0.1     |                       |       | 65      | 2.1                   | 0.107 | 5        |                       |       | 65              | 70           | 0.07                | 2.1                            |
| GT2A-78Z1 73.0-81.0       | Ol gabbro                           |         |                       |       | 2       |                       |       | 111      |                       |       | 2               | 113          | 0.99                |                                |

|                      |                         |     |      |      |       |      |       |      |      |      |      |      |     |
|----------------------|-------------------------|-----|------|------|-------|------|-------|------|------|------|------|------|-----|
| GT2A-83Z1 74.5-82.0  | Ol-bearing Gabbro       | 230 | 228  | 1.0  | 0.025 | 7    | 458   | 465  | 0.01 | 0.5  |      |      |     |
| GT2A-92Z4 11.0-20.0  | Ol gabbro               |     | 450  | 1.0  | 0.037 | 77   | 450   | 527  | 0.15 | 1.0  |      |      |     |
| GT2A-100Z4 14.0-21.0 | Ol gabbro               |     | 1233 | 1.3  | 0.020 | 42   | 1233  | 1275 | 0.03 | 1.3  |      |      |     |
| GT2A-100Z4 44.0-50.0 | Ol gabbro               |     | 54   | -0.7 |       | 197  | 17.3  | 0.01 | 54   | 251  | 0.78 | -0.7 |     |
| GT2A-104Z4 31.0-39.0 | Ol gabbro               |     | 288  | 0.8  | 0.034 | 2    | 288   | 291  | 0.01 | 0.8  |      |      |     |
| GT2A-108Z1 34.0-44.0 | Ol-bearing Gabbronorite |     | 614  | 2.1  | 0.014 | 0.2  | 614   | 614  | 0.00 | 2.1  |      |      |     |
| GT2A-115Z1 40.0-50.0 | Ol gabbro               |     | 563  | 1.4  | 0.032 |      | 563   | 563  |      | 1.4  |      |      |     |
| GT2A-123Z3 54.0-60.0 | Ol gabbro               |     | 705  | 1.2  | 0.007 | 36   | 705   | 741  | 0.05 | 1.2  |      |      |     |
| GT2A-133Z3 26.0-33.0 | Ol gabbro               |     | 729  | 0.6  | 0.079 | 27   | 5.7   | 729  | 756  | 0.04 | 0.6  |      |     |
| GT2A-139Z4 82.0-89.0 | Ol gabbro               |     | 1566 | 0.7  | 0.000 |      | 1566  | 1566 |      | 0.7  |      |      |     |
| GT2A-149Z2 17.0-25.0 | Ol gabbro               |     | 57   |      |       | 24   | 57    | 82   | 0.30 |      |      |      |     |
| GT1A-25Z3 5.0-10.0   | Ol Gabbro               | 28  | 1.9  | 0.04 | 283   | 1.0  | 0.096 | 24   | 2.8  | 310  | 334  | 0.07 | 1.1 |
| GT1A-30Z1 55.0-60.0  | Ol Gabbro               | 3   | 1.8  |      | 48    | 1.8  |       | 5    |      | 52   | 57   | 0.09 | 1.8 |
| GT1A-31Z2 20.0-25.0  | Ol bearing Gabbro       | 337 | 0.3  | 0.04 | 712   | 0.9  | 0.005 | 109  | 3.3  | 1050 | 1159 | 0.09 | 0.7 |
| GT1A-33Z3 45.0-50.0  | Ol Gabbro               |     | 499  | 1.6  | 0.006 |      | 499   | 499  |      | 499  | 499  |      | 1.6 |
| GT1A-39Z1 3.0-12.0   | Ol Melagabbro           | 25  | 1.4  |      | 172   | 1.2  | 0.012 | 13   |      | 197  | 211  | 0.06 | 1.2 |
| GT1A-49Z4 69.5-75.5  | Ol Gabbro               | 26  | -0.2 | 0.08 | 298   | 0.8  | 0.130 |      |      | 324  | 324  |      | 0.7 |
| GT1A-57Z2 42.0-51.0  | Ol Gabbro               |     | 1    |      |       | 4    |       | 1    | 5    | 0.75 |      |      |     |
| GT1A-63Z2 59.0-65.5  | Ol Gabbro               |     | 26   | 1.0  | 0.008 | 689  |       | 26   | 714  | 0.96 | 1.0  |      |     |
| GT1A-72Z4 33.0-45.0  | Ol Gabbro               |     | 17   |      |       |      |       | 17   | 17   |      |      |      |     |
| GT1A-79Z1 50.5-59.5  | Ol Gabbro               |     | 11   | 1.6  |       |      |       | 11   | 11   |      | 1.6  |      |     |
| GT1A-89Z1 18.0-26.0  | Opx-bearing ol gabbro   |     | 83   | -3.2 | 0.014 | 1933 | 17.1  | 0.02 | 83   | 2016 | 0.96 | -3.2 |     |
| GT1A-96Z1 15.0-23.0  | Ol Gabbro               |     | 757  | 2.2  | 0.149 | 19   |       | 757  | 776  | 0.02 | 2.2  |      |     |
| GT1A-100Z1 45.0-50.0 | Ol Gabbro               |     | 303  | -0.1 | 0.043 | 7    |       | 303  | 309  | 0.02 | -0.1 |      |     |
| GT1A-107Z2 55.0-62.0 | Ol Gabbro               |     | 59   | 2.6  | 0.009 | 99   |       | 59   | 157  | 0.63 | 2.6  |      |     |
| GT1A-112Z2 69.0-77.0 | Ol Gabbro               |     | 32   | 1.2  | 0.017 | 1    |       | 32   | 33   | 0.03 | 1.2  |      |     |
| GT1A-119Z4 12.0-20.0 | Ol Gabbro               | 146 | 0.3  | 0.02 | 392   | 0.6  | 0.099 | 113  |      | 538  | 651  | 0.17 | 0.5 |
| GT1A-123Z2 0.0-8.0   | Ol Gabbro               |     | 24   | 2.3  | 0.010 | 1    |       | 24   | 25   | 0.04 | 2.3  |      |     |
| GT1A-136Z3 29.0-37.0 | Ol Gabbro               |     | 52   | 2.3  | 0.004 | 2    |       | 52   | 53   | 0.03 | 2.3  |      |     |
| GT1A-138Z2 56.0-64.0 | Ol Gabbro               | 136 | -0.4 | 0.01 | 429   | 0.5  | 0.114 | 14   |      | 565  | 579  | 0.02 | 0.3 |
| GT1A-141Z4 0.0-8.0   | Ol bearing Gabbro       |     | 35   | 1.4  | 0.005 | 24   | 16.1  | 0.02 | 35   | 58   | 0.41 | 1.4  |     |
| GT1A-147Z2 49.0-54.0 | Ol bearing Gabbro       |     | 114  | 1.9  | 0.020 |      |       | 114  | 114  |      | 1.9  |      |     |
| GT1A-151Z2 45.0-55.0 | Ol Gabbro               |     | 306  | 0.8  | 0.034 | 5    |       | 306  | 311  | 0.02 | 0.8  |      |     |
| GT1A-152Z3 0.0-8.0   | Ol Gabbro               |     | 310  | 0.6  | 0.017 | 1    |       | 310  | 311  | 0.00 | 0.6  |      |     |

| Ref                       | Lithology               | Δ36S<br>[%] | Δ33S<br>[%] | δ34S<br>[%] |
|---------------------------|-------------------------|-------------|-------------|-------------|
| GT3A-26Z3 10.0-15.0       | Diabase                 | 1.001       | -0.012      | 5.31        |
| GT3A-41Z3 22.0-27.0       | Basalt                  | 1.192       | -0.048      | -11.37      |
| GT3A-48Z1 11.0-13.0       | Basalt                  | 1.069       | 0.018       | 13.76       |
| GT3A-56Z1 59.0-64.0       | Ol Gabbro               | 0.931       | 0.008       | 13.80       |
| GT3A-63Z1 0.0-6.0         | Plag-cpx phryic Basalt  | 0.986       | 0.005       | 14.27       |
| GT3A-100Z4 67.0-72.0      | Oxide Gabbro            | 0.815       | -0.002      | 5.56        |
| GT3A-101Z3 66.0-71.0      | Basalt                  | 0.877       | -0.008      | 10.94       |
| GT3A-128Z2 62.0-70.0      | Oxide Gabbro            | 0.968       | -0.017      | 5.33        |
| GT3A-141Z4 43-51          | Pyrite Epidote patch    | 1.069       | -0.011      | 8.91        |
| GT3A-142Z4 61.0-69.0 DIOR | Diorite                 | 0.802       | -0.028      | 5.52        |
| GT3A-146Z1 57.0-65.0      | Oxide Gabbro            | 0.673       | -0.007      | 7.44        |
| GT2A-24Z2 31.0-36.0       | Ol gabbro               | 1.239       | -0.042      | 1.22        |
| GT2A-31Z1 70.0-75.1       | Ol gabbro               | 1.091       | -0.036      | 1.42        |
| GT2A-67Z3 58.0-68.0       | Ol gabbro               | 1.022       | -0.029      | 1.79        |
| GT2A-83Z1 74.5-82.0       | Ol-bearing Gabbro       | 1.520       | -0.024      | 2.28        |
| GT2A-100Z4 44.0-50.0      | Ol gabbro               | 1.059       | -0.014      | -0.66       |
| GT2A-108Z1 34.0-44.0      | Ol-bearing Gabbronorite | 0.857       | -0.034      | 2.20        |
| GT2A-133Z3 26.0-33.0      | Ol gabbro               | 0.907       | -0.023      | 0.78        |
| GT1A-30Z1 55.0-60.0       | Ol Gabbro               | 1.145       | -0.023      | 1.55        |
| GT1A-31Z2 20.0-25.0       | Ol bearing Gabbro       | 1.145       | -0.033      | 0.59        |
| GT1A-49Z4 69.5-75.5       | Ol Gabbro               | 1.143       | -0.032      | 0.60        |
| GT1A-100Z1 45.0-50.0      | Ol Gabbro               | 1.083       | -0.019      | -0.17       |
| GT1A-123Z2 0.0-8.0        | Ol Gabbro               | 1.119       | -0.035      | 2.42        |
| GT1A-147Z2 49.0-54.0      | Ol bearing Gabbro       | 0.980       | -0.042      | 2.03        |
| GT1A-152Z3 0.0-8.0        | Ol Gabbro               | 1.044       | -0.030      | 0.76        |

| SAMPLE           |             | Mineral Phase          | Sulfide Type | $\delta^{34}\text{S}$ ‰ | ± ‰  |
|------------------|-------------|------------------------|--------------|-------------------------|------|
| GT3A-47Z4 34-39  | Basalt      | Py small bleb 1 (C)    | Hydro        | <b>13.8</b>             | 0.05 |
| GT3A-47Z4 34-39  | Basalt      | Py small bleb 1 (B)    | Hydro        | <b>13.9</b>             | 0.06 |
| GT3A-47Z4 34-39  | Basalt      | Py small bleb 2 (C)    | Hydro        | <b>13.5</b>             | 0.05 |
| GT3A-47Z4 34-39  | Basalt      | Py small bleb 2 (B)    | Hydro        | <b>12.9</b>             | 0.06 |
| GT3A-48Z1 11-13  | Basalt      | Py large bleb (C)      | Hydro        | <b>11.9</b>             | 0.05 |
| GT3A-48Z1 11-13  | Basalt      | Py large bleb (T)      | Hydro        | <b>11.1</b>             | 0.06 |
| GT3A-48Z1 11-13  | Basalt      | Py large bleb (T)      | Hydro        | <b>12.7</b>             | 0.08 |
| GT3A-48Z1 11-13  | Basalt      | Py large bleb (T)      | Hydro        | <b>14.2</b>             | 0.06 |
| GT3A-48Z1 11-13  | Basalt      | Py large bleb (B)      | Hydro        | <b>14.4</b>             | 0.05 |
| GT3A-140Z2 22-30 | Basalt      | Ccp dusty              | Hydro        | <b>2.5</b>              | 0.28 |
| GT3A-140Z2 22-30 | Basalt      | Ccp dusty              | Hydro        | <b>1.8</b>              | 0.29 |
| GT3A-140Z2 22-30 | Basalt      | Py large aggregate (C) | Hydro        | <b>1.0</b>              | 0.08 |
| GT3A-140Z2 22-30 | Basalt      | Py large aggregate (C) | Hydro        | <b>0.9</b>              | 0.08 |
| GT3A-140Z2 22-30 | Basalt      | Py large aggregate (C) | Hydro        | <b>1.2</b>              | 0.09 |
| GT3A-140Z2 22-30 | Basalt      | Py large aggregate (B) | Hydro        | <b>0.9</b>              | 0.09 |
| GT3A-140Z2 22-30 | Basalt      | Py large aggregate (B) | Hydro        | <b>0.7</b>              | 0.08 |
| GT3A-140Z2 22-30 | Basalt      | Py grain 2 (C)         | Hydro        | <b>-1.0</b>             | 0.09 |
| GT3A-140Z2 22-30 | Basalt      | Py grain 1 (B)         | Hydro        | <b>1.0</b>              | 0.08 |
| GT3A-140Z2 22-30 | Basalt      | Py grain 1 (B)         | Hydro        | <b>1.2</b>              | 0.08 |
| GT3A-141Z4 43-51 | Ep Py patch | Py-ep patch ©          | Hydro        | <b>9.6</b>              | 0.07 |
| GT3A-141Z4 43-51 | Ep Py patch | Py-ep patch (traverse) | Hydro        | <b>10.0</b>             | 0.07 |
| GT3A-141Z4 43-51 | Ep Py patch | Py-ep patch (traverse) | Hydro        | <b>9.3</b>              | 0.07 |
| GT3A-141Z4 43-51 | Ep Py patch | Py-ep patch (traverse) | Hydro        | <b>9.5</b>              | 0.07 |
| GT3A-141Z4 43-51 | Ep Py patch | Py-ep patch (traverse) | Hydro        | <b>9.9</b>              | 2.00 |
| GT3A-141Z4 43-51 | Ep Py patch | Py-ep patch (B)        | Hydro        | <b>7.3</b>              | 0.07 |
| GT3A-142Z3 4-10  | Diorite     | Ccp grain 1 (C)        | Hydro        | <b>13.1</b>             | 0.09 |
| GT3A-142Z3 4-10  | Diorite     | Ccp grain 1 (B)        | Hydro        | <b>2.4</b>              | 0.10 |
| GT3A-142Z3 4-10  | Diorite     | Ccp grain 2 (C)        | Hydro        | <b>7.4</b>              | 0.11 |
| GT3A-142Z3 4-10  | Diorite     | Ccp grain 2 (B)        | Hydro        | <b>7.2</b>              | 0.11 |
| GT3A-142Z3 4-10  | Diorite     | Ccp small              | Hydro        | <b>3.1</b>              | 0.15 |
| GT3A-142Z3 4-10  | Diorite     | Ccp small              | Hydro        | <b>6.4</b>              | 0.08 |
| GT3A-142Z3 4-10  | Diorite     | Ccp small              | Hydro        | <b>7.4</b>              | 0.08 |
| GT3A-142Z3 4-10  | Diorite     | Py 1 (C)               | Hydro        | <b>3.1</b>              | 0.08 |
| GT3A-142Z3 4-10  | Diorite     | Py 1 (B)               | Hydro        | <b>5.4</b>              | 0.10 |
| GT3A-142Z3 4-10  | Diorite     | Py 2 (C)               | Hydro        | <b>1.6</b>              | 0.08 |
| GT3A-142Z3 4-10  | Diorite     | Py 2 (B)               | Hydro        | <b>1.3</b>              | 0.09 |
| GT3A-146Z1 57-65 | Oxide Gb    | Py non cataclastic (C) | Hydro        | <b>6.2</b>              | 0.06 |
| GT3A-146Z1 57-66 | Oxide Gb    | Py non cataclastic (B) | Hydro        | <b>5.9</b>              | 0.06 |
| GT3A-146Z1 57-67 | Oxide Gb    | Py Cataclastic ©       | Hydro        | <b>6.0</b>              | 0.06 |
| GT3A-146Z1 57-68 | Oxide Gb    | Py Cataclastic (B)     | Hydro        | <b>6.4</b>              | 0.07 |
| GT2A-31Z1 68-70  | OI Gabbro   | Ccp Vein               | Hydro        | <b>0.7</b>              | 0.11 |
| GT2A-31Z1 68-70  | OI Gabbro   | Ccp Vein               | Hydro        | <b>0.4</b>              | 0.11 |
| GT2A-31Z1 68-70  | OI Gabbro   | Ccp Vein               | Hydro        | <b>1.5</b>              | 0.12 |
| GT2A-36Z1 59-62  | OI Gabbro   | Ccp (C)                | Remob        | <b>1.2</b>              | 0.10 |
| GT2A-36Z1 59-62  | OI Gabbro   | Ccp (B)                | Remob        | <b>1.3</b>              | 0.10 |
| GT2A-36Z1 59-62  | OI Gabbro   | Py after Po (C)        | Metas        | <b>-1.5</b>             | 0.33 |
| GT2A-36Z1 59-62  | OI Gabbro   | Py after Po (B)        | Metas        | <b>-0.8</b>             | 0.27 |
| GT2A-36Z1 59-62  | OI Gabbro   | Ccp in altered OI (C)  | Remob        | <b>0.8</b>              | 0.12 |
| GT2A-36Z1 59-62  | OI Gabbro   | Py bulky (C)           | Hydro        | <b>0.1</b>              | 0.11 |

|                  |                   |                                |       |             |      |
|------------------|-------------------|--------------------------------|-------|-------------|------|
| GT2A-36Z1 59-62  | Ol Gabbro         | Py bulky (B)                   | Hydro | <b>1.6</b>  | 0.13 |
| GT2A-100Z4 14-17 | Ol Gabbro         | Ccp intergranular veinlet (C)  | Hydro | <b>0.6</b>  | 0.19 |
| GT2A-100Z4 14-17 | Ol Gabbro         | Ccp intergranular veinlet (B)  | Hydro | <b>0.4</b>  | 0.16 |
| GT2A-100Z4 14-17 | Ol Gabbro         | Ccp PI fractures               | Hydro | <b>1.0</b>  | 0.16 |
| GT2A-100Z4 14-17 | Ol Gabbro         | Ccp Ol fractures               | Hydro | <b>0.7</b>  | 0.19 |
| GT2A-100Z4 14-17 | Ol Gabbro         | Ccp intergranular veinlet      | Hydro | <b>-1.8</b> | 0.23 |
| GT2A-100Z4 14-17 | Ol Gabbro         | Ccp Ol fractures               | Hydro | <b>1.6</b>  | 0.16 |
| GT2A-100Z4 14-17 | Ol Gabbro         | Py dendritic aggregate (C)     | Hydro | <b>2.7</b>  | 0.11 |
| GT2A-100Z4 14-17 | Ol Gabbro         | Py dendritic aggregate (B)     | Hydro | <b>1.6</b>  | 0.06 |
| GT2A-100Z4 14-17 | Ol Gabbro         | Ccp in hydrous silicates (C)   | Meta  | <b>1.1</b>  | 0.19 |
| GT2A-100Z4 14-17 | Ol Gabbro         | Ccp in hydrous silicates (B)   | Meta  | <b>1.8</b>  | 0.15 |
| GT2A-139Z4 77-80 | Ol Gabbro         | Ccp                            | Remob | <b>0.0</b>  | 0.13 |
| GT2A-139Z4 77-80 | Ol Gabbro         | Po (C)                         | Remob | <b>-1.8</b> | 0.15 |
| GT2A-139Z4 77-80 | Ol Gabbro         | Po (B)                         | Remob | <b>-3.8</b> | 0.19 |
| GT2A-139Z4 77-80 | Ol Gabbro         | Po Smec-Chl aggregate after Ol | Hydro | <b>-3.8</b> | 0.17 |
| GT2A-139Z4 77-80 | Ol Gabbro         | Po Smec-Chl aggregate after Ol | Hydro | <b>-3.8</b> | 0.12 |
| GT2A-139Z4 77-80 | Ol Gabbro         | Po Smec-Chl aggregate after Ol | Hydro | <b>-5.0</b> | 0.24 |
| GT2A-139Z4 77-80 | Ol Gabbro         | Py dendritic aggregate (C)     | Hydro | <b>-1.0</b> | 0.12 |
| GT2A-139Z4 77-80 | Ol Gabbro         | Py dendritic aggregate (C)     | Hydro | <b>-1.2</b> | 0.11 |
| GT1A-30Z1 55-60  | Ol Gabbro         | Ccp in Polydimite aggregate    | Meta  | <b>1.4</b>  | 0.07 |
| GT1A-30Z1 55-60  | Ol Gabbro         | Ccp                            | Remob | <b>0.5</b>  | 0.10 |
| GT1A-30Z1 55-60  | Ol Gabbro         | Ccp                            | Remob | <b>0.6</b>  | 0.09 |
| GT1A-30Z1 55-60  | Ol Gabbro         | Ccp in altered Ol              | Hydro | <b>2.0</b>  | 0.09 |
| GT1A-30Z1 55-60  | Ol Gabbro         | Ccp in altered Ol              | Hydro | <b>1.0</b>  | 0.13 |
| GT1A-31Z2 20-25  | Ol bearing Gabbro | Ccp in Po                      | Mag   | <b>0.9</b>  | 0.06 |
| GT1A-31Z2 20-25  | Ol bearing Gabbro | Ccp in Po                      | Mag   | <b>0.9</b>  | 0.06 |
| GT1A-31Z2 20-25  | Ol bearing Gabbro | Ccp in Po                      | Mag   | <b>0.9</b>  | 0.07 |
| GT1A-31Z2 20-25  | Ol bearing Gabbro | Ccp in Po                      | Mag   | <b>1.0</b>  | 0.08 |
| GT1A-31Z2 20-25  | Ol bearing Gabbro | Ccp in Po                      | Mag   | <b>0.8</b>  | 0.07 |
| GT1A-31Z2 20-25  | Ol bearing Gabbro | Po                             | Mag   | <b>0.0</b>  | 0.10 |
| GT1A-31Z2 20-25  | Ol bearing Gabbro | Po                             | Mag   | <b>0.1</b>  | 0.10 |
| GT1A-31Z2 20-25  | Ol bearing Gabbro | Po                             | Mag   | <b>0.0</b>  | 0.09 |
| GT1A-31Z2 20-25  | Ol bearing Gabbro | Po                             | Mag   | <b>-1.0</b> | 0.79 |
| GT1A-31Z2 20-25  | Ol bearing Gabbro | Po Smec-Chl aggregate after Ol | Hydro | <b>0.5</b>  | 0.10 |
| GT1A-31Z2 20-25  | Ol bearing Gabbro | Po Smec-Chl aggregate after Ol | Hydro | <b>0.8</b>  | 0.10 |
| GT1A-72Z4 33-45  | Ol Gabbro         | Ccp platelets in Cpx           | Hydro | <b>0.5</b>  | 0.10 |
| GT1A-72Z4 33-45  | Ol Gabbro         | Ccp platelets in Cpx           | Hydro | <b>2.5</b>  | 0.07 |
| GT1A-72Z4 33-45  | Ol Gabbro         | Ccp platelets in Cpx           | Hydro | <b>-1.2</b> | 0.13 |
| GT1A-72Z4 33-45  | Ol Gabbro         | Ccp platelets in Cpx           | Hydro | <b>-0.4</b> | 0.22 |
| GT1A-100Z1 45-50 | Ol Gabbro         | Ccp                            | Remob | <b>-0.3</b> | 0.13 |
| GT1A-100Z1 45-50 | Ol Gabbro         | Ccp                            | Remob | <b>-0.4</b> | 0.12 |
| GT1A-100Z1 45-50 | Ol Gabbro         | Py after Po                    | Meta  | <b>-3.2</b> | 0.29 |
| GT1A-100Z1 45-50 | Ol Gabbro         | Py in Ccp aggregate            | Metas | <b>0.4</b>  | 0.07 |
| GT1A-100Z1 45-50 | Ol Gabbro         | Py in Ccp aggregate            | Metas | <b>0.0</b>  | 0.08 |
| GT1A-100Z1 45-50 | Ol Gabbro         | Ccp in Py aggregate            | Remob | <b>0.1</b>  | 0.11 |
| GT1A-112Z2 69-77 | Ol Gabbro         | Co-pyrite (C)                  | Hydro | <b>2.2</b>  | 0.08 |

|                  |           |                     |       |             |      |
|------------------|-----------|---------------------|-------|-------------|------|
| GT1A-112Z2 69-77 | Ol Gabbro | Co-pyrite (B)       | Hydro | <b>2.6</b>  | 0.08 |
| GT1A-112Z2 69-77 | Ol Gabbro | Co-pyrite (B)       | Hydro | <b>1.5</b>  | 0.08 |
| GT1A-152Z3 0-8   | Ol Gabbro | Ccp in Po anomalous | Mag   | <b>-0.8</b> | 0.12 |
| GT1A-152Z3 0-8   | Ol Gabbro | Po bleb             | Mag   | <b>-2.2</b> | 0.10 |
| GT1A-152Z3 0-8   | Ol Gabbro | Po bleb             | Mag   | <b>-4.3</b> | 0.14 |

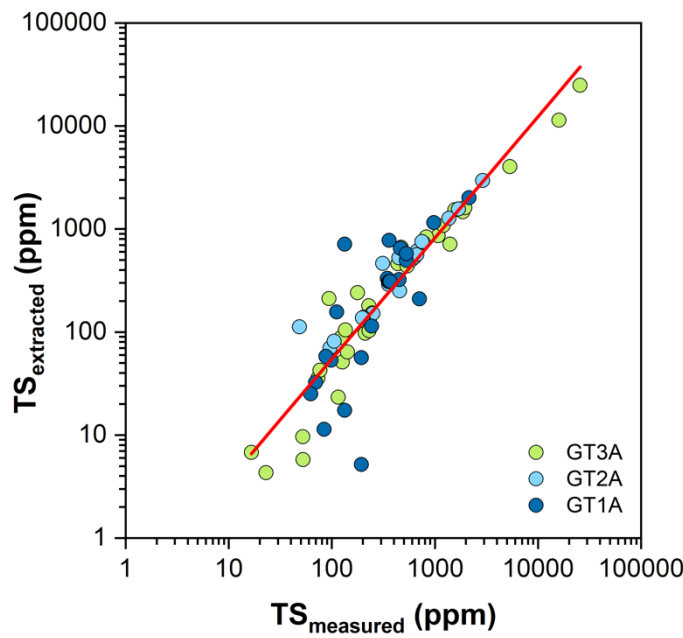
**Table 1.** Modal estimates for studied samples including: 1) total alteration % by weighted average of each magmatic mineral species; 2) relative modes for remobilized, magmatic and hydrothermal sulfide; and 3) relative modes for sulfide species as reported in section 4.1.

**Table 2.** EPMA data for sulfide assemblages: a) Ni phases; b) Cu-phases; c) Fe-phases. Classifications for sulfides are as described in text: Magmatic-Mag, Remobilized-Rem, Hydrothermal s.l.-Hydro, Metasomatic. Met. Each mineral phase there are two calculations: Atoms % and the structural formula based on the number of ions in one unit cell. The description column provides a brief description of the mineral association where relevant, the associated sulfides usually are referenced in parenthesis.

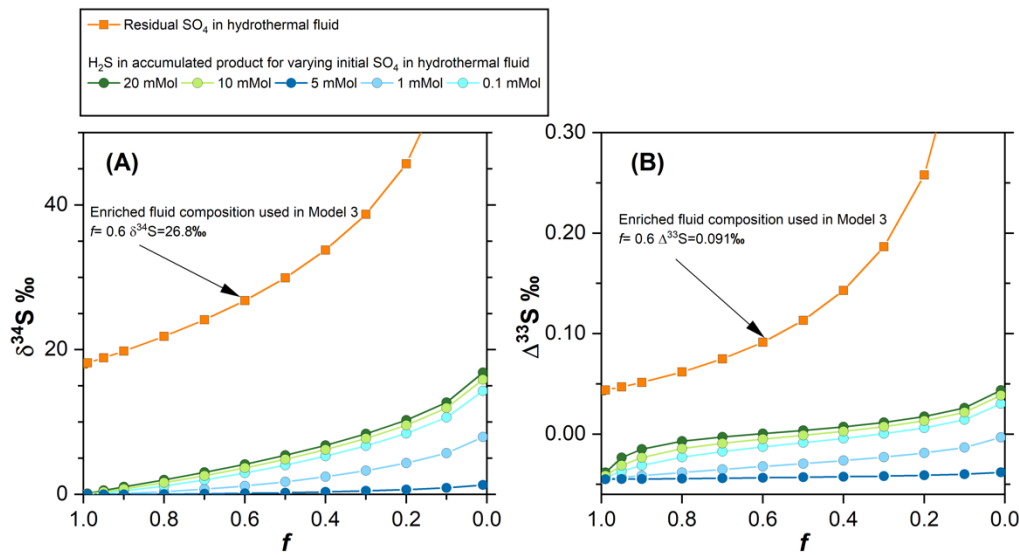
**Mineral Abbreviations:** *Po*-Pyrrhotite, *Pen*-Pentlandite, *Ccp*- Chalcopyrite, *Py*- Pyrite, *Thio*-Thiospinels (*Poly*- Polydimitite, *Sieg*- Siegenite), *Mil*-Milerite, *Bn*- Bornite, *Sph*-Sphalerite,

Other Abbreviations: *Alt*- Altered, *V*-Veins

**Classification-** refers to the paragenetic mode of occurrence of the sulfides: *Mag*- Magmatic, *Remob*- Remobilized, *Met*-Metasomatic, *Hydro*- Hydrothermal.



**SM2 Fig 1.** Relationship between  $TS_{measured}$  in the Eltra furnace and  $TS_{extracted}$  obtained by gravimetry. The  $TS_{measured}$  data were used to determine the amount of sample to process for sulfur sequential extractions and to assess if the extractions were complete.

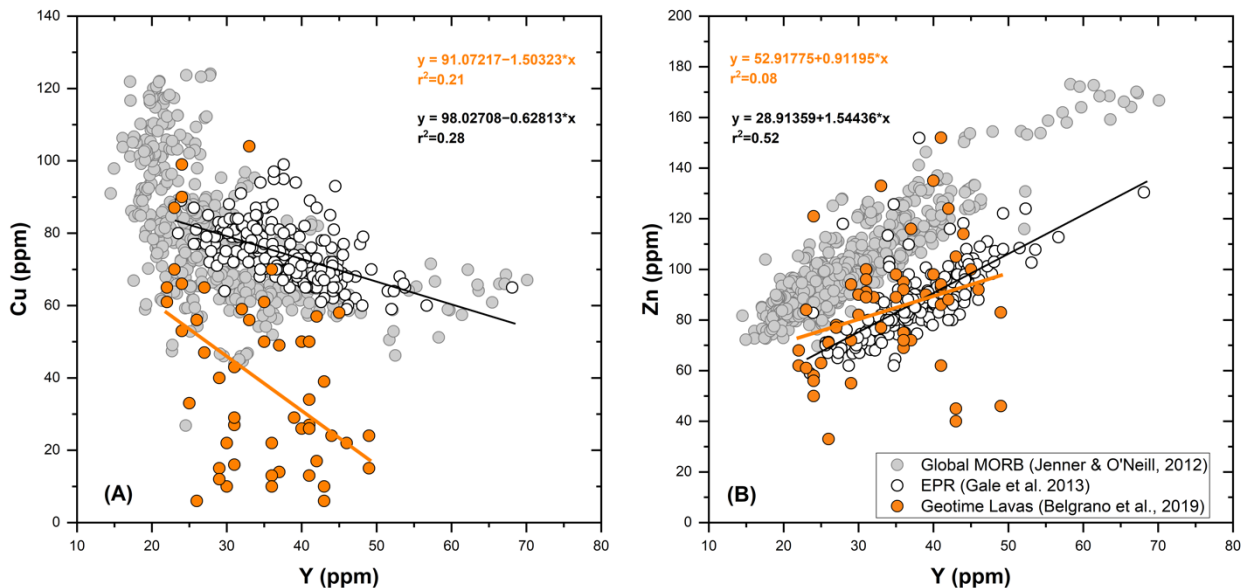


**SM2 Fig 2.** Evolving  $\delta^{34}\text{S}$  (A) and  $\Delta^{33}\text{S}$  (B) isotope composition of the residual  $\text{SO}_4$  in the fluid and pooled (or accumulated)  $\text{H}_2\text{S}$  product as a function of  $f$  during TSR followed by mixing in closed system conditions (Rayleigh distillation). The example is from mixing **Model 2 (Figure 12B)** with magmatic sulfur concentrations of 120 ppm and  $T=350^\circ\text{C}$ . The model was computed for variable sulfate concentrations in the hydrothermal fluid (20, 10, 5, 1 and 0.1 mMol) corresponding to the different coloured curves. The isotope composition of the residual sulfate in the fluid does not vary with initial sulfate concentration in the fluid because it depends exclusively of the  $\text{SO}_4\text{-H}_2\text{S}$  fractionation factor and  $f$ , therefore, only one curve is shown for all considered initial concentrations. The final  $\text{H}_2\text{S}$  product in turn, will depend on how

much sulfate is available in the fluid to convert to H<sub>2</sub>S and in the magmatic rocks which are fixed (compare with mixing Model 2 for 1200 ppm magmatic sulfur in the main text). Therefore, for low initial SO<sub>4</sub> concentrations in the fluid, the H<sub>2</sub>S product is dominated by the composition of magmatic sulfide, whereas at higher SO<sub>4</sub> concentrations more seawater-reduced sulfide will mix with magmatic sulfide producing heavier compositions for the final product. Also shown is both diagrams is the point (f=0.6) where the composition of an enriched fluid used in Model 3 was obtained.

**SM3 Table 1.** Relation between [A] GT3A sulfur geochemistry data from this work ( $TS_{extracted}$ ,  $\delta^{34}S_{\text{sulfide}}$ ) and [B] MgO and  $Fe_{2}O_{3\text{Tot}}$ , concentrations measured by the OmanDP shipboard party (Kelemen et al., 2020) indicating the lithological units(\*) that were matched when measurements were not available in the same interval. Columns [C] show the estimated magmatic concentrations for GT3A rocks on the basis of **Equation 3** (Alt & Shanks 2011) for S-#Mg relationships.

| Sample                   | Lithology         | Depth | Lithologic Unit | Matched Lithologic unit* | [A] this work  |                   | [B] shipboard data |                         |      | [C] S estimates, this work |            |
|--------------------------|-------------------|-------|-----------------|--------------------------|----------------|-------------------|--------------------|-------------------------|------|----------------------------|------------|
|                          |                   |       |                 |                          | $\delta^{34}S$ | $TS_{\text{ext}}$ | MgO                | $Fe_{2}O_{3\text{Tot}}$ | #Mg  | Smag                       | $\Delta S$ |
|                          |                   |       |                 |                          | ‰              | ppm               | wt%                | wt%                     |      | ppm                        | %          |
| GT3A-9Z-1 7.0-12.0       | Diabase           | 6.6   | 3               | 3                        | -0.53          | 6                 | 6.4                | 11.96                   | 0.52 | 1318                       | -100       |
| GT3A-22Z2 4.0-9.0 DB     | Diabase           | 23.7  | 12              | 8 + 13                   | 0.53           | 4                 | 6.9                | 9.83                    | 0.58 | 1193                       | -100       |
| GT3A-26Z-3 10.0-15.0     | Diabase           | 35.1  | 13              | 13                       | 5.12           | 89                | 7.9                | 9.52                    | 0.62 | 1106                       | -92        |
| GT3A-41Z-3 22.0-27.0     | Basalt            | 78.0  | 21              | 16 + 28                  | -12.75         | 212               | 8.1                | 8.51                    | 0.65 | 1044                       | -80        |
| GT3A-48Z-1 11.0-13.0     | Basalt            | 97.4  | 64-1            | 63 + 67                  | 13.21          | 862               | 8.6                | 9.64                    | 0.64 | 1077                       | -20        |
| GT3A-52Z-1 35.0-40.0     | Basalt            | 107.2 | 76              | 67 + 73                  | 11.30          | 1084              | 8.3                | 9.42                    | 0.63 | 1085                       | 0          |
| GT3A-56Z-1 59.0-64.0     | OI Gabbro         | 119.2 | 75-2            | 104                      | 13.25          | 665               | 7.8                | 6.26                    | 0.71 | 929                        | -28        |
| GT3A-63Z-1 0.0-6.0       | Pl-cpx phryic Bas | 136.9 | 86              | 86                       | 13.63          | 462               | 8.6                | 5.62                    | 0.75 | 851                        | -46        |
| GT3A-65Z1 36.0-39.0      | Basalt            | 143.4 | 97              | 97                       | 8.79           | 105               | 7.6                | 8.00                    | 0.65 | 1046                       | -90        |
| GT3A-73Z4 9.0-14.0 GB    | Oxide Gabbro      | 169.9 | 118             | 90                       | 3.25           | 7                 | 7.9                | 6.95                    | 0.69 | 966                        | -99        |
| GT3A-78Z-1 36.0-41.0     | Basalt            | 182.6 | 130             | 130                      | 7.12           | 98                | 7.3                | 10.15                   | 0.59 | 1175                       | -92        |
| GT3A-91Z-4 80.0-85.0     | Basalt (Dior Xen) | 224.4 | 157-2           | 152+160                  | 9.37           | 125               | 4.9                | 9.49                    | 0.49 | 1366                       | -91        |
| GT3A-94Z1 27.0-32.0 BS   | Basalt            | 230.5 | 166             | 166                      | 10.38          | 4032              | 2.5                | 9.88                    | 0.34 | 1677                       | 140        |
| GT3A-94Z1 27.0-32.0 DI   | Diorite           | 230.5 | 166             | 185                      | 3.78           | 36                | 3.0                | 6.20                    | 0.49 | 1368                       | -97        |
| GT3A-100Z-4 67.0-72.0    | Oxide Gabbro      | 251.4 | 176             | 176                      | 5.35           | 23                | 4.4                | 11.58                   | 0.43 | 1490                       | -98        |
| GT3A-101Z-3 66.0-71.0    | Basalt            | 253.5 | 176-1           | 177                      | 11.67          | 1545              | 8.5                | 9.85                    | 0.63 | 1092                       | 41         |
| GT3A-109Z1 27.0-35.0     | Gabbro            | 265.7 | 178             | 178                      | 8.37           | 51                | 7.5                | 7.69                    | 0.66 | 1037                       | -95        |
| GT3A-121Z4 7.0-15.0      | Oxd Diss. Gabbro  | 303.8 | 207             | 216                      | 8.57           | 43                | 3.9                | 13.37                   | 0.36 | 1620                       | -97        |
| GT3A-128Z-2 62.0-70.0    | Oxide Gabbro      | 321.1 | 216             | 216                      | 5.12           | 714               | 3.9                | 10.20                   | 0.43 | 1483                       | -52        |
| GT3A-130Z1 55.0-63.0 GB  | Oxide Gabbro      | 326.5 | 216             | 216                      | 10.17          | 837               | 6.0                | 15.10                   | 0.44 | 1466                       | -43        |
| GT3A-132Z2 54.0-62.0     | Gabbro            | 333.2 | 218             | 218                      | 3.56           | 10                | 8.3                | 9.02                    | 0.65 | 1063                       | -99        |
| GT3A-137Z-4 26.0-34.0    | Oxide Gabbro      | 350.0 | 226             | 235                      | 5.89           | 103               | 4.7                | 15.56                   | 0.37 | 1605                       | -94        |
| GT3A-139Z1 5.0-13.0      | Oxide Gabbro      | 353.4 | 226             | 235                      | 5.23           | 1472              | 4.7                | 15.56                   | 0.37 | 1605                       | -8         |
| GT3A-140Z2 22.0-30.0     | Pl-cpx phryic Bas | 357.6 | 229             | 229                      | 4.99           | 241               | 6.3                | 10.30                   | 0.55 | 1251                       | -81        |
| GT3A-141Z4 43-51         | Gabbro Py-patch   | 362.2 | 232             | 235 + 237                | 8.63           | 24902             | 6.2                | 13.70                   | 0.48 | 1396                       | 1684       |
| GT3A-142Z-4 61.0-69.0 DR | Diorite           | 365.4 | 234             | 234                      | 7.09           | 1610              | 2.2                | 9.49                    | 0.32 | 1716                       | -6         |
| GT3A-143Z4 24.0-32.0     | Oxide Gabbro      | 368.2 | 235             | 235                      | 4.04           | 64                | 4.1                | 14.34                   | 0.36 | 1624                       | -96        |
| GT3A-146Z-1 57.0-65.0    | Oxide Gabbro      | 375.3 | 235             | 235                      | 6.14           | 11410             | 5.2                | 16.78                   | 0.38 | 1586                       | 619        |
| GT3A-146Z4 17.0-21.0     | Oxide Gabbro      | 377.4 | 235             | 235                      | 6.33           | 180               | 4.7                | 15.56                   | 0.37 | 1605                       | -89        |
| GT3A-155Z3 21.0-29.0     | Oxide Gabbro      | 397.8 | 237             | 237                      | 0.78           | 440               | 8.1                | 9.48                    | 0.63 | 1099                       | -60        |



**SM3 Fig 1.** Geotimes lavas from Belgrano et al (2019) Y vs Cu (A) and Y vs Zn (B) and respective regression equations used to estimate Cu and Zn magmatic concentrations for GT3A Hole lavas. Also shown are the EPR basalts from Gale et al. (2013) and the global MORB database of Jenner & O'Neill (2012) filtered out of anomalous, plume-influenced segments with high Cu.

Zn behaves incompatibly and increases along with Y in the melt throughout differentiation. EPR lavas experienced an evolution path at slightly lower Zn at given Y content relative to other MORBs. Geotimes unit follows this trend closely, therefore calculations of  $\Delta$ Zn based on Geotimes (black line in Fig 13H) or EPR concentrations (grey line in Fig 13H) are identical.

Cu has a compatible behaviour and EPR basalts lie within the upper limit of global MORB whereas Geotimes lavas display much lower Cu contents, which should reflect at least in part, the overprint of low-temperature spilitic alteration. As such, we present  $\Delta$ Cu calculated based on the Geotimes lavas (main, black data series in Figure 13G) and on the EPR dataset (Fig 13G greyline). It should be noted that: a) the Geotimes-based calculations represent a more conservative estimate of Cu losses, and therefore are used in the final metal estimates of mobilized metals per volume of crust; b) the extent of hydrothermal alteration in Hole GT3A is such, that the extremely low Cu (and S) concentrations for most of the section invariably result in Cu losses  $> 90\%$ , therefore the main differences lie in the lower gabbro where higher Cu concentrations may represent smaller losses, or minor gains.

Jenner, F. E., & O'Neill, H. S. C. (2012). Analysis of 60 elements in 616 ocean floor basaltic glasses. *Geochemistry, Geophysics, Geosystems*, 13(2).